Supraconductivité et ordre de charge dans les bicouches de graphène moirées

Superconductivity and charge order in twisted bilayer graphene

by

Bahman Pahlevanzadeh

Doctoral thesis submitted to

Faculté des Sciences, Université de Sherbrooke
Sherbrooke, Québec, Canada

and

Faculty of Physics, Isfahan University of Technology
Isfahan, Iran

Le 11 février 2022

le jury a accepté la thèse de Monsieur Bahman Pahlevanzadeh dans sa version finale.

Membres du jury

Pr David Sénéchal
Co-directeur de recherche
Université de Sherbrooke

Pr Peyman Sahebsara
Co-directeur de recherche
Isfahan University of Technology

Pr Claude Bourbonnais
Président rapporteur
Université de Sherbrooke

Pr Farhad Fazileh
Membre interne
Isfahan University of Technology

Pr Akbar Jafari
Membre externe
Sharif University of Technology

DEDICATION

This dissertation is dedicated to the memory of my uncle, Ayub Pahlevanzadeh. He taught me to be kind to everyone.

Also, I would like to dedicate this thesis to my parents, my brothers, and my beloved sister for their endless love, support, and encouragement to accomplish the thesis work.

Last but not the least, I dedicate this thesis to my dear nephews, Taha and Roham.

Summary

The recent discovery of a correlated insulating state and superconductivity in twisted bilayer Graphene (TBG) has opened a new platform for studying unconventional superconductivity. superconductivity appears for TBG at an angle $\sim 1.08°$ for a very low carrier density of about 10^{11} cm^{-2}, with a T_c of 1.7 K.

The misalignment of the two layers of graphene at the magic angle creates a periodic lattice called the moiré lattice. The effective model we use to describe this system is based on the moiré lattice and was proposed by Kang and Vafek. This model includes four Wannier orbitals located at the honeycomb lattice sites. In addition to hopping terms between these orbitals, we also add intra-orbital and inter-orbital interactions to the Hamiltonian and use a Hubbard or extended Hubbard model to describe the system. Our calculations are based on quantum cluster methods. To investigate the superconductivity we tile the lattice by the four site clusters immersed among six bath orbitals and use the CDMFT method. In the study of the correlated insulating phase, we use the VCA method and select clusters consisting of 12 Wannier orbitals so that we can define inter-orbital interactions in a cluster.

We obtain a non-zero $p \pm ip$ order parameter for superconductivity in a wide range of carrier densities, which is consistent with the experimental observations. Experimental measurements show that the system has a gap in the vicinity of $n = 0.5$ and $n = 1.5$ and behaves like a Mott insulator. So we expect that the superconductivity to be suppressed or eliminated in these ranges of densities, which is confirmed by our calculations. $d \pm id$ is another nonzero superconductor order parameter that we found. The size of this singlet order parameter is smaller than the $p \pm ip$. By calculating the Patthoff functional for two kinds of superconductors, we conclude that $p \pm ip$ superconductivity has a lower free energy and therefore is the dominant phase between the two. In addition to the superconducting phase, the study of the strongly correlated insulating phases observed in the experiment was another objective of this thesis. Our calculations confirm the existence of these phases at quarter-, half- and three-quarter filling. Further computations show that the insulating phase at quarter-filling is not a charge density wave and that the insulating phase at half-filling is not antiferromagnetic.

Sommaire

La découverte récente d'un état corrélé isolant et de la supraconductivité dans la bi-couche de graphène moirée (TBG) a ouvert un nouveau canal dans l'étude de la supra-conductivité non conventionnelle. Dans ce système, la supraconductivité apparaît à un angle de torsion $\sim 1.08°$ et à très faible densité de porteurs de 10^{11} cm^{-2}, avec une T_c de $1.7\,K$.

Le défaut d'alignement des deux couches de graphène crée un super-réseau appelé *réseau moiré*. Le modèle effectif utilisé pour décrire ce système est basé sur ce réseau moiré et a été proposé par Kang et Vafek. Ce modèle comporte 4 orbitales de Wannier centrées sur les sites d'un réseau en nid d'abeille. En plus des termes de saut entre ces orbitales, nous ajoutons des interactions (intra- et inter-orbitales) et utilisons le mod-èle de Hubbard étendu pour modéliser ce système. Nos calculs reposent sur les méth-odes d'amas quantiques. Pour étudier la supraconductivité, nous utilisons un dallage du réseau par des amas de quatre sites couplés à six sites de bain dans la théorie du champ moyen dynamique sur amas (CDMFT). Pour l'étude des phases isolantes, nous utilisons plutôt la méthode de l'amas variationnel (VCA) sur un amas de douze sites, de sorte que les interactions étendues peuvent être comprises minimalement dans l'amas.

Pour une large gamme de densités, cohérente avec les observations, nous trouvons un état supraconducteur de type $p \pm ip$. Les expériences montrent que le système pos-sède un gap spectral au voisinage de $n = 0.5$ et $n = 1.5$ et se comporte comme un isolant de Mott. On s'attend donc à ce que la supraconductivité soit atténuée ou éliminée près de ces densités, ce qui est confirmé par nos calculs. On trouve aussi un état supraconduc-teur $d \pm id$ comme solution secondaire, avec un paramètre d'ordre plus petit. Un calcul de la fonctionnelle de Potthoff dans ces deux solutions nous permet d'affirmer que l'état $p \pm ip$ a une énergie plus basse et constitue donc la phase dominante. L'étude des phases isolantes était un deuxième objectif de cette thèse. Nos calculs démontrent l'existence de phases isolantes de Mott au quart remplissage et au demi-remplissage. Des calculs additionnels montrent que l'état isolant à quart rempli n'est pas une onde de densité de charge et que l'état isolant au demi-remplissage n'est pas antiferromagnétique.

Acknowledgements

Contents

List of Figures

Chapter 1

The graphene bilayer

1.1 Graphene

Graphene was isolated for the first time by Konstantin Novoselov and André K. Geim in 2004 at the University of Manchester. For this and other contributions to this eld, they were awarded the Nobel prize in physics in 2010. Following this discovery, graphene has received a lot of attention from theoretical and experimental scientists in order to understand the amazing properties of this 2D crystal. This was the first time that a truly 2D material was observed in Nature. This simple 2D crystal has remarkable electrical, chemical and mechanical properties. One of these exiting properties is the relativistic behavior of its electrons. Electrons in graphene are massless charged particles that obey the Dirac equation. Therefore this system is an ideal candidate for testing quantum eld-theoretical models and making a bridge between condensed matter and high-energy physics. Graphene is an isolated layer of graphite, the most available allotrope of carbon that is made up of very tightly bonded carbon atoms. Graphite has a multilayer structure and in each layer, carbon atoms are organised into a hexagonal lattice. The electronic conguration of carbon is $1s^2 2s^2 2p^2$ which shows that it has 4 valence electrons (2s and 2p) in its outer shell. These valence electrons contributed to make chemical bonds with neighboring atoms. The atomic orbitals of each carbon atom form a sp^2 hybridization in which three electrons are distributed into three in-plane σ bonds, which are strongly covalent. These strong σ bonds and the monolayer character of graphene make it a very special material that breaks many records in terms of strength, electricity, heat conduction, etc. In addition to these three electrons which make σ bands, there is one extra electron per atom that remains in the p_z orbital that is perpendicular to graphene plane. These p_z electrons form the weaker π bond between different layers in graphite. The Electronic structure calculations show that the σ bands are far away from the Fermi level and therefore only the electrons in the π bond contribute to the electronic properties of graphene [100]. Because of this, it is sufcient to treat graphene as a collection of atoms with single p_z orbitals per site. In graphene, carbon atoms are located at the vertices of a hexagonal lattice, which is a bipartite lattice and consists of two sublattices

A and B. To have a Bravais lattice we have to put each two atoms in a repeated unit cell with the basis vectors $(\mathbf{a_1}, \mathbf{a_2})$.

$$\mathbf{a}_1 = \frac{a_0}{2}(3, \sqrt{3})$$
$$\mathbf{a}_2 = \frac{a_0}{2}(3, -\sqrt{3}), \tag{1.1}$$

where $a_0 = 1.42$ Å is the carbon-carbon distance in the hexagonal lattice. The corresponding reciprocal-lattice vectors are given by:

$$\mathbf{b_1} = \frac{2\pi}{3a_0}(1, \sqrt{3})$$
$$\mathbf{b_2} = \frac{2\pi}{3a_0}(1, -\sqrt{3}). \tag{1.2}$$

In Fig. 1.1, we see the hexagonal lattice of graphene which tiles two-sites unit cells, and the corresponding first Brillouin zone. The first Brillouin zone, in this case, has a hexagonal shape and its vertices are called Dirac points. There are only two inequivalent Dirac points denoted $\mathbf{K}$ and $\mathbf{K}'$. We will see that near each Dirac point the energy of the system is a linear function of the wave vector.
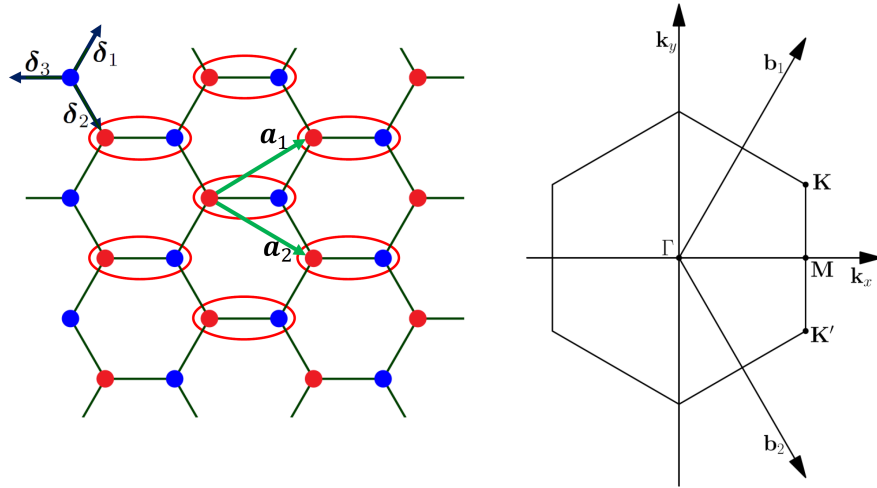
Figure 1.1

Hexagonal structure of graphene and its Brillouin zone. Left panel: honeycomb lattice of single-layer graphene, made out of two triangular sublattices, A (red circles) and B (blue circles); red ellipses indicate the two sites unit cells, $\mathbf{a_{1,2}}$ are the lattice unit vectors and $\boldsymbol{\delta}_i$ are the nearest-neighbor vectors. Right panel: the first Brillouin zone of graphene is a hexagon in momentum space. The reciprocal lattice vectors are $\mathbf{b_{1,2}}$. The Dirac points are denoted by $\mathbf{K}$ and $\mathbf{K}'$.

The simplest tight binding Hamiltonian of this system is:

$$\hat{H} = -t \sum_{\langle ij\rangle\sigma} a^\dagger_{i\sigma} b_{j\sigma} + \text{H.c.}, \tag{1.3}$$

where we only retain the first nearest neighbor hopping terms and t is the hopping amplitude, $a^\dagger_{i\sigma}(b^\dagger_{i\sigma})$ creates an electron on site i of the sublattice $A(B)$. The index σ labels spin projections, the brackets $\langle ...\rangle$ stand for nearest-neighbor sites, and H.c. stands for the Hermitian conjugate term. Since each unit cell has two carbon atoms A and B, the single-electron spectrum of Hamiltonian (1.3) consists of two bands, both of which are doubly degenerate with respect to the spin projection σ. We will follow the standard procedure to find the spectrum. We use the Fourier transform of the electron operators and rewrite the Hamiltonian in k-space,

$$a^\dagger_{i\sigma} = \frac{1}{\sqrt{N}} \sum_{\mathbf{k}} e^{-i\mathbf{k}\cdot\mathbf{r}_i} a^\dagger_{\mathbf{k}\sigma}, \quad b_{j\sigma} = \frac{1}{\sqrt{N}} \sum_{\mathbf{k}} e^{i\mathbf{k}\cdot\mathbf{r}_j} b_{\mathbf{k}\sigma}, \tag{1.4}$$

where N is the number of unit cells in the lattice and the sums run over all the quasi-momenta $\mathbf{k}$ of the Brillouin zone. In this representation the Hamiltonian becomes:

$$\hat{H} = -t \sum_{i\delta_j\sigma} \frac{1}{N} \sum_{\mathbf{k}\mathbf{k}'} e^{-i(\mathbf{k}-\mathbf{k}')\cdot\mathbf{r}_i} e^{i\mathbf{k}'\cdot\delta_j} a^\dagger_{\mathbf{k}\sigma} b_{\mathbf{k}'\sigma} + \text{H.c.}, \tag{1.5}$$

where the index i runs over all the unit cells of the honeycomb lattice and δ_j is the relative position of the nearest neighbor atoms. Using the property $\sum_i e^{-i(\mathbf{k}-\mathbf{k}')\cdot\mathbf{r}_i} = N\delta_{\mathbf{k}\mathbf{k}'}$ the Hamiltonian becomes:

$$\hat{H} = -t \sum_{\mathbf{k}\sigma} a^\dagger_{\mathbf{k}\sigma} b_{\mathbf{k}\sigma} \sum_{\delta_j} e^{i\mathbf{k}\cdot\delta_j} + \text{H.c.}, \tag{1.6}$$

where,

$$\delta_1 = \frac{a_0}{2}(1, \sqrt{3}), \quad \delta_2 = \frac{a_0}{2}(1, -\sqrt{3}), \quad \delta_3 = -a_0(1, 0), \tag{1.7}$$

Thus:

$$\hat{H} = -t \sum_{\mathbf{k}\sigma} f(\mathbf{k}) a^\dagger_{\mathbf{k}\sigma} b_{\mathbf{k}\sigma} + \text{H.c.},$$

$$f(\mathbf{k}) = \sum_{\delta_j} e^{i\mathbf{k}\cdot\delta_j} = \exp(-ia_0 k_x)\left[1 + 2\exp\left(\frac{3ia_0 k_x}{2}\right)\cos\frac{\sqrt{3}a_0 k_y}{2}\right]. \tag{1.8}$$

It is convenient to group the two electron operators into a single spinor $\Psi^\dagger_{\mathbf{k}\sigma} = (a^\dagger_{\mathbf{k}\sigma}, b^\dagger_{\mathbf{k}\sigma})$. In this representation the Hamiltonian becomes:

$$\hat{H} = \sum_{\mathbf{k}\sigma} \Psi^\dagger_{\mathbf{k}\sigma} H_{\mathbf{k}} \Psi_{\mathbf{k}\sigma}, \quad \text{where} \quad H_{\mathbf{k}} = -t \begin{pmatrix} 0 & f(\mathbf{k}) \\ f^*(\mathbf{k}) & 0 \end{pmatrix}. \tag{1.9}$$

3

Where $f^*(\mathbf{k})$ is the complex conjugate of $f(\mathbf{k})$. It is easy to diagonalize this 2×2 matrix and find its eigenvalues and eigenvectors. The energy spectrum is given by:

$$\varepsilon_{\mathbf{k}}^{(1,2)} = \pm t|f(\mathbf{k})|. \tag{1.10}$$

Now we can plot the energy spectrum of this system in $\mathbf{k}$-space. As we can see in Fig. 1.2, the energy spectrum has two energy bands, the upper and lower bands are called the conduction and valence band, respectively. These two bands are connected together at the Dirac points, located at the corners of the first Brillouin zone. It is important to remind ourselves that only two points of these six points are non-equivalent and all the other points are connected to them by a reciprocal lattice vector. These points are conventionally denoted as $\mathbf{K}$ and $\mathbf{K}'$ (see Fig. 1.1). A possible choice of two non-equivalent points is:

$$\mathbf{K} = \frac{2\pi}{3a_0}(1, \frac{1}{\sqrt{3}}), \quad \mathbf{K}' = \frac{2\pi}{3a_0}(1, \frac{-1}{\sqrt{3}}). \tag{1.11}$$

As we can see in Fig. 1.2 the energy spectrum near the Dirac points is a linear function of the quasimomentum $\mathbf{k}$. To find this linear relation it is convenient to dene a 2D vector as $\mathbf{q} = \mathbf{k} - \mathbf{K}$ around a Dirac point (let us say for deniteness the point $\mathbf{K}'$) and to expand the expression for $f(\mathbf{k})$ around $q = 0$.

Using the Taylor expansion we nd:

$$f(\mathbf{k}) = \frac{3a_0}{2}(-ie^{-i\frac{2\pi}{3}})(q_x - iq_y), \tag{1.12}$$

and the Hamiltonian matrix become:

$$H_{\mathbf{k}} = \hbar v_F \begin{pmatrix} 0 & q_x - iq_y \\ q_x + iq_y & 0 \end{pmatrix} \equiv \hbar v_F \hat{\boldsymbol{\sigma}} \cdot \mathbf{q}, \quad v_F = \frac{3a_0 t}{2\hbar} \simeq 10^6 m/s, \tag{1.13}$$

Here I extracted a constant phase factor $(-ie^{-i\frac{2\pi}{3}})$ which clearly has no effect on physical results. By expanding around the second Dirac point ($\mathbf{K}$) the Hamiltonian matrix become:

$$H_{\mathbf{k}} = \hbar v_F \begin{pmatrix} 0 & q_x + iq_y \\ q_x - iq_y & 0 \end{pmatrix}. \tag{1.14}$$

This two matrix representation of the Hamiltonian is similar to the Dirac equation. The standard Dirac equation in four dimensions is:

$$i\hbar \frac{\partial}{\partial t} \begin{pmatrix} \Psi_1 \\ \Psi_2 \\ \Psi_3 \\ \Psi_4 \end{pmatrix} = \begin{pmatrix} mc^2 \mathbb{I} & c\hat{\boldsymbol{\sigma}} \cdot \mathbf{p} \\ c\hat{\boldsymbol{\sigma}} \cdot \mathbf{p} & -mc^2 \mathbb{I} \end{pmatrix} \begin{pmatrix} \Psi_1 \\ \Psi_2 \\ \Psi_3 \\ \Psi_4 \end{pmatrix}, \tag{1.15}$$

4
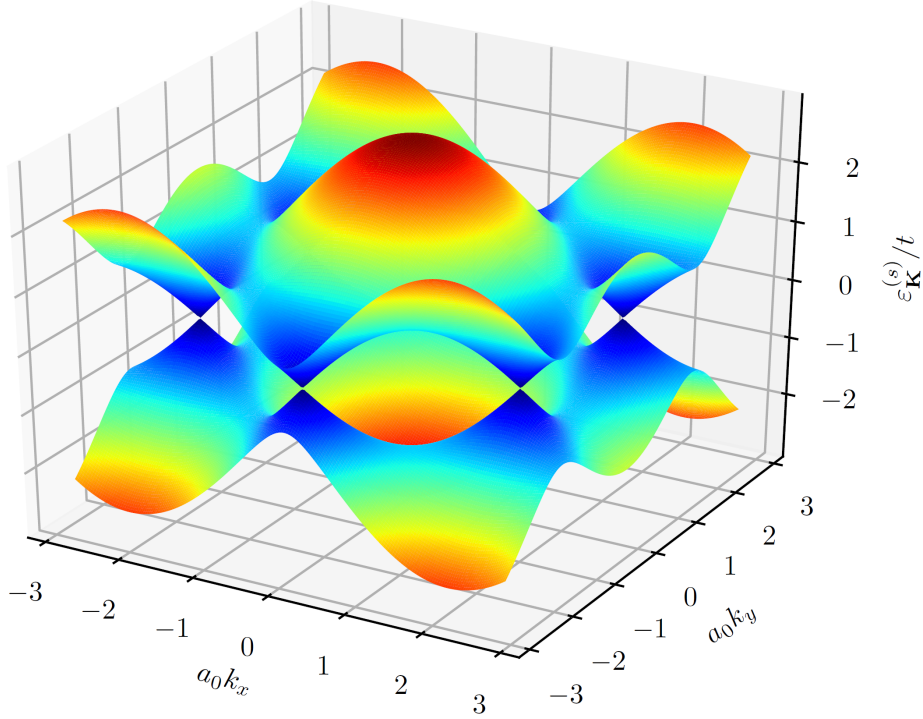
Figure 1.2
Electronic dispersion of single-layer graphene. The conductance and valence bands touch each other at six Dirac points in reciprocal space.

where **p** is a 2D momentum vector in the xy plane. Explicitly:

$$
i\hbar\frac{\partial}{\partial t}\begin{pmatrix}\Psi_1\\\Psi_2\\\Psi_3\\\Psi_4\end{pmatrix}=\begin{pmatrix}mc^2 & 0 & 0 & c(p_x-ip_y)\\0 & mc^2 & c(p_x+ip_y) & 0\\0 & c(p_x-ip_y) & -mc^2 & 0\\c(p_x+ip_y) & 0 & 0 & -mc^2\end{pmatrix}\begin{pmatrix}\Psi_1\\\Psi_2\\\Psi_3\\\Psi_4\end{pmatrix}. \tag{1.16}
$$

Now I can decompose the previous equation and write it as two equations:

$$
i\hbar\frac{\partial}{\partial t}\begin{pmatrix}\Psi_1\\\Psi_4\end{pmatrix}=\begin{pmatrix}mc^2 & c(p_x-ip_y)\\c(p_x+ip_y) & -mc^2\end{pmatrix}\begin{pmatrix}\Psi_1\\\Psi_4\end{pmatrix}, \tag{1.17}
$$

$$
i\hbar\frac{\partial}{\partial t}\begin{pmatrix}\Psi_2\\\Psi_3\end{pmatrix}=\begin{pmatrix}mc^2 & c(p_x+ip_y)\\c(p_x-ip_y) & -mc^2\end{pmatrix}\begin{pmatrix}\Psi_2\\\Psi_3\end{pmatrix}. \tag{1.18}
$$

5

The two matrix representations of the Hamiltonian of Eqs. (1.17,1.18) are the same that we had before about single-layer graphene (Eqs. (1.13,1.14)), but in the latter case the electrons behave like some massless pseudoparticles which move with the Fermi velocity (v_F), not the speed of light. This is the reason that we say electrons in graphene behave like relativistic particles that have no rest mass.

1.2 Bilayer graphene

Experimentally, the graphene bilayer exists in three different structures: AA, AB (the so-called Bernal phase), and the twisted bilayer. The AA structure is the simplest one: all the carbon atoms of the second layer are located exactly above the carbon atoms of the first layer. However, this structure is not stable and therefore its manufacture was reported only in a few pieces of literature [58, 52, 51, 12]. The AB bilayer is made by shifting the second layer of the AA structure by a carbon-carbon bond length and in the same direction. Therefore, half of the carbon atoms of the second layer are on top of the carbon atoms of the lower layer, and the other atoms are located above the centers of the lower layer hexagons, like the construction of successive layers in natural graphite. The AB bilayer is the most stable bilayer and high-quality samples were produced and studied in many experiments [107, 57]. The third type of bilayer graphene structure is the twisted bilayer. In this case, one of the graphene sheets is rotated with respect to the other layer by an angle θ [27]. Samples with this structure are produced using some special technological processes and are stable like the Bernal structure. These three types of bilayer structures have rather different electronic properties. In the following two subsections, we briefly introduce the AA and AB-stacked bilayers. Then we will give an almost comprehensive discussion of twisted bilayer graphene.

1.2.1 AA-stacked bilayer graphene

The main objective in this section is to derive the electronic spectrum of AA-stacked bilayer graphene. Fig. 1.3 shows the crystal structure of this system. The AA-stacked bilayer is composed of two graphene layers; 1 and 2. In the upper layer, each carbon atom is positioned above the corresponding atom of the lower layer.

Since the hexagonal structure of each graphene layer consists of two triangular sublattices, A and B, there are four carbon atoms in each unit cell of this bilayer system, which we call A_1, A_2, B_1, and B_2. A tight-binding Hamiltonian, based on the p_z orbitals of each atom, is used to model the system. By including both in-plane and interplane tunneling, the Hamiltonian is expressed as [87]:

$$\hat{H} = -t\sum_{\langle ij \rangle \sigma} a^{\dagger}_{i\alpha\sigma} b^{\dagger}_{j\alpha\sigma} + t_0 \sum_{i\sigma}\left(a^{\dagger}_{i1\sigma}a_{i2\sigma} + b^{\dagger}_{i1\sigma}b_{i2\sigma}\right) - t'\sum_{\langle\langle ij \rangle\rangle \alpha\sigma}\left(a^{\dagger}_{i\alpha\sigma}a_{j\alpha\sigma} + b^{\dagger}_{i\alpha\sigma}b_{j\alpha\sigma}\right)$$
$$+ t_g \sum_{\langle ij \rangle \sigma}\left(a^{\dagger}_{i1\sigma}b_{j2\sigma} + a^{\dagger}_{i2\sigma}b_{j1\sigma}\right) + \text{H.c.} \tag{1.19}$$
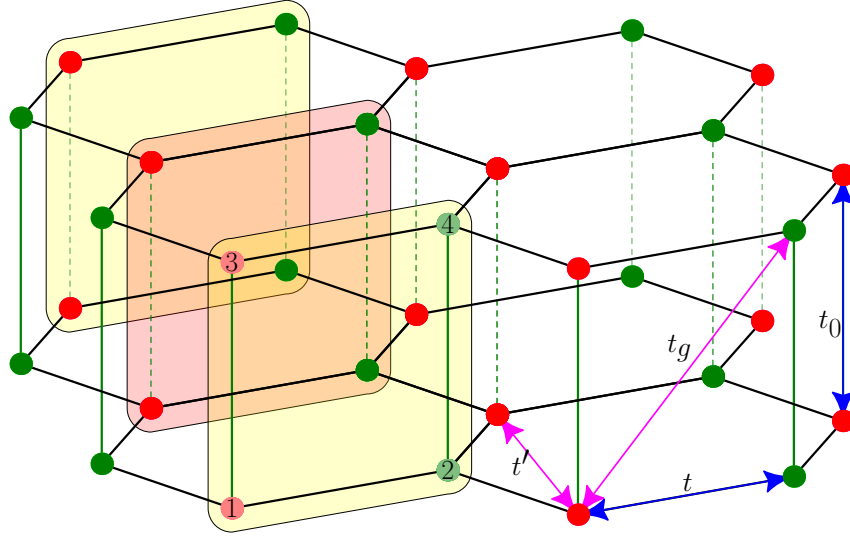
Figure 1.3

Crystal structure of the AA-stacked bilayer graphene. The circles demonstrate carbon atoms in the A (red) and B (green) sublattices in the bottom (1) and top (2) layers. The unit cell is composed of four atoms and illustrated by yellow and orang foursquares. Hopping integrals t and t' match the in-plane nearest and next-nearest-neighbor hopping, t_0 and t_g match the interplane nearest and next-nearest-neighbor hopping.

Here, the first term is the in-plane nearest-neighbor hopping of a graphene sheet [see Eq. (1.3)], the second term represents the nearest-neighbor inter-plane hopping with amplitude t_0, the third and the fourth terms relates to the in-plane and interplane next-nearest-neighbor hopping with amplitudes t' and t_g, respectively. We use the symbol $\langle\langle\cdots\rangle\rangle$ to show the summation over the next-nearest-neighbor sites. Using *ab initio* calculations and tight-binding fit to experiments, it is possible to calculate the hopping integral values. A well-established value for t is $t = 2.5 - 3$ eV [72, 20, 13, 30]. The interplane nearest-neighbor hopping integral is $t_0 = 0.3 - 0.4$ eV [72, 20, 13, 30]. About t', an *ab initio* calculations performed by S. Reich et al. [88] indicate $0.02t < t' < 0.2t$ depend on in-plane nearest-neighbor hopping. Furthermore, Deacon et al. [24] using an experimental method, verified this small value. They found $t' \approx 0.1$ eV. The interplane next-nearest-neighbor integral t_g is signicantly smaller than the others. Based on *ab initio* calculations in Ref. [13], $t_g \approx 0.03$ eV.

At first, we ignore next-nearest-neighbor hoppings and simply considering the first two terms in Hamiltonian (1.19) (the last two terms will be added to the model at the end of this section). Each unit cell of the AA bilayer has four atoms, therefore the electronic spectrum consists of four bands $\varepsilon_{0\mathbf{k}}^s$, where $s = 1, 2, 3, 4$. We can obtain the eigenenergies $\varepsilon_{0\mathbf{k}}^s$ by a similar method that we used for the single-layer graphene. We need to transform Hamiltonian (1.19) into $\mathbf{k}$–space, and define a four-component

spinor as follows:

$$\Psi_{\mathbf{k}\sigma} = (a_{\mathbf{k}1\sigma}, a_{\mathbf{k}2\sigma}, b_{\mathbf{k}1\sigma}, b_{\mathbf{k}2\sigma},)^T. \tag{1.20}$$

By ignoring next-nearest-neighbor hopping, Hamiltonian (1.19) can be expressed as

$$H = \sum_{\mathbf{k}\sigma} \Psi_{\mathbf{k}\sigma}^\dagger \hat{H}_{\mathbf{k}} \Psi_{\mathbf{k}\sigma}$$

where $\hat{H}_{\mathbf{k}}$ is a 4×4 matrix:

$$\hat{H}_{\mathbf{k}} = \begin{pmatrix} 0 & t_0 & -tf(\mathbf{k}) & 0 \\ t_0 & 0 & 0 & -tf(\mathbf{k}) \\ -tf^*(\mathbf{k}) & 0 & 0 & t_0 \\ 0 & -tf^*(\mathbf{k}) & t_0 & 0 \end{pmatrix} \tag{1.21}$$

The spectrum of this Hamiltonian contains four energy bands

$$\varepsilon_{0\mathbf{k}}^{(1)} = -t_0 - t|f(\mathbf{k})|, \quad \varepsilon_{0\mathbf{k}}^{(2)} = +t_0 - t|f(\mathbf{k})|,$$
$$\varepsilon_{0\mathbf{k}}^{(3)} = -t_0 + t|f(\mathbf{k})|, \quad \varepsilon_{0\mathbf{k}}^{(4)} = +t_0 + t|f(\mathbf{k})|, \tag{1.22}$$

which are plotted in Fig. 1.4. This spectrum is made of two copies of the single-layer graphene spectrum. One copy (bands 2 and 4) is shifted to higher energies by the amount t_0 while the other copy (bands 1 and 3) is shifted down by the same value. In this approximation the spectrum has electron-hole symmetry. Near the Dirac points, bands 1 and 2 are hole-like, while bands 3 and 4 are electron-like. An electron-hole transformation exchanges the bands 1 and 4 and also 2 and 3. There is no difference between the rst Brillouin zone of this system (panel (b) of Fig. 1.4) and that for single-layer graphene (see Fig. 1.1). For a pure AA-stacked bilayer, bands 2 and 3 go across the Fermi level near the Dirac points $\mathbf{K}$ and $\mathbf{K}'$. This statement leads us to an equation for the Fermi surface. Using Eq. (1.22) we find $|f(\mathbf{k})| = t_0/t$. Since $t_0/t \ll 1$, we can expand the function $|f(\mathbf{k})|$ near the Dirac points and keep only the linear term. Doing this computation we nd that the Fermi surface consists of two circles with radius $k_r = 2t_0/(3ta_0)$. As a result, the AA-stacked bilayer graphene is an electrical conductor even in the case of zero doping.

Fig. 1.4 illustrates the spectrum of the AA-stacked bilayer graphene, linear in the vicinity of the Dirac points (similar to the case of single-layer graphene). By expanding Eq. (1.22) in powers of $|\mathbf{q}| = |\mathbf{K} - \mathbf{k}|, |\mathbf{K}' - \mathbf{k}| \ll |\mathbf{K}|$, we derive the linear approximation

$$\varepsilon_{0\mathbf{K}+\mathbf{q}}^{1,2,3,4} = \mp t_0 \mp \hbar v_F |\mathbf{q}|,$$

where v_F is the Fermi velocity for the AA-stacked bilayer, which is the same as for single-layer graphene.
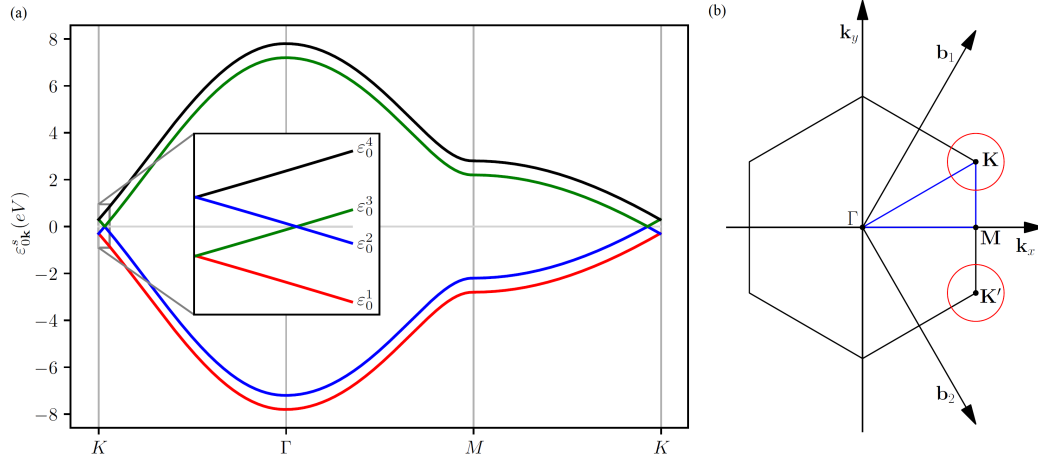
Figure 1.4
a) Band structure of AA-stacked bilayer graphene without the next-nearest-neighbor hopping. The spectrum is composed of two copies of the single-layer graphene spectrum, one of them is shifted to higher energies and the other to lower energies. In this approximation the spectrum has electron-hole symmetry. b) The system has the same first Brillouin zone as single-layer graphene. The two red circles show the two branches of the degenerate Fermi surface around Dirac points.

Adding next-nearest-neighbors hopping terms into the model breaks electron-hole symmetry. Thus, the Hamiltonian in k-representation becomes

$$\hat{H}_{\mathbf{k}} = \begin{pmatrix} -t'F(\mathbf{k}) & t_0 & -tf(\mathbf{k}) & t_g f(\mathbf{k}) \\ t_0 & -t'F(\mathbf{k}) & t_g f(\mathbf{k}) & -tf(\mathbf{k}) \\ -tf^*(\mathbf{k}) & t_g f^*(\mathbf{k}) & -t'F(\mathbf{k}) & t_0 \\ t_g f^*(\mathbf{k}) & -tf^*(\mathbf{k}) & t_0 & -t'F(\mathbf{k}) \end{pmatrix} \tag{1.23}$$

where

$$F(\mathbf{k}) = |f(\mathbf{k})|^2 - 3 = 2\cos(\sqrt{3}k_y a_0) + 4\cos\left(\frac{\sqrt{3}k_y a_0}{2}\right)\cos\left(\frac{3k_x a_0}{2}\right).$$

In this case, the electron bands satisfy the equations

$$\varepsilon_{\mathbf{k}}^{(1)} = -t'F(\mathbf{k}) - t_0 - (t + t_g)|f(\mathbf{k})|, \qquad \varepsilon_{\mathbf{k}}^{(2)} = -t'F(\mathbf{k}) + t_0 - (t - t_g)|f(\mathbf{k})|,$$
$$\varepsilon_{\mathbf{k}}^{(3)} = -t'F(\mathbf{k}) - t_0 + (t + t_g)|f(\mathbf{k})|, \qquad \varepsilon_{\mathbf{k}}^{(4)} = -t'F(\mathbf{k}) + t_0 + (t - t_g)|f(\mathbf{k})|. \tag{1.24}$$

By expanding around the Dirac point, up to the first order in $|\mathbf{q}|$, we find

$$\varepsilon_{\mathbf{q}}^{(1,2)} = 3t' \mp t_0 - \hbar v_F \left(1 \pm \frac{t_g}{t}\right)|\mathbf{q}|, \qquad \varepsilon_{\mathbf{q}}^{(3,4)} = 3t' \mp t_0 + \hbar v_F \left(1 \pm \frac{t_g}{t}\right)|\mathbf{q}|, \tag{1.25}$$

9

The first term of these equations, $3t'$, is the same for all four bands. This means the in-plane next-nearest-neighbor hopping t' only shifts the position of the Fermi level and can be absorbed into the chemical potential μ. But the interlayer next-nearest-neighbor hopping t_g has a different effect: it remarkably breaks electron-hole symmetry and leads to unequal renormalized Fermi velocities for electrons and holes. This asymmetric band structure is shown in the left panel of Fig. 1.5.
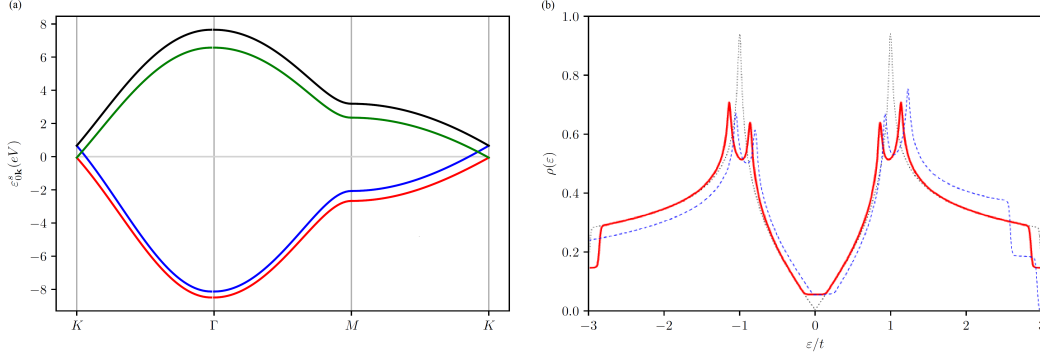
Figure 1.5
a) Band structure of AA-stacked bilayer graphene with next-nearest-neighbor hopping. The electron-hole symmetry is broken due to the interlayer next-nearest-neighbor hopping. b) The density of states of the AA-stacked bilayer graphene. The red solid curve corresponds to $t_g = 0$ and $t' = 0$, while the blue dashed curve is calculated for $t_g = 0.03\ eV$ and $t' = 0.1\ eV$. For both cases $t = 2.57\ eV$, $t_0 = 0.36\ eV$. The black dotted curve shows the density of states of single-layer graphene ($t' = 0$) which is shown for comparison.

The following expression can be used to calculate the density of states of the AA-stacked bilayer graphene

$$\rho(\varepsilon) = \sum_s \int_{V_{BZ}} \frac{d^2\mathbf{k}}{V_{BZ}} \delta\left(\varepsilon - \varepsilon_{\mathbf{k}}^{(s)}\right)$$

the integration should be taken over the first Brillouin zone $V_{BZ} = 8\pi^2/3\sqrt{3}a_0^2$, and $\delta(\varepsilon - \varepsilon_{\mathbf{k}})$ is the Dirac delta-function. The results are shown in the right panel of Fig. (1.5). This calculation was done with and without the next-nearest-neighbor hopping terms and demonstrates that the system has a non-zero density of states near the Fermi-level (the system is undoped in this calculation). The function $\rho(\varepsilon)$ is flat near $\varepsilon = 0$, or in the other hand the DOS is almost constant in the energy range $|\varepsilon| < t_0$. The figure shows four van Hove singularities, inherited from the single-layer graphene spectrum. Adding the next-nearest-neighbor hopping terms to the system violates the electron-hole symmetry of the DOS (blue dotted curve of Fig. 1.5(b)). This deviation is very fragile, particularly in an energy range smaller than van Hove singularities.

10

1.2.2 AB-stacked bilayer graphene

To construct an AB, or Bernal stacked bilayer (see Fig. 1.6) we can start from the AA-stacked bilayer and then shift one of the layers by the vector $\boldsymbol{\delta}_3$ shown in Fig. 1.1. This displacement locates the sublattice A of the shifted layer at the top of sublattice B of the fixed layer. Two sites from two layers which are opposite to each other are called dimer sites whereas the sites of one layer which are opposite to the hexagonal center of of the other layer are called non-dimer sites. The special form and also the position of
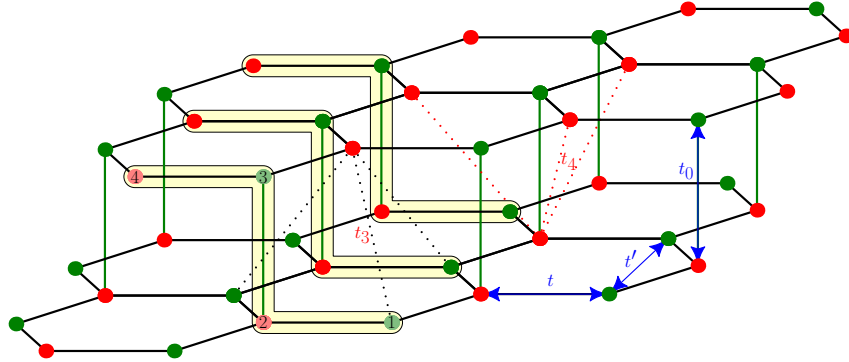
Figure 1.6
Crystal structure of the AB or Bernal stacked bilayer graphene. The only difference with the AA-stacked bilayer is that case the top layer was shifted by the vector $\boldsymbol{\delta}_3$. Two carbon atoms connected with green vertical lines make a dimer site with hopping integral t_0. The non-dimer sites are located against the central points of the hexagons in the opposite layer. The hopping from a non-dimer site to nearest non-dimer sites in the opposite layer is shown by t_3 (black dotted lines) while t_4 shows the hopping from a dimer site to nearest non-dimer sites of the opposite layer (red dotted lines).

p-orbitals of carbon atoms entails that the strongest interlayer hopping amplitude t_0 is between dimer sites. The simplest description of the AB bilayer is a model that includes only these tunneling amplitudes. Using this simple approximation and the notation of Eq. (1.21), we can write the Hamiltonian in **k**-space as follows:

$$\hat{H}_{\mathbf{k}}^{AB} = \begin{pmatrix} 0 & 0 & -tf(\mathbf{k}) & 0 \\ 0 & 0 & t_0 & -tf(\mathbf{k}) \\ -tf^*(\mathbf{k}) & t_0 & 0 & 0 \\ 0 & -tf^*(\mathbf{k}) & 0 & 0 \end{pmatrix} \tag{1.26}$$

For the Bernal bilayer, the parameters of the Hamiltonian are estimated as [62, 55]

$$2.9 \text{ eV} \leq t \leq 3.16 \text{ eV}, \qquad 0.3 \text{ eV} \leq t_0 \leq 0.4 \text{ eV}.$$

11

The matrix of Eq. (1.26) is easy to diagonalize. The corresponding eigenvalues satisfy the following equation

$$\varepsilon^4 - 2\varepsilon^2 \left(t^2 |f(\mathbf{k})|^2 + \frac{1}{2} t_0^2 \right) + t^4 |f(\mathbf{k})|^4 = 0 \tag{1.27}$$

which can be solved to nd the following four bands

$$\left(\varepsilon_{\mathbf{k}}^{(1,4)} \right)^2 = t^2 |f(\mathbf{k})|^2 + \frac{1}{2} t_0^2 + \sqrt{ t_0^2 t^2 |f(\mathbf{k})|^2 + \frac{1}{4} t_0^4 },$$

$$\left(\varepsilon_{\mathbf{k}}^{(2,3)} \right)^2 = t^2 |f(\mathbf{k})|^2 + \frac{1}{2} t_0^2 - \sqrt{ t_0^2 t^2 |f(\mathbf{k})|^2 + \frac{1}{4} t_0^4 }. \tag{1.28}$$

These bands are plotted in Fig. 1.7. Near the Dirac points $\mathbf{K}$ (or $\mathbf{K}'$), where
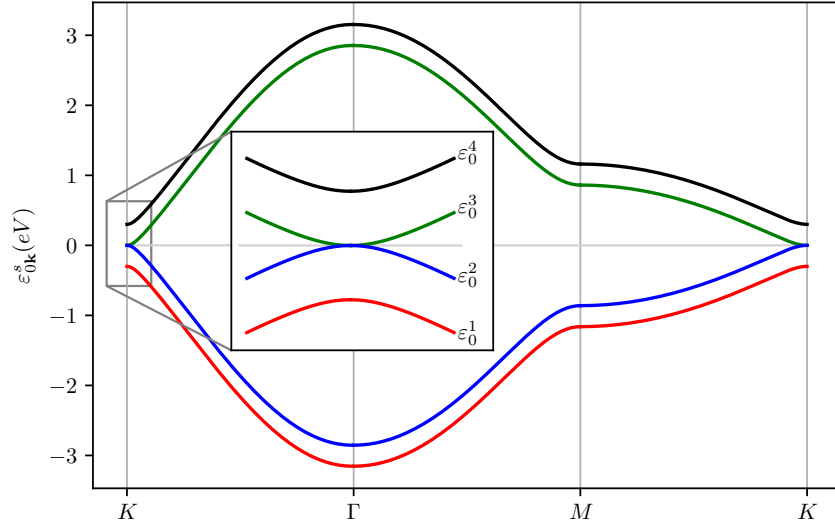
Figure 1.7

Single-particle band structure of AB-stacked bilayer graphene. The Hamiltonian in this calculation includes only the nearest-neighbor hopping integrals. The spectra of both AA and AB bilayers look like each other for large energies. But near the Dirac points they have quite different structures. For the AA-stacked graphene (see Fig. 1.4), the Fermi surface are two degenerate circles while in this case we see two Fermi points where two parabolic bands touch each other (the inset zooms on the area around the Dirac point).

$$|f(\mathbf{k})| \ll \frac{t_0}{2t}$$

we can expand the equation (1.28) and derive the following approximate formulas for the energy bands

$$\varepsilon_{\mathbf{K+q}}^{(1,4)} \approx \pm \left(t_0 + \frac{t^2}{t_0} |f(\mathbf{k})|^2 \right) \approx \pm \left(t_0 + \frac{\hbar^2 v_F^2}{t_0} |\mathbf{q}|^2 \right),$$

$$\varepsilon_{\mathbf{K+q}}^{(2,3)} \approx \pm \frac{t^2}{t_0} |f(\mathbf{k})|^2 \approx \pm \frac{\hbar^2 v_F^2}{t_0} |\mathbf{q}|^2, \qquad (1.29)$$

where we used Eq. (1.13) for v_F. Unlike both the monolayer and AA-stacked graphene, the band structure of this system has a parabolic dispersion near the Dirac points. The bands $s = 2, 3$ touch each other at K and K' points while the other bands ($s = 1, 4$) are separated by an energy gap.

Including the hopping terms from non-dimer sites of one layer to non-dimer sites of the other layer will modify the dispersion relation in Eq. (1.29). These hopping terms are shown by the black dotted line and labeled by t_3 in Fig. 1.7. The corresponding Hamiltonian matrix is

$$\hat{H}_{\mathbf{k}}^{AB} = - \begin{pmatrix} 0 & 0 & -tf(\mathbf{k}) & t_3 f^*(\mathbf{k}) \\ 0 & 0 & t_0 & -tf(\mathbf{k}) \\ -tf^*(\mathbf{k}) & t_0 & 0 & 0 \\ t_3 f(\mathbf{k}) & -tf^*(\mathbf{k}) & 0 & 0 \end{pmatrix} \qquad (1.30)$$

The spectrum of this matrix can be obtained by an analytical method [64], but here we show the results of a numerical solution [90]. Fig. 1.8 shows the band structure close to one of the Dirac points. The computation was done for non-zero t_3, whose value was obtained from experiment [50] and DFT calculations [20]:

$$t_3 = 0.3 \text{ eV}.$$

As the figure shows, adding t_3 to the tight-binding Hamiltonian replaces the parabolic dispersion near the $\mathbf{K}$ and $\mathbf{K}'$ points by a structure including four Dirac cones. The apexes of these cones lie at the Fermi energy. The central apex coincides with a corner of the Brillouin zone ($\mathbf{K}$, or $\mathbf{K}'$) and the others are shifted by a small quantity, p_L, from the corner . The figure also demonstrates six saddle points (three for $\varepsilon > 0$ and another three for $\varepsilon < 0$) at the energies $\varepsilon = \pm \varepsilon_L$ [64, 65]. This low-energy ne structure is called trigonal warping [64].

$$p_l = \frac{3a_0 t_0 t_3}{2\hbar^2 v_F^2} \approx 0.007 a_0^{-1}, \qquad \varepsilon_L = t_0 \left(\frac{3a_0 t_3}{4\hbar v_F} \right)^2 \approx 1 \text{ meV}. \qquad (1.31)$$

Both ε_L and p_L are quite small and probably become invisible in experimental measurements.
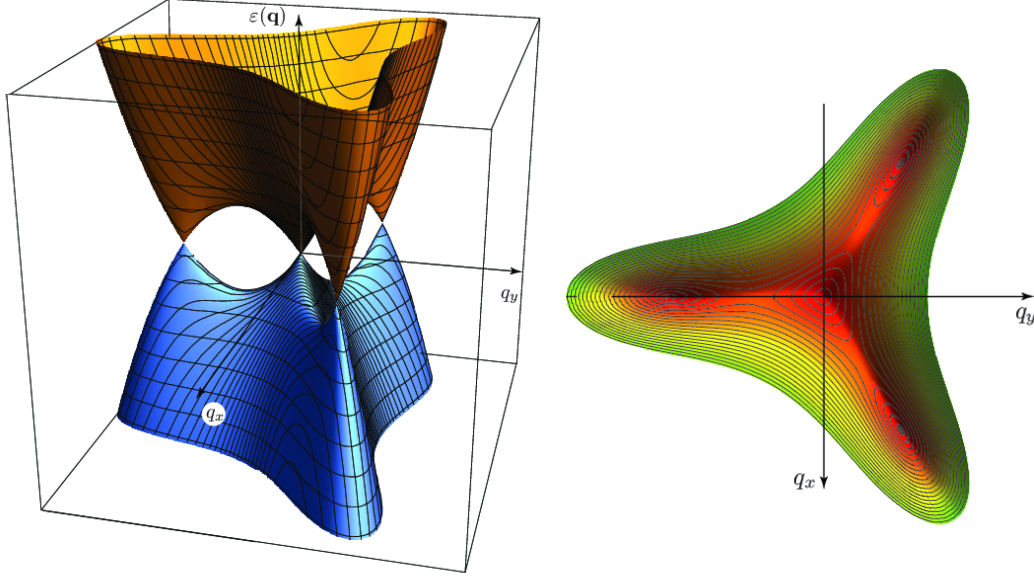
Figure 1.8
Trigonal warping. The interlayer hopping terms between non-dimer sites violate the parabolic dispersion at the Dirac point and reproduce four Dirac cones with linear dispersion. These Dirac cones are clear in the left panel. The right panel shows a top view of the same picture, with equal-energy contours. The origin of the coordinate system is set to a Dirac point and $q_{x,y}$ are momenta measured from the origin. The central cone is located at the corner of the Brillouin zone and the others are shifted from there by the amount p_L. This figure is taken from Ref. [90].

To match the experimental data with the theoretically-calculated dispersion, some additional hopping amplitudes and on-site energies should be added to the Hamiltonian [50, 61]. As an example, the hopping t_4 between dimer and non-dimer sites (red dotted lines in Fig. 1.6) leads to a small asymmetry between hole and electron states of the AB-stacked bilayer, which is an experimentally measurable effect.

1.3 Moiré structure

Consider an AA stacked bilayer graphene. Each A site of this system corresponds to a lattice vector. Any lattice vector is a linear combination of two primitive vectors of honeycomb lattice ($\mathbf{R}_{mn} = m\mathbf{a}_1 + n\mathbf{a}_2$). By defining the primitive lattice vectors of a 2D graphene system as

$$\mathbf{a}_1 = \left(\frac{\sqrt{3}}{2}, \frac{1}{2}\right)a \qquad , \mathbf{a}_2 = \left(\frac{\sqrt{3}}{2}, -\frac{1}{2}\right)a, \qquad (1.32)$$

we can express $\mathbf{R}_{mn}$ in the polar coordinates (see Fig. 1.9)

14
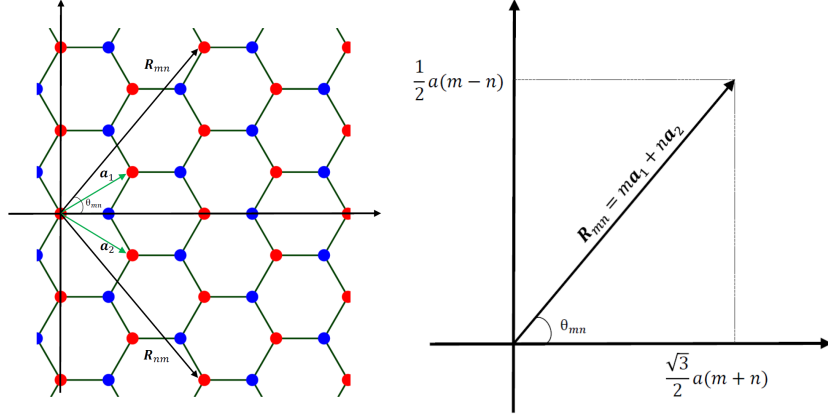
Figure 1.9
Left) AA stacked double layer graphene. $\mathbf{R}_{mn}$ is an arbitrary lattice vector which is a liniar combination of hexagonal primitive lattice vectors ($\mathbf{a}_1$, $\mathbf{a}_2$). Right) decomposition of $\mathbf{R}_{mn}$ to the x and y components.

$$\mathbf{R}_{mn} = m\mathbf{a}_1 + n\mathbf{a}_2 = m\left(\frac{\sqrt{3}}{2}, \frac{1}{2}\right)a + n\left(\frac{\sqrt{3}}{2}, -\frac{1}{2}\right)a = \frac{a}{2}\left(\sqrt{3}(m+n), (m-n)\right)$$

$$= a\sqrt{m^2 + n^2 + mn}\left(\frac{\sqrt{3}}{2}\frac{(m+n)}{\sqrt{m^2+n^2+mn}}, \frac{1}{2}\frac{(m-n)}{\sqrt{m^2+n^2+mn}}\right)$$

$$= a\sqrt{m^2 + n^2 + mn}\,(\cos\theta_{mn}, \sin\theta_{mn}), \tag{1.33}$$

where a is the lattice constant. Since the honeycomb lattice is symmetric under reflection with respect to the x-axis, for a given $\mathbf{R}_{mn} = (R_x, R_y)$ there always exists a $\mathbf{R}_{nm} = n\mathbf{a}_1 + m\mathbf{a}_2 = (R_x, -R_y)$. Now if we rotate the top and bottom layer by θ_{mn} and $-\theta_{mn}$ respectively, $\mathbf{R}_{mn}$ (top layer)and $\mathbf{R}_{nm}$ (bottom layer) coincide with the x axis. $R_{mn}(1, 0)$ is a lattice vector for the moiré structure associated to the twist angle $\phi = 2\theta_{mn}$. Thus, for any choice of m and n we can find the commensurate angle and the moiré wavelength:

$$\tan\theta_{mn} = \frac{m-n}{\sqrt{3}(m+n)}, \quad R_{mn} = a\sqrt{m^2 + n^2 + mn}. \tag{1.34}$$

The rotation angle ϕ between two layer is such that

$$\cos\phi = \cos 2\theta_{mn} = \frac{1}{2}\frac{m^2 + n^2 + 4mn}{m^2 + n^2 + mn}.$$

Noting that $m-n$ and $m+n$ have the same parity (both of them are even or odd), we can use an equivalence equation $(m-n)/(m+n) = p/q$ to find a simple and familiar relation for moiré structure parameters:

$$\tan\theta_{mn} = \frac{m-n}{\sqrt{3}(m+n)} = \frac{1}{\sqrt{3}}\frac{p}{q}, \tag{1.35}$$

15

and for the moire wavelength:

$$
\begin{aligned}
R_{mn} = a\sqrt{m^2 + n^2 + mn} &= a\sqrt{\frac{3}{4}q^2 + \frac{1}{4}p^2} = \frac{ap}{2}\sqrt{3\frac{q^2}{p^2} + 1} \\
&= \frac{ap}{2}\sqrt{\cot^2\theta_{mn} + 1} = \frac{ap}{2\sin(\phi/2)}
\end{aligned}
\tag{1.36}
$$

The minimum value of p in Eq. (1.36) defines the primitive lattice vector of the moiré superlattice. By fixing $p = 1$ and q as an odd integer equal to $q = 2k+1$, we have:

$$
\mathbf{R} = \frac{a}{2\sin(\phi/2)}\hat{i}, \qquad \tan(\frac{\phi}{2}) = \frac{1}{\sqrt{3}}\frac{1}{2k+1},
\tag{1.37}
$$

where $\hat{i}$ is the unit vector along the x axis. The moiré lattice of TBG has a triangular structure, therefore we can obtain the other lattice vectors by doing a sixty degrees rotation around the z axis. For symmetry considerations we select the two following vectors as the primitive lattice vectors of this 2D moiré structure:

$$
\mathbf{R}_1^{(M)} = R(\frac{1}{2}, \frac{\sqrt{3}}{2}), \qquad \mathbf{R}_2^{(M)} = R(\frac{1}{2}, -\frac{\sqrt{3}}{2}),
\tag{1.38}
$$

the reciprocal lattice vectors are:

$$
\begin{aligned}
\mathbf{R}_1^{*(M)} &= \frac{2\pi}{R}(1, \frac{1}{\sqrt{3}}) = \frac{4\pi}{a}\sin(\frac{\phi}{2})(1, \frac{1}{\sqrt{3}}), \\
\mathbf{R}_2^{*(M)} &= \frac{2\pi}{R}(1, -\frac{1}{\sqrt{3}}) = \frac{4\pi}{a}\sin(\frac{\phi}{2})(1, -\frac{1}{\sqrt{3}}).
\end{aligned}
\tag{1.39}
$$

In Eq. (1.32) we define the primitive lattice vectors for a hexagonal lattice. The reciprocal lattice vectors associated to this definition are:

$$
\mathbf{a}_1^* = \frac{2\pi}{a\sqrt{3}}(1, \sqrt{3}), \qquad \mathbf{a}_2^* = \frac{2\pi}{a\sqrt{3}}(1, -\sqrt{3}),
\tag{1.40}
$$

after rotation of the two layers, the reciprocal lattice vectors of each of them become:

$$
\mathbf{a}_i^{*(T)} = R_z\left(\frac{\phi}{2}\right)\mathbf{a}_i^*, \quad \mathbf{a}_i^{*(B)} = R_z\left(\frac{-\phi}{2}\right)\mathbf{a}_i^*
\tag{1.41}
$$

where $R_z(\alpha)$ is a rotation by an angle α with respect to the z axis. The reciprocal lattice vectors of a moiré structure could be calculated using reciprocal lattice vectors of two graphene layers:

$$
\begin{aligned}
\mathbf{a}_1^{*(B)} - \mathbf{a}_1^{*(T)} &= R_z(\frac{-\phi}{2})\mathbf{a}_1^* - R_z(\frac{\phi}{2})\mathbf{a}_1^* = \frac{4\pi}{a}\sin\frac{\phi}{2}(1, -\frac{1}{\sqrt{3}}) \\
\mathbf{a}_2^{*(T)} - \mathbf{a}_2^{*(B)} &= R_z(\frac{\phi}{2})\mathbf{a}_2^* - R_z(\frac{-\phi}{2})\mathbf{a}_2^* = \frac{4\pi}{a}\sin\frac{\phi}{2}(1, \frac{1}{\sqrt{3}})
\end{aligned}
\tag{1.42}
$$

Eq. (1.42) shows the same results that we saw in Eq. (1.39) and this is another method to introduce the moiré structure. All these vectors are shematically shown in Fig. 1.10.
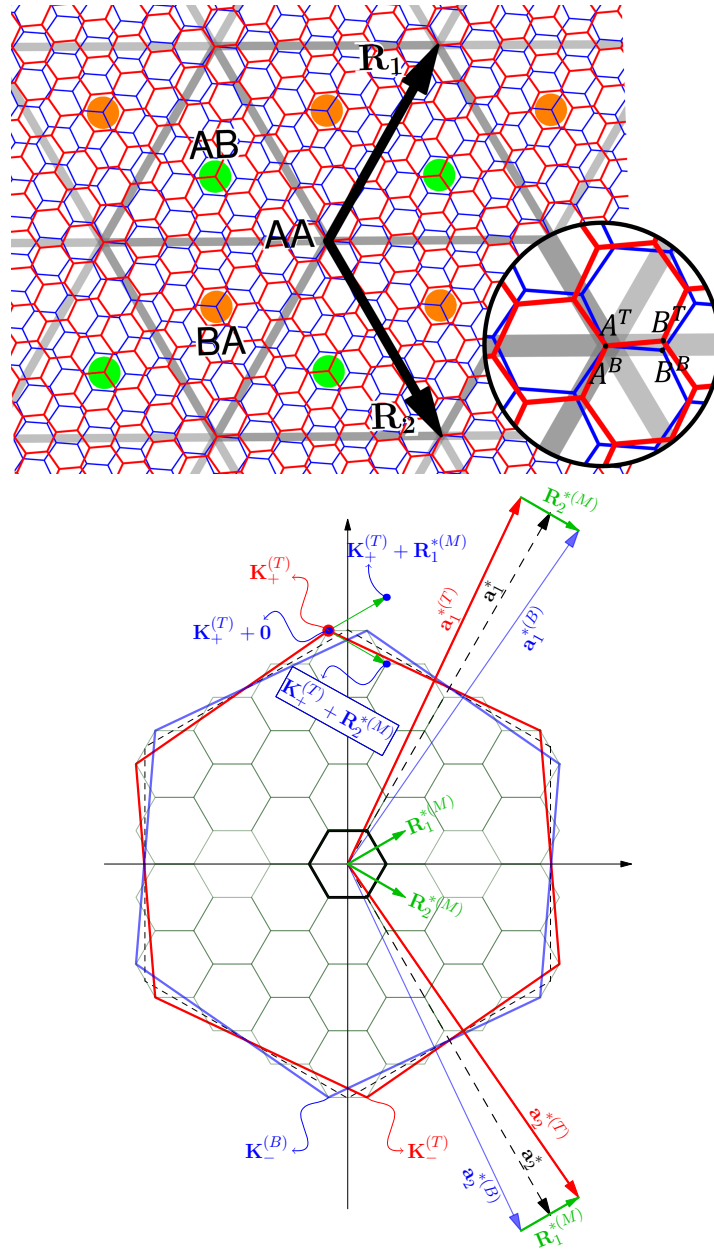
Figure 1.10
Top) Twisted bilayer graphene: two graphene layers are rotated by 9.43° with respect to each other. The triangular moiré lattice is shown by thick gray lines. AA spots (where the sublattice A of top layer is located over the sublattice A of bottom layer) are located at the triangular lattice sites, and AB and BA spots are at the centers of triangles indicated by green and orange dots. R_1 and R_2 are the lattice vectors of the moiré structure. Bottom) Brillouin zone folding in TBG. Two large hexagons (red and blue) represent the first Brillouin zones of graphene layers, and the small hexagon is the moiré Brillouin zone of TBG. Reciprocal lattice vectors are also shown in the picture, T and B are used to represent the top and bottom layers. An electron with the wave vector $\mathbf{k} = \mathbf{K}_+^{(T)}$ in the Dirac point of top layer (red point) is coupled with three electrons of the bottom layer with wave vectors, $\tilde{\mathbf{k}} = \mathbf{K}_+^{(T)}$, $\tilde{\mathbf{k}} = \mathbf{K}_+^{(T)} + \mathbf{R}_1^{*(M)}$ and $\tilde{\mathbf{k}} = \mathbf{K}_+^{(T)} + \mathbf{R}_2^{*(M)}$ (blue points) [see section 1.4.4].

17

1.4 Continuum model for multilayer systems

Incommensurate multilayer systems are a novel type of nanoscale materials made by stacking individual atomic layers over each other. In general, these systems don't have a common spatial period in their atomic structure and this is the reason why they are called incommensurate. In some recent experiments, several types of hybrid systems composed of different kinds of atomic layers were fabricated with acceptable quality. Twisted bilayer graphene (TBG) is a typical example of incommensurate multilayer systems [59, 18, 19]. Another well-known example is graphene hexagonal boron nitride (hBN), where hexagonal lattices with slightly dierent lattice constants are overlapped [25, 39, 109].

The interlayer interaction between incommensurate atomic layers frequently gives rise to remarkable physical properties that are absent in the individual atomic layers. When the adjacent layers have almost identical lattice structure, their slightly dierent periods interfere together and give rise to a long-period moiré pattern that signicantly modies the low-energy electronic spectrum. For example, in TBG, when the rotation angle is small enough, the Dirac cones of two single-layer graphenes are strongly coupled, leading to a remarkable reduction in the renormalized Fermi velocity [27, 28, 29, 9]. Theoretically, for the incommensurate multilayer systems the period of the translational symmetry is too large and then the moiré unit cell is too large for the usual band structure techniques like DFT.

When the period of the moiré superlattice is much longer than the atomic scale, however, it is possible to extract an eective continuum model, dependent on the moiré wavelength, using an appropriate coarse-graining process. The eective long-range theory was developed for TBG [43, 46, 45] and graphenehBN bilayer system [71, 105]. This theoretical method could be extended to general incommensurate systems in which the lattice structures are not close to each other [45].

1.4.1 Incommensurate Atomic Layers

This section presents a theoretical formulation to describe the electronic coupling between the incommensurate bilayers using the tight-binding approximation [45]. Our starting point is to define a general bilayer system composed of a pair of two-dimensional atomic layers with dierent crystal structures. We define the primitive lattice vectors as $\mathbf{a}_1$ and $\mathbf{a}_2$ for layer 1 and $\tilde{\mathbf{a}}_1$ and $\tilde{\mathbf{a}}_2$ for layer 2, which are assumed to be parallel with the (xy) plane of the coordinate system. The reciprocal lattice vectors for layer 1 and 2 are dened by $\mathbf{a}_i^*$ and $\tilde{\mathbf{a}}_i^*$, respectively, so as to satisfy $\mathbf{a}_i \cdot \mathbf{a}_j^* = \tilde{\mathbf{a}}_i \cdot \tilde{\mathbf{a}}_j^* = 2\pi\delta_{ij}$. The area of the unit cell is given by $S = |\mathbf{a}_1 \times \mathbf{a}_2|$ for layer 1, and $\tilde{S} = |\tilde{\mathbf{a}}_1 \times \tilde{\mathbf{a}}_2|$ for layer 2.

A unit cell that we define for each layer may contain dierent sublattices and/or multiple atomic orbitals. We introduce indices X for layer 1 and $\tilde{X}$ for layer 2, to specify the sublattice and orbital degrees of freedom. The positions of the lattice sites are given

by

$$\mathbf{R}_X = n_1\mathbf{a}_1 + n_2\mathbf{a}_2 + \boldsymbol{\tau}_X \qquad \text{(layer 1)},$$
$$\mathbf{R}_{\tilde{X}} = \tilde{n}_1\tilde{\mathbf{a}}_1 + \tilde{n}_2\tilde{\mathbf{a}}_2 + \boldsymbol{\tau}_{\tilde{X}} \qquad \text{(layer 2)}, \tag{1.43}$$

where n_i and $\tilde{n}_i$ are integers, and $\boldsymbol{\tau}_X$ and $\boldsymbol{\tau}_{\tilde{X}}$ are used to show the sublattice position inside the unit cell. Let us dene $|\mathbf{R}_X\rangle = \phi_X(\mathbf{r} - \mathbf{R}_X)$ as the atomic orbital of X localized at $\mathbf{R}_X$. The atomic orbital ϕ_X may depend on the sublattice. We define $-T_{\tilde{X}X}(\mathbf{R}_{\tilde{X}} - \mathbf{R}_X)$ as the transfer integral from the site $\mathbf{R}_X$ to $\mathbf{R}_{\tilde{X}}$. This quantity depends on the relative position $\mathbf{R}_{\tilde{X}} - \mathbf{R}_X$ and also on the type of atomic orbitals of X and $\tilde{X}$. The interlayer Hamiltonian to couple the layer 1 and 2 is then written as

$$\mathscr{H} = -\sum_{X,\tilde{X}} T_{\tilde{X},X}(\mathbf{R}_{\tilde{X}} - \mathbf{R}_X)|\mathbf{R}_{\tilde{X}}\rangle\langle\mathbf{R}_X| + H.c. \tag{1.44}$$

Now let us dene the Bloch bases as

$$|\mathbf{k},X\rangle = \frac{1}{\sqrt{N}} \sum_{\mathbf{R}_X} e^{i\mathbf{k}\cdot\mathbf{R}_X}|\mathbf{R}_X\rangle \qquad \text{(layer 1)},$$

$$|\tilde{\mathbf{k}},\tilde{X}\rangle = \frac{1}{\sqrt{\tilde{N}}} \sum_{\mathbf{R}_{\tilde{X}}} e^{i\tilde{\mathbf{k}}\cdot\mathbf{R}_{\tilde{X}}}|\mathbf{R}_{\tilde{X}}\rangle \qquad \text{(layer 2)}, \tag{1.45}$$

where $\mathbf{k}$ and $\tilde{\mathbf{k}}$ are the two-dimensional Bloch wave vectors respectively for layer 1 and 2. $N = S_{tot}/S$ ($\tilde{N} = S_{tot}/\tilde{S}$) is the number of unit cell of layer 1 (2) in the total system area S_{tot}.

The matrix elements of interlayer Hamiltonian, $\mathscr{H}$, between Bloch bases can be written as [45]

$$\begin{aligned}
\mathscr{H}_{\tilde{X},X}(\tilde{\mathbf{k}},\mathbf{k}) &= \langle\tilde{\mathbf{k}},\tilde{X}|\mathscr{H}|\mathbf{k},X\rangle \\
&= \frac{1}{\sqrt{\tilde{N}N}} \sum_{\mathbf{R}_{\tilde{X}}}\sum_{\mathbf{R}_X} e^{-i\tilde{\mathbf{k}}\cdot\mathbf{R}_{\tilde{X}}} e^{i\mathbf{k}\cdot\mathbf{R}_X} \langle\mathbf{R}_{\tilde{X}}|\mathscr{H}|\mathbf{R}_X\rangle \\
&= -\frac{1}{\sqrt{\tilde{N}N}} \sum_{\mathbf{R}_{\tilde{X}}}\sum_{\mathbf{R}_X} e^{-i\tilde{\mathbf{k}}\cdot\mathbf{R}_{\tilde{X}}} e^{i\mathbf{k}\cdot\mathbf{R}_X} \times \left[T_{\tilde{X},X}(\mathbf{R}_{\tilde{X}} - \mathbf{R}_X)\right] \\
&= -\frac{1}{\sqrt{\tilde{N}N}} \sum_{\mathbf{R}_X} e^{i(\mathbf{k}-\tilde{\mathbf{k}})\cdot\mathbf{R}_X} \sum_{\mathbf{R}_{\tilde{X}}} T_{\tilde{X},X}(\mathbf{R}_{\tilde{X}} - \mathbf{R}_X) e^{-i\tilde{\mathbf{k}}\cdot(\mathbf{R}_{\tilde{X}}-\mathbf{R}_X)}. \tag{1.46}
\end{aligned}$$

To simplify the second summation in the right-hand side of Eq. (1.46) we need to define the in-plane Fourier transform of the transfer integral as

$$t_{\tilde{X}X}(\mathbf{q}) = \frac{1}{\sqrt{\tilde{S}S}} \int T_{\tilde{X}X}\left(\mathbf{r} + z_{\tilde{X}X}\mathbf{e}_z\right) e^{-i\mathbf{q}\cdot\mathbf{r}} d^2r, \tag{1.47}$$

19

and the inverse Fourier transform is:

$$T_{\tilde{X}X}\left(\mathbf{r} + z_{\tilde{X}X}\mathbf{e}_z\right) = \frac{1}{\sqrt{\tilde{N}N}} \int t_{\tilde{X}X}(\mathbf{q})e^{i\mathbf{q}\cdot\mathbf{r}}d^2q. \tag{1.48}$$

By applying the inverse Fourier transform to equation (1.46), the second summation is transformed as

$$\sum_{\mathbf{R}_{\tilde{X}}} T_{\tilde{X},X}(\mathbf{R}_{\tilde{X}} - \mathbf{R}_X)e^{-i\tilde{\mathbf{k}}\cdot(\mathbf{R}_{\tilde{X}} - \mathbf{R}_X)}$$

$$= \frac{1}{\sqrt{\tilde{N}N}} \int d^2q \; e^{i(\mathbf{q}-\tilde{\mathbf{k}})\cdot(\tau_{\tilde{X}} - \mathbf{R}_X)} t_{\tilde{X}X}(\mathbf{q}) \sum_{\tilde{n}_1\tilde{n}_2} e^{i(\mathbf{q}-\tilde{\mathbf{k}})\cdot(\tilde{n}_1\tilde{\mathbf{a}}_1 + \tilde{n}_2\tilde{\mathbf{a}}_2)}$$

$$= \sqrt{\frac{\tilde{N}}{N}} \sum_{\tilde{\mathbf{G}}} t_{\tilde{X}X}(\tilde{\mathbf{k}} + \tilde{\mathbf{G}})e^{i\tilde{\mathbf{G}}\cdot(\tau_{\tilde{X}} - \mathbf{R}_X)} \tag{1.49}$$

where in the last equation we used

$$\sum_{\tilde{n}_1\tilde{n}_2} e^{i(\mathbf{q}-\tilde{\mathbf{k}})\cdot(\tilde{n}_1\tilde{\mathbf{a}}_1 + \tilde{n}_2\tilde{\mathbf{a}}_2)} = \tilde{N} \sum_{\tilde{\mathbf{G}}} \delta_{\mathbf{q}-\tilde{\mathbf{k}},\tilde{\mathbf{G}}} \tag{1.50}$$

where $\tilde{\mathbf{G}} = \tilde{m}_1\tilde{\mathbf{a}}_1^* + \tilde{m}_2\tilde{\mathbf{a}}_2^*$ is a reciprocal lattice vector of layer 2 and we have a similar definition, $\mathbf{G} = m_1\mathbf{a}_1^* + m_2\mathbf{a}_2^*$, for layer 1. Using equations (1.46) and (1.49), we have

$$\mathcal{H}_{\tilde{X}X}(\tilde{\mathbf{k}},\mathbf{k}) = -\frac{1}{N} \sum_{\tilde{\mathbf{G}}} t_{\tilde{X}X}(\tilde{\mathbf{k}} + \tilde{\mathbf{G}})e^{i\tilde{\mathbf{G}}\cdot\tau_{\tilde{X}}} \sum_{\mathbf{R}_X} e^{i(\mathbf{k}-\tilde{\mathbf{k}}-\tilde{\mathbf{G}})\cdot\mathbf{R}_X}$$

$$= -\sum_{\mathbf{G}\tilde{\mathbf{G}}} t_{\tilde{X}X}(\mathbf{k} + \mathbf{G})e^{-i\mathbf{G}\cdot\tau_X + i\tilde{\mathbf{G}}\cdot\tau_{\tilde{X}}} \delta_{\mathbf{k}+\mathbf{G},\tilde{\mathbf{k}}+\tilde{\mathbf{G}}}, \tag{1.51}$$

where for the summation in $\mathbf{R}_X$ in the first line, we used the transformation

$$\sum_{\mathbf{R}_X} e^{i(\mathbf{k}-\tilde{\mathbf{k}}-\tilde{\mathbf{G}})\cdot\mathbf{R}_X} = \sum_{n_1 n_2} e^{i(\mathbf{k}-\tilde{\mathbf{k}}-\tilde{\mathbf{G}})\cdot(n_1\mathbf{a}_1 + n_2\mathbf{a}_2 + \tau_X)}$$

$$= e^{i(\mathbf{k}-\tilde{\mathbf{k}}-\tilde{\mathbf{G}})\cdot\tau_X} \sum_{n_1 n_2} e^{i(\mathbf{k}-\tilde{\mathbf{k}}-\tilde{\mathbf{G}})\cdot(n_1\mathbf{a}_1 + n_2\mathbf{a}_2)}$$

$$= e^{i(\mathbf{k}-\tilde{\mathbf{k}}-\tilde{\mathbf{G}})\cdot\tau_X} N \sum_{\mathbf{G}} \delta_{\mathbf{k}-\tilde{\mathbf{k}}-\tilde{\mathbf{G}},-\mathbf{G}}. \tag{1.52}$$

The matrix element Eq. (1.51) is non-zero only when

$$\mathbf{k} + \mathbf{G} = \tilde{\mathbf{k}} + \tilde{\mathbf{G}}. \tag{1.53}$$

According to Eq. (1.51), a Bloch wave number $\mathbf{k}$ in layer 1 has appropriate couplings with only a limited number of $\tilde{\mathbf{k}}$s in layer 2, because $t_{\tilde{X}X}(\mathbf{q})$ quickly decays in large q.

20

1.4.2 Long-period moiré superlattice

Consider a situation where the lattice structures of the two layers are close to each other. The interference of the slightly different atomic periods leads to an appearance of long-period moiré pattern, and we can describe the interlayer interaction by the eective long-wavelength Hamiltonian. Using the formulation presented in the previous section, it is possible to derive the eective theory of the general moiré superlattice just by assuming that the two layers have almost identical lattice structures [45]. We can use a linear transformation matrix A, to relate the primitive lattice vectors of layer 1 and 2 as

$$\tilde{\mathbf{a}}_i = A\mathbf{a}_i. \tag{1.54}$$

For instance, when the system is composed of two identical layers rotationally stacked with a small angle like in TBG, the transformation matrix is given by a rotation matrix R. When layer 1 and layer 2 have the same structure but with dierent lattice constants as in the graphenehBN bilayer, the matrix A is given by MR, which is a multiplication of the isotropic expansion matrix M, and the rotation matrix R. Correspondingly, the reciprocal lattice vectors become

$$\tilde{\mathbf{a}}_i^* = (A^\dagger)^{-1}\mathbf{a}_i^*. \tag{1.55}$$

to satisfy $\mathbf{a}_i \cdot \mathbf{a}_j^* = \tilde{\mathbf{a}}_i \cdot \tilde{\mathbf{a}}_j^* = 2\pi\delta_{ij}$. When the two layers have similar lattice structures, as we proved before in section 1.3 the reciprocal lattice vectors of the moiré superlattice is expressed by small dierence between $\mathbf{a}_i^*$ and $\tilde{\mathbf{a}}_i^*$ as

$$\mathbf{R}_i^{*(M)} = \mathbf{a}_i^* - \tilde{\mathbf{a}}_i^* = [1 - (A^\dagger)^{-1}]\mathbf{a}_i^*. \tag{1.56}$$

Consider the matrix A is nearly equals to the unit matrix, then $\mathbf{R}_1^{*(M)}$ and $\mathbf{R}_2^{*(M)}$ are very small vevtors and for any wave vector of layer 2 we can write

$$\tilde{\mathbf{k}} \approx \mathbf{k} + m_1\mathbf{R}_1^{*(M)} + m_2\mathbf{R}_2^{*(M)},$$

then, it is simple to determine the interlayer matrix elements for the long wavelength components using Eq. (1.51) as,

$$\mathscr{H}_{\tilde{X}X}(\mathbf{k} + m_1\mathbf{R}_1^{*(M)} + m_2\mathbf{R}_2^{*(M)}, \mathbf{k}) = t_{\tilde{X}X}(\mathbf{k} + m_1\mathbf{a}_1^* + m_2\mathbf{a}_2^*)$$
$$\times\, e^{-i(m_1\mathbf{a}_1^* + m_2\mathbf{a}_2^*)\cdot\boldsymbol{\tau}_X + i(m_1\tilde{\mathbf{a}}_1^* + m_2\tilde{\mathbf{a}}_2^*)\cdot\boldsymbol{\tau}_{\tilde{X}}}, \tag{1.57}$$

where m_1 and m_2 are integers. Since $t_{\tilde{X}X}(\mathbf{q})$ decays in large q, the couplings are considerable only for a few small values of m_1 and m_2.

1.4.3 Twisted Bilayer Graphene

We continue our discussion with twisted bilayer graphene (TBG), the system which is constructed by stacking a pair of hexagonal lattice with relative rotation angle ϕ. Let us

recall that the primitive lattice vectors of the two layers are defined by (T and B indices are used for top and bottom)

$$\mathbf{a}_i^{(T)} = R_z\left(\frac{\phi}{2}\right)\mathbf{a}_i, \quad \mathbf{a}_i^{(B)} = R_z\left(\frac{-\phi}{2}\right)\mathbf{a}_i, \tag{1.58}$$

where $R_z(\theta)$ is the rotation matrix and $\mathbf{a}_1$ and $\mathbf{a}_2$ are the primitive lattice vectors of the non rotated hexagonal lattice (Eq. (1.32)). In reciprocal space we have

$$\mathbf{a}_i^{*(T)} = R_z\left(\frac{\phi}{2}\right)\mathbf{a}_i^*, \quad \mathbf{a}_i^{*(B)} = R_z\left(\frac{-\phi}{2}\right)\mathbf{a}_i^* \tag{1.59}$$

where $\mathbf{a}_1^*$ and $\mathbf{a}_2^*$ are the reciprocal lattice vectors of the non rotated system defined at Eq. (1.40). As an example, the lattice vectors and the reciprocal lattice vectors for TBG at rotation angle $\theta = 10°$ are shown in Fig. 1.11. Each graphene layer contains two sublattices labeled by $X = A, B$ in its own unit cell. In the absence of the lattice distortion, the positions of sublattice X on layer l are given by:

$$\mathbf{R}_X^{(l)} = n_1\mathbf{a}_1^{(l)} + n_2\mathbf{a}_2^{(l)} + \boldsymbol{\tau}_X^{(l)}, \tag{1.60}$$

Here n_1 and n_2 are integers, and $\boldsymbol{\tau}_X^{(l)}$ is the relative sublattice position inside the unit cell, given by

$$
\begin{aligned}
\boldsymbol{\tau}_A^{(B)} &= 0, \\
\boldsymbol{\tau}_B^{(B)} &= \frac{1}{3}(\mathbf{a}_1^{(B)} + \mathbf{a}_2^{(B)}), \\
\boldsymbol{\tau}_A^{(T)} &= d\mathbf{e}_z + \boldsymbol{\tau}_0, \\
\boldsymbol{\tau}_B^{(T)} &= d\mathbf{e}_z + \boldsymbol{\tau}_0 + \frac{1}{3}(\mathbf{a}_1^{(T)} + \mathbf{a}_2^{(T)}),
\end{aligned}
\tag{1.61}
$$

where $d\mathbf{e}_z$ is the interlayer spacing vector. Here we take the origin at an A site, and $\boldsymbol{\tau}_0$ is the relative in-plane translation vector of layer 2 with respect to layer 1 [set to zero in Fig. 1.11a].
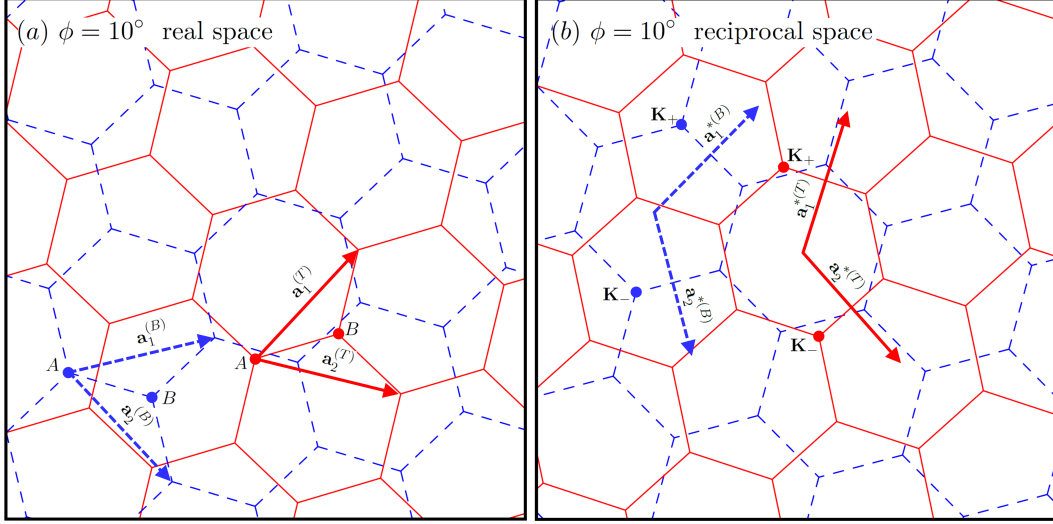
Figure 1.11
(a) Twisted bilayer graphene at rotation angle $\theta = 10°$. Top and bottom layers are shown by red and blue colors respectively (b) Brillouin zones of the individual layers in the extended zone scheme. Two Dirac points for each layer are shown by $\mathbf{K}_+$ and $\mathbf{K}_-$.

In TBG, when the rotation angle is small, $\theta \lesssim 10°$, the interference between the structures of two stacked lattice creates a moiré pattern with a period much greater than the atomic scale as shown in the top panels of Fig. 1.13, and then we can apply the general argument that we derived in Sect. 1.4.2. The moiré lattice vectors in real and reciprocal spaces were defined in Eqs. (1.38) and (1.39). Figure 1.12 illustrates the Brillouin zone reduction for TBG of $\theta = 10°$ and $\theta = 9.43°$. The graphene Dirac points (the band touching points) are located at

$$\mathbf{K}_\xi^{(l)} = R_z(\pm\frac{\phi}{2})\mathbf{K}_\xi \tag{1.62}$$

where

$$\mathbf{K}_\xi = \frac{\xi}{3}(\mathbf{a}_1^* - \mathbf{a}_2^*) = \xi\frac{4\pi}{3}(0,1), \tag{1.63}$$

is the Dirac points before rotation and $\xi = \pm 1$ is the valley index.

The electronic states around the Dirac points are the most important states to control the low-energy spectrum, therefore the states around the zone corners are all that is required to describe this spectrum. Since the **k**-space distance between $\mathbf{K}_+$ and $\mathbf{K}_-$ in each layer is much grater than the moiré reciprocal vector $\mathbf{R}_i^{*(M)}$, the interlayer couplings $\mathcal{H}$ can not lead to the hybridization of these two groups and it is possible to treat these distant valleys as independent subsystems. Then we can dene two separate superlattice mini-Brillouin zone near $\mathbf{K}_+^{(T\&B)}$ and $\mathbf{K}_-^{(T\&B)}$ (see Fig. 1.12(a)). The zone tiling pattern

near $\mathbf{K}_+^{(T\&B)}$ and that near $\mathbf{K}_-^{(T\&B)}$ are not generally consistent with each other, and this corresponds to the fact that there is no full commensurability between the moiré pattern and the atomic period of single layer graphene, i.e., the system does not have an exact translational symmetry as a whole. However, at some special rotation angles, a complete matching takes place between the atomic structures of the two layers and the whole structure becomes rigorously periodic. We have discussed the essential condition that leads to such a special commensurate situation previously in Sect. 1.3., where we demonstrate that, to have a commensurate moiré lattice, the exact superlattice period and the rotation angle θ should satisfy Eq. (1.37). Figure 1.12(b) shows the superlattice Brillouin zone for the commensurate TBG of $(m, n) = (3, 4)$ with $\theta \simeq 9.43°$. Having a well-defined translation symmetry with a finite period, we can define the common superlattice Brillouin zone for the entire system, and this is consistent with the tiling of the local zone near both $\mathbf{K}_+^{(T\&B)}$ and $\mathbf{K}_-^{(T\&B)}$ argued in Fig. 1.12(a). In a rigorous argument
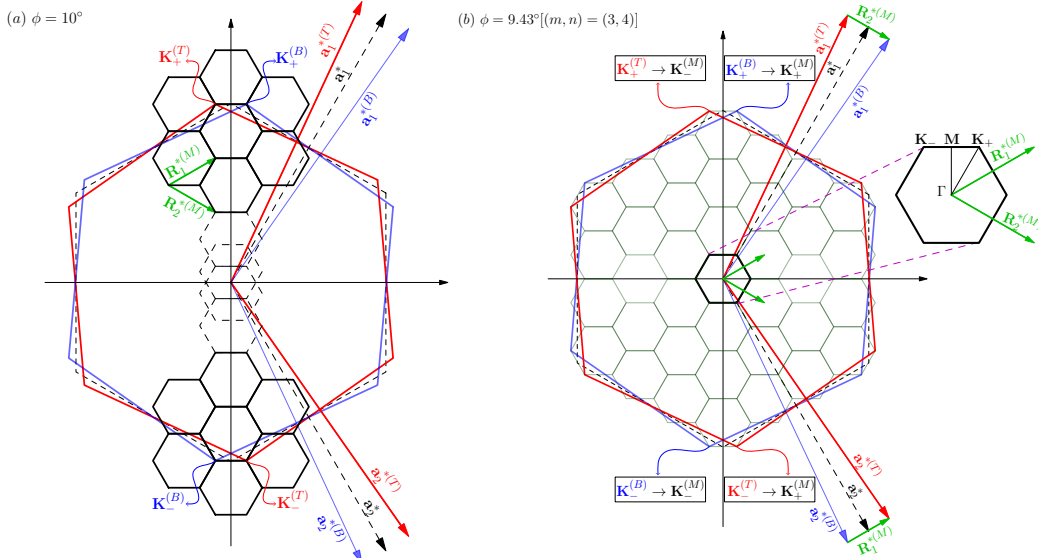
Figure 1.12

Brillouin zone reduction in (a) the incommensurate TBG with $\phi = 10°$ and (b) commensurate TBG with $\phi = 9.43°$ $[(m, n) = (3, 4)]$. The red and blue solid hexagons are the rst Brillouin zones of the top and bottom layers rotated by $\phi/2$ and $-\phi/2$ respectively. Black dashed hexagon is the rst Brillouin zone of the nontotated graphene layer. The small hexagons represent the folded superlattice Brillouin zones. Dirac points and primitive lattice vectors associated with each layer are shown in the figure.

the superlattice period L_S, and the period of the moiré structure, L_M, are not equal in general and the L_S is $|m - n|$ times greater than L_M. The superlattice period L_S is only dened at commensurate angles, while L_M is a continuous function of the rotation angle θ and always dened regardless of the commensurability. For small values of the rotation angle, the moiré pattern period L_M, is not too different of the superlattice period L_S,

and it is possible to show that the low-energy electronic properties are only influenced by moiré structure [68]. As a result, the effective continuum model described in the next section, eliminates the original lattice and leaves only the moiré superperiod.

1.4.4 Effective continuum model

In the following, we are going to derive the eective low-energy Hamiltonian for the small angle TBG system. Several methods were used to develop the effective theory of TBG, and the results are basically equivalent [68, 29, 27]. Here we derive the eective Hamiltonian using our general argument in Sect. (1.4.2) [45]. Our model is based on the single orbit tight-binding appriximation for p_z orbital of carbon atoms. We consider the transfer integral between any two orbitals is written in terms of the SlaterKoster form as [97],

$$-T(\mathbf{r}) = V_{pp\pi} \left[1 - \left(\frac{\mathbf{r} \cdot \mathbf{e}_z}{r} \right)^2 \right] + V_{pp\sigma} \left(\frac{\mathbf{r} \cdot \mathbf{e}_z}{r} \right)^2,$$
$$V_{pp\pi} = V_{pp\pi}^0 e^{-(r-a_0)/r_0}, \quad V_{pp\sigma} = V_{pp\sigma}^0 e^{-(r-d_0)/r_0}. \tag{1.64}$$

Here $\mathbf{e}_z$ is the unit vector perpendicular to the graphene plane, $a_0 = a/\sqrt{3} \simeq 0.142$ nm is the distance between neighboring A and B sites on graphene and two graphene layers are separated by a distance $d_0 = 0.335$ nm. The parameter $V_{0pp\pi} \simeq -2.7$ eV is the intralayer transfer integral between nearest-neighbor atoms and $V_{0pp\sigma} \simeq 0.48$ eV is the transfer integral between atoms located at neighboring layers of graphite. r_0 is the decay length of the transfer integral, estimated to be $0.184a$, which lowers the next-nearest interlayer coupling to $0.1V_{pp\pi}^0$ [102, 101]. Defining the transfer integral $T(\mathbf{r})$ between the atomic sites, one can compute the in-plane Fourier transform $t(\mathbf{q})$ and specify the interlayer Hamiltonian. The interlayer matrix element is given by Eq. (1.57).

As an example, when we start from $\mathbf{k} = \mathbf{K}_+$ (K-point) of layer 1, the matrix $\mathcal{H}$ express the coupling of this state to $\tilde{\mathbf{k}} = \mathbf{K}_+ + m_1 \mathbf{R}_1^{*(M)} + m_2 \mathbf{R}_2^{*(M)}$ in layer 2 with the amplitude $t(\mathbf{K}_+ + m_1 \mathbf{a}_1^* + m_2 \mathbf{a}_2^*)$. Figure 1.10, right panel, illustrates three important scattering process with

$$(m_1, m_2) = (0, 0), \qquad (m_1, m_2) = (1, 0), \qquad (m_1, m_2) = (0, 1),$$

where the red point shows the electron at $\mathbf{K}_+$ of layer 1 and three blue points show the wave numbers of coupled electrons on layer 2,

$$\tilde{\mathbf{k}}_1 = \mathbf{K}_+, \qquad \tilde{\mathbf{k}}_2 = \mathbf{K}_+ + \mathbf{R}_1^{*(M)}, \qquad \tilde{\mathbf{k}}_3 = \mathbf{K}_+ + \mathbf{R}_2^{*(M)}.$$

Since $T(\mathbf{R})$ exponentially decays in $R \gtrsim r_0$, the Fourier transform $t(\mathbf{q})$ decays in $q \gtrsim 1/r_0$ so only a few sets of (m_1, m_2) satisfying $|\mathbf{K}_+ + m_1 \mathbf{a}_1^* + m_2 \mathbf{a}_2^*| \lesssim 1/r_0$ have an important role in interlayer coupling. Shifting the initial vector $\mathbf{k}$ from the $\mathbf{K}$ point modifies the

matrix elements, but we neglect such a dependence, assuming $\mathbf{k}$ is close to the Dirac point. As a result, the interlayer Hamiltonian near the $\mathbf{K}_+$ valley is expressed as

$$
\mathscr{H} = \begin{pmatrix} \mathscr{H}_{\tilde{A}A} & \mathscr{H}_{\tilde{A}B} \\ \mathscr{H}_{\tilde{B}A} & \mathscr{H}_{\tilde{B}B} \end{pmatrix} = \begin{pmatrix} t_{\tilde{A}A}(\mathbf{K}_+) & t_{\tilde{A}B}(\mathbf{K}_+) \\ t_{\tilde{B}A}(\mathbf{K}_+) & t_{\tilde{B}B}(\mathbf{K}_+) \end{pmatrix}
$$

$$
+ \begin{pmatrix} t_{\tilde{A}A}(\mathbf{K}_+ + \mathbf{a}_1^*) & t_{\tilde{A}B}(\mathbf{K}_+ + \mathbf{a}_1^*)e^{-\frac{2\pi}{3}} \\ t_{\tilde{B}A}(\mathbf{K}_+ + \mathbf{a}_1^*)e^{\frac{2\pi}{3}} & t_{\tilde{B}B}(\mathbf{K}_+ + \mathbf{a}_1^*) \end{pmatrix}
$$

$$
+ \begin{pmatrix} t_{\tilde{A}A}(\mathbf{K}_+ + \mathbf{a}_2^*) & t_{\tilde{A}B}(\mathbf{K}_+ + \mathbf{a}_2^*)e^{-\frac{2\pi}{3}} \\ t_{\tilde{B}A}(\mathbf{K}_+ + \mathbf{a}_2^*)e^{\frac{2\pi}{3}} & t_{\tilde{B}B}(\mathbf{K}_+ + \mathbf{a}_2^*) \end{pmatrix}, \tag{1.65}
$$

the coupling amplitudes are given by $t(K) \approx 110$ meV, where $K = |\mathbf{K}| = 4\pi/(3a)$.
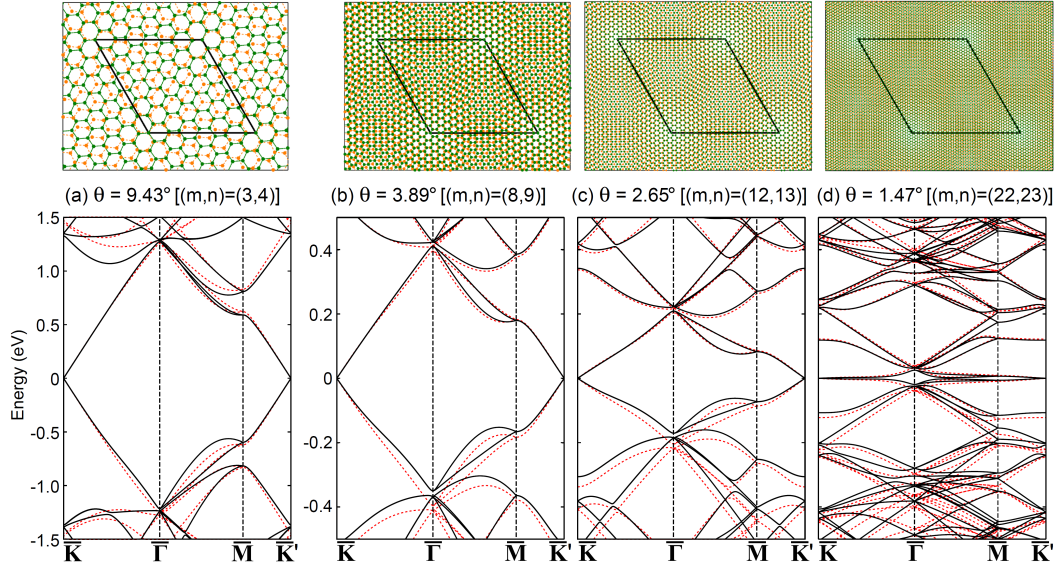
Figure 1.13
Atomic structures (top) and band structures (bottom) of TBGs with (a) $\phi = 9.43°$, (b) 3.89°, (c) 2.65°, and (d) 1.47°, calculated by the tight-binding model (solid black lines) and the eective continuum model (dashed red lines). The Dirac point energy is set to zero. This figure is taken from Ref. [68].

The total Hamiltonian is written in the basis of $\{A, B, \tilde{A}, \tilde{B}\}$ as

$$
H_{eff}^{(\xi)} = \begin{pmatrix} H_1 & \mathscr{H}^\dagger \\ \mathscr{H} & H_2 \end{pmatrix} \tag{1.66}
$$

26

where H_1 and H_2 are the intralayer Hamiltonian of layer 1 and 2, respectively, dened by the massless Dirac Hamiltonian [2]

$$H_l(\mathbf{k}) \approx -\hbar v \left[R_z(\pm\phi/2)\left(\mathbf{k} - \mathbf{K}_\xi^{(l)}\right)\right] \cdot (\xi\sigma_x, \sigma_y), \tag{1.67}$$

with Pauli matrices σ_x and σ_y, and the graphenes band velocity v.

We can use the effective continuum model to obtain the band structure of TBG at any small twist angle regardless of the commensurability of the exact lattice structure. By increasing the rotation angle the moiré period becomes in the range of the atomic scale and the long-range eective theory is not applicable anymore. But still, we can obtain the quasi band structure using the original expression of the interlayer matrix, Eq. (1.51), and the lowest-order approximation that neglects higher-order coupling processes [45]. Figure 1.13 shows the band structure of TBG at four different rotation angle, calculated using the effective continuum model.

1.5   BCS theory of superconductivity

In 1956 Cooper showed that near the Fermi level any arbitrarily small attractive interaction can bond two electrons together and form a stable state called a Cooper pair. Fröhlich and, independently, Bardeen suggested this attractive force can be mediated of phonons. These two observations is the basis of the BCS theory of superconductivity. Here we want to study this theory using mean-field approximation.

1.5.1   Cooper pair

The Schrödinger equation for two electrons that interact with each other via a potential $V(\mathbf{r}_1 - \mathbf{r}_2)$ is:

$$\left[-\frac{\hbar^2\nabla_{\mathbf{r}_1}^2}{2m} - \frac{\hbar^2\nabla_{\mathbf{r}_2}^2}{2m} + V(\mathbf{r}_1 - \mathbf{r}_2) \right]\Psi(\mathbf{r}_1, \mathbf{r}_2) = E\Psi(\mathbf{r}_1, \mathbf{r}_2).$$

We change the variables to the relative displacement and center of mass position. Therefore:

$$\left[-\frac{\hbar^2\nabla_{\mathbf{R}}^2}{2m^*} - \frac{\hbar^2\nabla_{\mathbf{r}}^2}{2\mu} + V(\mathbf{r}) \right]\Psi(\mathbf{r}, \mathbf{R}) = E\Psi(\mathbf{r}, \mathbf{R}).$$

Where $m^* = 2m$ and $\mu = m/2$. Since the potential is independent of $\mathbf{R}$, we expect a wave function as, $\Psi(\mathbf{r}, \mathbf{R}) = \psi(\mathbf{r})e^{i\mathbf{K}\cdot\mathbf{R}}$. Therefore the equation becomes:

$$\left[-\frac{\hbar^2\nabla_{\mathbf{r}}^2}{2\mu} + V(\mathbf{r}) \right]\psi(\mathbf{r}) = \tilde{E}\psi(\mathbf{r}),$$

where we defined $\tilde{E} = E - \frac{\hbar^2\mathbf{K}^2}{2m^*}$. The system should have the minimum value of energy, therefore the momentum of the center of mass should be zero. In other words, the two

electrons should have opposite momenta. Taking the Fourier transform $\left(\psi(\mathbf{k}) = \int d^3r\ \psi(\mathbf{r})e^{-i\mathbf{k}\cdot\mathbf{r}}\right)$ of the above equation gives:

$$\frac{\hbar^2 k^2}{2\mu}\psi(\mathbf{k}) + \int d^3r\ V(\mathbf{r})\psi(\mathbf{r})e^{-i\mathbf{k}\cdot\mathbf{r}} = E\psi(\mathbf{k})$$

$$\int \frac{d^3q}{(2\pi)^3}V(\mathbf{q})\int d^3r\ \psi(\mathbf{r})e^{-i(\mathbf{k}-\mathbf{q})\cdot\mathbf{r}} = (E - \frac{\hbar^2 k^2}{m})\psi(\mathbf{k})$$

$$\int \frac{d^3k'}{(2\pi)^3}V(\mathbf{k}-\mathbf{k}')\psi(\mathbf{k}') = (E - 2\epsilon_{\mathbf{k}})\psi(\mathbf{k}). \qquad (1.68)$$

In the last line, we used the definition of free electron energy $\left(\epsilon_{\mathbf{k}} = \frac{\hbar^2 k^2}{2m}\right)$ and changed variables to $\mathbf{q} = \mathbf{k} - \mathbf{k}'$. The energy of the bound state of two electrons is smaller than the energy of two electrons in a free electron gas. A modified wave-function is defined as follows:

$$\Delta(\mathbf{k}) = (E - 2\epsilon_{\mathbf{k}})\psi(\mathbf{k}),$$

and substitution in equation (1.68) gives:

$$\Delta(\mathbf{k}) = -\int \frac{d^3k'}{(2\pi)^3}\frac{V(\mathbf{k}-\mathbf{k}')}{(2\epsilon_{\mathbf{k}}-E)}\Delta(\mathbf{k}').$$

Suppose the electron-phonon interaction provides an attractive potential $V(\mathbf{k}-\mathbf{k}') = -V_0$ for electrons in the energy range of $(\epsilon_{\mathbf{k}'} - \epsilon_F, \epsilon_{\mathbf{k}} - \epsilon_F < \hbar\omega_D)$ and zero potential outside of this range. The density of states can be approximated by its value at the Fermi energy. Thus, for $\Delta(\mathbf{k}) = \Delta$ independent of the direction, we have:

$$\Delta = V_0\rho(\epsilon_F)\Delta \int_{\epsilon_F}^{\epsilon_F + \hbar\omega_D} \frac{d\epsilon}{2\epsilon - E}$$

or, if $\Delta \neq 0$,

$$\frac{2}{V_0\rho(\epsilon_F)} = \ln\left(\frac{2\epsilon_F - E + 2\hbar\omega_D}{2\epsilon_F - E}\right).$$

Using the approximation $2\epsilon_F - E + 2\hbar\omega_D \simeq 2\hbar\omega_D$ we obtain:

$$E_b \equiv 2\epsilon_F - E = 2\hbar\omega_D e^{-\frac{2}{V_0\rho(\epsilon_F)}}.$$

This shows for any small value of the attractive potential, the bound state energy is lower than that of the free electron gas and so it is stable. This bound state is called a Cooper pair.

28

1.5.2 BCS wave-function

The effective many-body Hamiltonian that describes superconductivity is:

$$H = \sum_{\mathbf{k}\sigma} \xi_{\mathbf{k}} c^{\dagger}_{\mathbf{k}\sigma} c_{\mathbf{k}\sigma} + \frac{1}{N} \sum_{\mathbf{k}\mathbf{k}'} V_{\mathbf{k}\mathbf{k}'} c^{\dagger}_{\mathbf{k}\uparrow} c^{\dagger}_{-\mathbf{k}\downarrow} c_{-\mathbf{k}'\downarrow} c_{\mathbf{k}'\uparrow}$$

Here $c^{\dagger}_{\mathbf{k}\sigma}$ and $c_{\mathbf{k}\sigma}$ are electron creation and annihilation operators, respectively, and $\xi_{\mathbf{k}} = \epsilon_{\mathbf{k}} - \mu$. The second term describes the creation and annihilation of Cooper pairs. We use mean-field theory to simplify the second term of Hamiltonian:

$$c^{\dagger}_{\mathbf{k}\uparrow} c^{\dagger}_{-\mathbf{k}\downarrow} c_{-\mathbf{k}'\downarrow} c_{\mathbf{k}'\uparrow} \approx \langle c^{\dagger}_{\mathbf{k}\uparrow} c^{\dagger}_{-\mathbf{k}\downarrow} \rangle c_{-\mathbf{k}'\downarrow} c_{\mathbf{k}'\uparrow} + c^{\dagger}_{\mathbf{k}\uparrow} c^{\dagger}_{-\mathbf{k}\downarrow} \langle c_{-\mathbf{k}'\downarrow} c_{\mathbf{k}'\uparrow} \rangle - \langle c^{\dagger}_{\mathbf{k}\uparrow} c^{\dagger}_{-\mathbf{k}\downarrow} \rangle \langle c_{-\mathbf{k}'\downarrow} c_{\mathbf{k}'\uparrow} \rangle.$$

The gap function is defined by $\Delta_{\mathbf{k}} = -\frac{1}{N} \sum_{\mathbf{k}'} V_{\mathbf{k}\mathbf{k}'} \langle c_{-\mathbf{k}'\downarrow} c_{\mathbf{k}'\uparrow} \rangle$ and the Hamiltonian becomes:

$$H = \sum_{\mathbf{k}\sigma} \xi_{\mathbf{k}} c^{\dagger}_{\mathbf{k}\sigma} c_{\mathbf{k}\sigma} - \sum_{\mathbf{k}} \left(\Delta_{\mathbf{k}} c^{\dagger}_{\mathbf{k}\uparrow} c^{\dagger}_{-\mathbf{k}\downarrow} + \Delta^{*}_{\mathbf{k}} c_{-\mathbf{k}\downarrow} c_{\mathbf{k}\uparrow} \right) + \sum_{\mathbf{k}} \Delta_{\mathbf{k}} \langle c^{\dagger}_{\mathbf{k}\uparrow} c^{\dagger}_{-\mathbf{k}\downarrow} \rangle.$$

In order to bring this Hamiltonian into the desired form, we introduce the Nambu spinor

$$c_{\mathbf{k}} = \begin{pmatrix} c_{\mathbf{k}\uparrow} \\ c^{\dagger}_{-\mathbf{k}\downarrow} \end{pmatrix} \tag{1.69}$$

which allows us to express H^{MF}_{BCS} in a form similar to the usual free fermion problem:

$$H = \sum_{\mathbf{k}} c^{\dagger}_{\mathbf{k}} h_{\mathbf{k}} c_{\mathbf{k}} + \sum_{\mathbf{k}} \left(\xi_{\mathbf{k}} + \Delta_{\mathbf{k}} \langle c^{\dagger}_{\mathbf{k}\uparrow} c^{\dagger}_{-\mathbf{k}\downarrow} \rangle \right), \tag{1.70}$$

with the 2×2-matrix

$$h_{\mathbf{k}} = \begin{pmatrix} \xi_{\mathbf{k}} & -\Delta_{\mathbf{k}} \\ -\Delta^{*}_{\mathbf{k}} & -\xi_{\mathbf{k}} \end{pmatrix}. \tag{1.71}$$

The eigenvalues of $h_{\mathbf{k}}$ are determined by $(E - \xi_{\mathbf{k}})(E + \xi_{\mathbf{k}}) - |\Delta_{\mathbf{k}}|^2 = 0$, which yields

$$E_{\mathbf{k}\pm} = \pm E_{\mathbf{k}} \tag{1.72}$$

with

$$E_{\mathbf{k}} = \sqrt{\xi^2_{\mathbf{k}} + |\Delta_{\mathbf{k}}|^2} > 0. \tag{1.73}$$

$h_{\mathbf{k}}$ is diagonalized by the unitary transformation $U_{\mathbf{k}}$. The columns of $U_{\mathbf{k}}$ are the eigenvectors $u^{(i)}_{\mathbf{k}}$ of $h_{\mathbf{k}}$. Interestingly there is some nontrivial structure in the matrix $h_{\mathbf{k}}$ that is

worth exploring as it can be very helpful for more complex systems such as multi-band superconductors or inhomogeneous systems. It holds with $\gamma = i\sigma_y$ that

$$\gamma h_{\mathbf{k}}^* \gamma^{-1} = -h_{\mathbf{k}} \tag{1.74}$$

Suppose one eigenvector of $h_{\mathbf{k}}$ is $\mathbf{u}_{\mathbf{k}}^{(1)} = (u_{\mathbf{k}}^*, -v_{\mathbf{k}}^*)^T$ corresponding to the eigenvalue $+E_{\mathbf{k}}$, i.e. $h_{\mathbf{k}}\mathbf{u}_{\mathbf{k}}^{(1)} = +E_{\mathbf{k}}\mathbf{u}_{\mathbf{k}}^{(1)}$. We can now construct the other vector

$$\mathbf{u}_{\mathbf{k}}^{(2)} = -\gamma \mathbf{u}_{\mathbf{k}}^{(1)*} = (v_{\mathbf{k}}, u_{\mathbf{k}})^T \tag{1.75}$$

which obeys

$$\gamma \mathbf{u}_{\mathbf{k}}^{(2)*} = -\gamma^2 \mathbf{u}_{\mathbf{k}}^{(1)} = \mathbf{u}_{\mathbf{k}}^{(1)} \tag{1.76}$$

$\mathbf{u}_{\mathbf{k}}^{(2)}$ is also an eigenvector but with eigenvalue $-E_{\mathbf{k}}$. To show that this is the case, we take the complex conjugate of the second eigenvalue equation $h_{\mathbf{k}}^* \mathbf{u}_{\mathbf{k}}^{(2)*} = -E_{\mathbf{k}}\mathbf{u}_{\mathbf{k}}^{(2)*}$ and write it as $\gamma h_{\mathbf{k}}^* \gamma^{-1} \gamma \mathbf{u}_{\mathbf{k}}^{(2)*} = -\gamma E_{\mathbf{k}}\mathbf{u}_{\mathbf{k}}^{(2)*}$, which yields $-h_{\mathbf{k}}\gamma \mathbf{u}_{\mathbf{k}}^{(2)*} = -\gamma E_{\mathbf{k}}\mathbf{u}_{\mathbf{k}}^{(2)*}$, and leads to the rst eigenvalue equation $h_{\mathbf{k}}\mathbf{u}_{\mathbf{k}}^{(1)} = E_{\mathbf{k}}\mathbf{u}_{\mathbf{k}}^{(1)}$, proving our assertion. Thus, the eigenvalues of the mean eld Hamiltonian occur in pairs of opposite signs and with eigenvalues related by the unimodular transformation γ. The unitary transformation that diagonalizes the above 2×2 matrix is

$$U_{\mathbf{k}} = \begin{pmatrix} u_{\mathbf{k}}^* & v_{\mathbf{k}} \\ -v_{\mathbf{k}}^* & u_{\mathbf{k}} \end{pmatrix} \tag{1.77}$$

and it follows that $U_{\mathbf{k}}^{-1} h_{\mathbf{k}} U_{\mathbf{k}} = \mathrm{diag}(E_{\mathbf{k}}, -E_{\mathbf{k}})$. It is straightforward to determine $u_{\mathbf{k}}$ and $v_{\mathbf{k}}$ from the eigenvalue equations;

$$v_{\mathbf{k}} = \frac{\Delta_{\mathbf{k}}}{E_{\mathbf{k}} + \xi_{\mathbf{k}}} u_{\mathbf{k}}. \tag{1.78}$$

Unitarity, i.e., the normalization of the eigenvectors, implies $|u_{\mathbf{k}}|^2 + |v_{\mathbf{k}}|^2 = 1$, and it follows that

$$|v_{\mathbf{k}}|^2 = \frac{1}{1 + \left|\frac{u_{\mathbf{k}}}{v_{\mathbf{k}}}\right|^2} = \frac{1}{1 + \left|\frac{E_{\mathbf{k}}+\xi_{\mathbf{k}}}{\Delta_{\mathbf{k}}}\right|^2}. \tag{1.79}$$

By using Eq. (1.73), this leads to:

$$\begin{aligned} |v_{\mathbf{k}}|^2 &= \frac{1}{2}\left(1 - \frac{\xi_{\mathbf{k}}}{E_{\mathbf{k}}}\right), \\ |u_{\mathbf{k}}|^2 &= 1 - v_{\mathbf{k}}^2 = \frac{1}{2}\left(1 + \frac{\xi_{\mathbf{k}}}{E_{\mathbf{k}}}\right). \end{aligned} \tag{1.80}$$

as well as $u_{\mathbf{k}} v_{\mathbf{k}}^* = \frac{\Delta_{\mathbf{k}}}{2E_{\mathbf{k}}}$.

The unitary transformation transforms the Nambu spinor $c_{\mathbf{k}}$ according to $a_{\mathbf{k}} = U_{\mathbf{k}}^{-1} c_{\mathbf{k}}$ with $a_{\mathbf{k}} = \left(a_{\mathbf{k}\uparrow}, a_{-\mathbf{k}\downarrow}^\dagger \right)^T$ and it follows that

$$
\begin{aligned}
\sum_{\mathbf{k}} c_{\mathbf{k}}^\dagger h_{\mathbf{k}} c_{\mathbf{k}} &= \sum_{\mathbf{k}} c_{\mathbf{k}}^\dagger U_{\mathbf{k}} \begin{pmatrix} E_{\mathbf{k}} & 0 \\ 0 & -E_{\mathbf{k}} \end{pmatrix} U_{\mathbf{k}}^{-1} c_{\mathbf{k}} \\
&= \sum_{\mathbf{k}} a_{\mathbf{k}}^\dagger \begin{pmatrix} E_{\mathbf{k}} & 0 \\ 0 & -E_{\mathbf{k}} \end{pmatrix} a_{\mathbf{k}} \\
&= \sum_{\mathbf{k}} E_{\mathbf{k}} \left(a_{\mathbf{k}\uparrow}^\dagger a_{\mathbf{k}\uparrow} - a_{-\mathbf{k}\downarrow} a_{-\mathbf{k}\downarrow}^\dagger \right) \\
&= \sum_{\mathbf{k}} E_{\mathbf{k}} \left(a_{\mathbf{k}\uparrow}^\dagger a_{\mathbf{k}\uparrow} + a_{-\mathbf{k}\downarrow}^\dagger a_{-\mathbf{k}\downarrow} - 1 \right) \\
&= \sum_{\mathbf{k}\sigma} E_{\mathbf{k}} a_{\mathbf{k}\sigma}^\dagger a_{\mathbf{k}\sigma} - \sum_{\mathbf{k}} E_{\mathbf{k}}
\end{aligned}
\tag{1.81}
$$

The mean eld Hamiltonian is then expressed as:

$$
H = \sum_{\mathbf{k},\sigma} E_{\mathbf{k}} a_{\mathbf{k}\sigma}^\dagger a_{\mathbf{k}\sigma} + \sum_{\mathbf{k}} \left(\xi_{\mathbf{k}} + \Delta_{\mathbf{k}} \langle c_{\mathbf{k}\uparrow}^\dagger c_{-\mathbf{k}\downarrow}^\dagger \rangle - \sqrt{\xi_{\mathbf{k}}^2 + |\Delta_{\mathbf{k}}|^2} \right).
\tag{1.82}
$$

The second term on the right-hand side of the equation (1.82) is the ground state energy. Now it is clear why we called $\Delta_{\mathbf{k}}$ the gap function: The minimum energy we need to excite quasi-particles, which are described by the operators $a_{\mathbf{k}\sigma}^\dagger$ and are usually called Bogoliubons, is more than $|\Delta_{\mathbf{k}}|$. At the Fermi level, where $\xi_{\mathbf{k}} = 0$, the gap size is equal to $|\Delta_{\mathbf{k}}|$.

A Bogoliubon is a quasi-particle that made of a superposition of an electron and a hole, so the creation of a Bogoliubon amounts to creating an electron in a state above the Fermi level and a hole of opposite momentum and spin below the Fermi level. Therefore, the vacuum of Bogoliubons is the BCS ground state wave-function:

$$
a_{\mathbf{k}\sigma} |\Psi_{BCS}\rangle = 0 \text{ for all } \mathbf{k}, \sigma.
$$

Now we want to express this ground state in terms of the original electron operators. The following equation is our starting point

$$
a_{\mathbf{k}\uparrow} |\Psi_{BCS}\rangle = 0 \quad \rightarrow \quad u_{\mathbf{k}} c_{\mathbf{k}\uparrow} |\Psi_{BCS}\rangle = v_{\mathbf{k}} c_{-\mathbf{k}\downarrow}^\dagger |\Psi_{BCS}\rangle.
\tag{1.83}
$$

Where we used $a_{\mathbf{k}} = U_{\mathbf{k}}^{(-1)} c_{\mathbf{k}}$, which explicitly is

$$
a_{\mathbf{k}\uparrow} = u_{\mathbf{k}} c_{\mathbf{k}\uparrow} - v_{\mathbf{k}} c_{-\mathbf{k}\downarrow}^\dagger, \qquad a_{-\mathbf{k}\downarrow}^\dagger = v_{\mathbf{k}}^* c_{\mathbf{k}\uparrow} + u_{\mathbf{k}}^* c_{-\mathbf{k}\downarrow}^\dagger
\tag{1.84}
$$

31

and is sometimes called the Bogoliobov transformation.

We suppose an arbitrary combination of Cooper pairs as the BCS wave-function:

$$|\Psi_{BCS}\rangle = \mathcal{N} \prod_{\mathbf{q}} e^{\alpha_{\mathbf{q}} c^{\dagger}_{\mathbf{q}\uparrow} c^{\dagger}_{-\mathbf{q}\downarrow}} |0\rangle$$

where $\mathcal{N}$ is a normalization constant and $\alpha_{\mathbf{k}}$ is a function that is determined in the following. When $c_{\mathbf{k}\uparrow}$ acts on the above wave-function, it commutes with all terms inside the product, except the one for which $\mathbf{q} = \mathbf{k}$. In the following, for simplicity we define $\theta_{\mathbf{k}} = \alpha_{\mathbf{k}} c^{\dagger}_{\mathbf{k}\uparrow} c^{\dagger}_{-\mathbf{k}\downarrow}$ and calculate how the $c_{\mathbf{k}\uparrow}$ acts on the $e^{\theta_{\mathbf{k}}} |0\rangle$,

$$c_{\mathbf{k}\uparrow} e^{\alpha_{\mathbf{k}} c^{\dagger}_{\mathbf{k}\uparrow} c^{\dagger}_{-\mathbf{k}\downarrow}} |0\rangle = c_{\mathbf{k}\uparrow} e^{\theta_{\mathbf{k}}} |0\rangle = \sum_{n=1}^{\infty} \frac{c_{\mathbf{k}\uparrow} \theta_{\mathbf{k}}^{n}}{n!} |0\rangle.$$

Using the relation, $[A, BC] = \{A, B\}C - B\{A, C\}$ we have the commutation relation

$$\left[c_{\mathbf{k}\uparrow}, \theta_{\mathbf{k}} \right] = \alpha_{\mathbf{k}} \{ c_{\mathbf{k}\uparrow}, c^{\dagger}_{\mathbf{k}\uparrow} \} c^{\dagger}_{-\mathbf{k}\downarrow} = \alpha_{\mathbf{k}} c^{\dagger}_{-\mathbf{k}\downarrow}.$$

Hence, since $c_{\mathbf{k}\uparrow}|0\rangle = 0$, it follows that:

$$c_{\mathbf{k}\uparrow} \theta_{\mathbf{k}} |0\rangle = \alpha_{\mathbf{k}} c^{\dagger}_{-\mathbf{k}\downarrow} |0\rangle,$$
$$c_{\mathbf{k}\uparrow} \theta_{\mathbf{k}}^{2} |0\rangle = \left(\left[c_{\mathbf{k}\uparrow} \theta_{\mathbf{k}}, \theta_{\mathbf{k}} \right] + \theta_{\mathbf{k}} c_{\mathbf{k}\uparrow} \theta_{\mathbf{k}} \right) |0\rangle$$
$$= \theta_{\mathbf{k}} \left(\left[c_{\mathbf{k}\uparrow}, \theta_{\mathbf{k}} \right] + c_{\mathbf{k}\uparrow} \theta_{\mathbf{k}} \right) |0\rangle = 2 \theta_{\mathbf{k}} \alpha_{\mathbf{k}} c^{\dagger}_{-\mathbf{k}\downarrow} |0\rangle,$$

(1.85)

and, in general,

$$c_{\mathbf{k}\uparrow} \theta_{\mathbf{k}}^{n} |0\rangle = n \theta_{\mathbf{k}}^{n-1} \alpha_{\mathbf{k}} c^{\dagger}_{-\mathbf{k}\downarrow} |0\rangle. \qquad (1.86)$$

Therefore:

$$c_{\mathbf{k}\uparrow} e^{\alpha_{\mathbf{k}} c^{\dagger}_{\mathbf{k}\uparrow} c^{\dagger}_{-\mathbf{k}\downarrow}} |0\rangle = \alpha_{\mathbf{k}} \sum_{n=1}^{\infty} \frac{\theta_{\mathbf{k}}^{n-1}}{(n-1)!} c^{\dagger}_{-\mathbf{k}\downarrow} |0\rangle.$$

Now, since $\left[\theta_{\mathbf{k}}, c^{\dagger}_{-\mathbf{k}\downarrow} \right] = \alpha_{\mathbf{k}} \left[c^{\dagger}_{\mathbf{k}\uparrow} c^{\dagger}_{-\mathbf{k}\downarrow}, c^{\dagger}_{-\mathbf{k}\downarrow} \right] = 0$ we obtain:

$$c_{\mathbf{k}\uparrow} \left(e^{\alpha_{\mathbf{k}} c^{\dagger}_{\mathbf{k}\uparrow} c^{\dagger}_{-\mathbf{k}\downarrow}} |0\rangle \right) = \alpha_{\mathbf{k}} c^{\dagger}_{-\mathbf{k}\downarrow} \sum_{n'=0}^{\infty} \frac{\theta_{\mathbf{k}}^{n'}}{n'!} |0\rangle = \alpha_{\mathbf{k}} c^{\dagger}_{-\mathbf{k}\downarrow} \left(e^{\alpha_{\mathbf{k}} c^{\dagger}_{\mathbf{k}\uparrow} c^{\dagger}_{-\mathbf{k}\downarrow}} |0\rangle \right).$$

Substituting in equation (1.83) gives:

$$u_{\mathbf{k}} c_{\mathbf{k}\uparrow} |\Psi_{BCS}\rangle = u_{\mathbf{k}} \alpha_{\mathbf{k}} c^{\dagger}_{-\mathbf{k}\downarrow} |\Psi_{BCS}\rangle = v_{\mathbf{k}} c^{\dagger}_{-\mathbf{k}\downarrow} |\Psi_{BCS}\rangle,$$

therefore, $\alpha_{\mathbf{k}} = \frac{v_{\mathbf{k}}}{u_{\mathbf{k}}}$.

Hence, the BCS wave-function is:

$$|\Psi_{BCS}\rangle = \mathcal{N} \prod_{\mathbf{k}} e^{\frac{v_{\mathbf{k}}}{u_{\mathbf{k}}} c^{\dagger}_{\mathbf{k}\uparrow} c^{\dagger}_{-\mathbf{k}\downarrow}} |0\rangle = \mathcal{N} \prod_{\mathbf{k}} \left(1 + \frac{v_{\mathbf{k}}}{u_{\mathbf{k}}} c^{\dagger}_{\mathbf{k}\uparrow} c^{\dagger}_{-\mathbf{k}\downarrow} \right) |0\rangle.$$

Using the Pauli's principle we know, $\left(c_{k\uparrow}^{\dagger} c_{-k\downarrow}^{\dagger}\right)^{n} = 0$ for $n > 1$. After normalization, BCS wave-function is given by:

$$|\Psi_{BCS}\rangle = \prod_{k} \left(u_{k} + v_{k} c_{k\uparrow}^{\dagger} c_{-k\downarrow}^{\dagger}\right) |0\rangle$$

1.5.3 The gap equation

Now we want to determine the gap function which was defined by the equation, $\Delta_{k} = -\frac{1}{N} \sum_{k'} V_{kk'} \langle c_{-k'\downarrow} c_{k'\uparrow}\rangle$. Using the Bogoliobov transformation (Eq. 1.84):

$$\Delta_{k} = -\frac{1}{N} \sum_{k'} V_{kk'} \left\langle \left(u_{k'}^{*} a_{-k'\downarrow} - v_{k'} a_{k'\uparrow}^{\dagger}\right)\left(u_{k'}^{*} a_{k'\uparrow} + v_{k'} a_{-k'\downarrow}^{\dagger}\right)\right\rangle,$$

$$\Delta_{k} = -\frac{1}{N} \sum_{k'} V_{kk'} u_{k'}^{*} v_{k'} \left(\langle a_{-k'\downarrow} a_{-k'\downarrow}^{\dagger}\rangle - \langle a_{k'\uparrow}^{\dagger} a_{k'\uparrow}\rangle\right).$$

The Bogoliubons are fermions and follow the Fermi-Dirac distribution function. Therefore:

$$\langle a_{-k'\downarrow} a_{-k'\downarrow}^{\dagger}\rangle - \langle a_{k'\uparrow}^{\dagger} a_{k'\uparrow}\rangle = 1 - \frac{1}{e^{\beta E_{k'}} + 1} - \frac{1}{e^{\beta E_{k'}} + 1} = \tanh\left(\frac{E_{k'}}{2k_{B}T}\right).$$

Using equations (1.78) and (1.80), we have:

$$u_{k'}^{*} v_{k'} = |u_{k'}|^{2} \frac{v_{k'}}{u_{k'}} = \frac{\Delta_{k'}}{2\sqrt{\xi_{k'}^{2} + |\Delta_{k'}|^{2}}},$$

and, for the gap function,

$$\Delta_{k} = -\frac{1}{N} \sum_{k'} \frac{V_{kk'} \Delta_{k'}}{2E_{k'}} \tanh\left(\frac{E_{k'}}{2k_{B}T}\right).$$

Now we can find the values of the attractive potential and also the temperature that led to the gap function and therefore, the BCS ground state wave function. We need to define a form for the potential so we suppose for electrons near the Fermi level, inside a shell of thickness $\hbar\omega_{D}$ the potential has a constant value ($V_{kk'} = -V_{0}$) and outside this shell it is zero. Since the potential is **k** independent, we expect that the gap function does not depend on **k**. Because of its spherical symmetry this type of gap function is called an s-wave gap. So, we have:

$$1 = \frac{V_{0}}{N} \sum_{k<k_{D}} \frac{1}{2E_{k}} \tanh\left(\frac{E_{k}}{2k_{B}T}\right).$$

Using the density of states we replace the summation with an integral:

$$1 = V_{0} \int_{-\hbar\omega_{D}}^{\hbar\omega_{D}} \frac{\rho(\epsilon)d\epsilon}{2\sqrt{\epsilon^{2} + \Delta^{2}}} \tanh\left(\frac{\sqrt{\epsilon^{2} + \Delta^{2}}}{2k_{B}T}\right),$$

33

the density of states doesn't change very much in the integral domain, so we use its value at Fermi level as an approximation and we have:

$$1 = V_0 \rho(\epsilon_F) \int_0^{\hbar \omega_D} \frac{d\epsilon}{\sqrt{\epsilon^2 + \Delta^2}} \tanh\left(\frac{\sqrt{\epsilon^2 + \Delta^2}}{2 k_B T}\right). \tag{1.87}$$

Using the above equation we can calculate the gap function for an arbitrary temperature. For example, at $T = 0$ we have $\tanh(x \to \infty) \to 1$ and therefore:

$$1 = V_0 \rho(\epsilon_F) \int_0^{\hbar \omega_D} \frac{d\epsilon}{\sqrt{\epsilon^2 + \Delta_0^2}},$$

where $\Delta_0 \equiv \Delta(T = 0)$. After solving the integral:

$$\frac{1}{V_0 \rho(\epsilon_F)} = \sinh^{-1}\left(\frac{\hbar \omega_D}{\Delta_0}\right) = \ln\left(\frac{2 \hbar \omega_D}{\Delta_0}\right),$$

in the last step we used $\sinh^{-1}(x) = \ln(x + \sqrt{x^2 + 1})$ and since Δ_0 is much smaller than $\hbar \omega_D$ we suppose $\sqrt{x^2 + 1} \simeq x$. So, the gap function is:

$$\Delta_0 = 2 \hbar \omega_D e^{-\frac{1}{V_0 \rho(\epsilon_F)}}, \tag{1.88}$$

this equation shows for any arbitrary small value of attractive potential, the system has a finite gap and the Fermi liquid is unstable towards the formation of the BCS superconducting state. Now we want to determine the critical temperature in which a nonzero gap appears for the first time. For this end we put $\Delta \to 0$ at equation (1.87) and obtain:

$$T_c = \frac{2 e^{\gamma_E}}{\pi} \frac{\hbar \omega_D}{k_B} e^{-\frac{1}{V_0 \rho(\epsilon_F)}} \tag{1.89}$$

where $\gamma_E \simeq 0.577$ is the Euler constant and we used $\hbar \omega_D >> k_B T_c$. We can combine two equations (1.88), (1.89) to find the universal ratio between the zero-temperature gap and the critical temperature,

$$\frac{\Delta_0}{k_B T_c} \simeq 1.76.$$

This result which is satisfied in many conventional superconductors, is one of the successes of BCS theory.

Chapter 2

Methodology

The study of the metal-insulator transition (or Mott transition) [70] and the discovery of high-temperature superconductors [6] have given rise to much research on strongly correlated electron systems. The nature of electron-electron interactions is often complex and it is not always easy to build microscopic models capable of realistically describing these interactions. However, there are many situations where these microscopic models, such as the Hubbard or t-J model, can be justied. Most of the time it is sufficient to study the model to determine the properties of the system. The analytical solution of the Hamiltonian of these models is limited only to very simple systems. Therefore, we are always turning to numerical methods to solve the Hamiltonian. Among these numerical methods, we can mention the Monte Carlo method, the continuous-time Monte Carlo method, and quantum cluster methods, where the approximations are based on embedding small systems in an infinite lattice. This chapter is devoted to describing the quantum cluster methods used in this document to approximately solve the Hubbard model. However, to introduce these approximate methods, we will first discuss direct methods. Direct numerical methods are mainly based on two bases: exact diagonalization (ED) [17, 14, 44, 53, 54] and Monte Carlo simulations [16, 15, 69, 86, 85, 104]. As the dimension of the Hilbert space increases exponentially with the size of the system, the systems that could be studied with exact diagonalization (ED) are limited to a small number of sites, usually less than twenty. This constraint causes finite-size effects that are more detrimental when considering low energy or long wavelength uctuations. Unlike the exact diagonalization method, Monte Carlo simulations allow larger systems to be processed, but at the cost of statistical error. The calculation of the various quantities must be done by statistical sampling using the Metropolis algorithm. In the Monte-Carlo method, obtaining the spectral weight as a function of frequency must be done by analytical continuation [96, 22]. Quantum cluster methods are similar to direct numerical methods, which consider quantum clusters with a finite number of sites. Despite the restriction of quantum cluster methods to short-range correlation effects, symmetry breaking can appear at the cluster level. Quantum cluster methods are: The variational cluster approximation (VCA) [84, 73, 81], cluster dynamical mean-field theory

(CDMFT) [33, 32, 48, 11] and the dynamical impurity approximation (DIA, or CDIA for its cluster extension). Before describing these methods, we will discuss cluster perturbation theory (CPT) [36, 92, 111, 112] and the exact diagonalization on which it is most often based.

2.1 Cluster perturbation theory

Cluster perturbation theory (CPT) is a numerical technique for computing the approximate Green function of the Hubbard model. It is exact within the limits of weak and strong coupling and provides an approximation for the spectral function of all wave vectors. It directly links theory and experience by making predictions about the spectral weight observable in ARPES. It is also a prerequisite for VCA and CDMFT. This theory begins with a subdivision of the original lattice into several identical clusters as shown in Fig 2.1, where $\mathbf{E}_1$ and $\mathbf{E}_2$ are the basis vectors of the super-lattice.
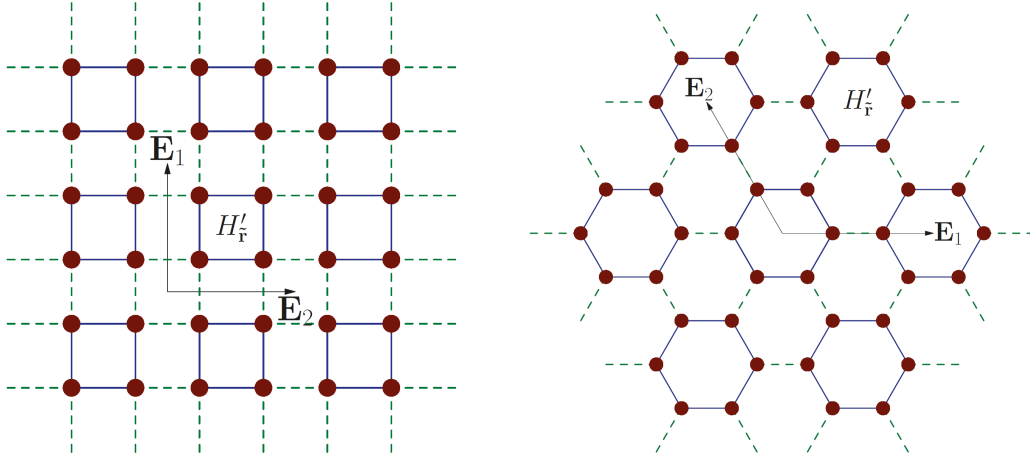
Figure 2.1
Clusters of four and six sites are represented respectively in a square (left) and hexagonal (right) lattice. E_1 and E_2 are the basis vectors of the superlattice defining by the clusters. $H'_{\tilde{\mathbf{r}}}$ is the Hamiltonian of a cluster at position $\tilde{\mathbf{r}}$

The Hamiltonian H of the system is then written in the form:

$$H = H' + V \tag{2.1}$$

In this equation, H' is the total Hamiltonian of clusters, and is dened by:

$$H' = \sum_{\tilde{\mathbf{r}}} H'_{\tilde{\mathbf{r}}} \tag{2.2}$$

36

where $H'_{\tilde{\mathbf{r}}}$ is the Hamiltonian of a cluster at position $\tilde{\mathbf{r}}$. The second term, V of equation (2.1) represents the inter-cluster term of the Hamiltonian. The basic idea of CPT consists of choosing small enough clusters to be able to diagonalize exactly their Hamiltonian and thus obtain the exact Green function for it. The inter-cluster term, V must be treated by perturbation theory. According to the theory of strong coupling perturbations [76, 77, 8, 7, 95], the Green function of the lattice $\mathbf{G}(\omega)$ is expressed as a function of the exact Green function of the cluster $\mathbf{G}'(\omega)$ and the inter cluster term of the Hamiltonian. In matrix form, we can write:

$$\mathbf{G}^{-1}(\omega) = \mathbf{G}'^{-1}(\omega) - \mathbf{V} \tag{2.3}$$

$\mathbf{G}'(\omega)$ is a block diagonal matrix, i.e. it does not include matrix elements between different clusters:

$$\mathbf{G}'_{\tilde{\mathbf{r}},\tilde{\mathbf{r}}'}(\omega) \propto \delta_{\tilde{\mathbf{r}},\tilde{\mathbf{r}}'} \tag{2.4}$$

Translational invariance of the superlattice makes it possible to write the matrix elements of $\mathbf{V}$ and $\mathbf{G}$ as a function of a wave vector $\tilde{\mathbf{q}}$ of the Brillouin zone of the superlattice Γ. For example, for $\mathbf{G}$, we can write:

$$\mathbf{G}_{\tilde{\mathbf{r}},\tilde{\mathbf{r}}'}(\omega) = \sum_{\tilde{\mathbf{q}}} \mathbf{G}_{\tilde{\mathbf{r}},\tilde{\mathbf{r}}'}(\tilde{\mathbf{q}},\omega) e^{i\tilde{\mathbf{q}}\cdot(\tilde{\mathbf{r}}-\tilde{\mathbf{r}}')} \tag{2.5}$$

In this representation, equation (2.3) gives the CPT Green function of the system:

$$\mathbf{G}_{\text{CPT}}^{-1}(\tilde{\mathbf{q}},\omega) = \mathbf{G}'^{-1}(\omega) - \mathbf{V}(\tilde{\mathbf{q}}) \tag{2.6}$$

The matrices in equation (2.6) are $L \times L$ matrices where L is the number of sites in the cluster times the number of bands, in particular spin.

2.1.1 Periodic CPT Green function

The Green function in Eq. (2.6) can be used to calculate average values of one-body operatores. However, a periodic Green function is necessary to evaluate the spectral weight. In what follows, we will show how the periodic CPT Green function could be obtained. The Green function $\mathbf{G}(\tilde{\mathbf{q}},\omega)$ of Eq. (2.6) is written in a mixed representation, i.e., it contains indices in direct space of the clusters and the vector $\tilde{\mathbf{q}} \in \Gamma$. It is preferable to work in the representation of wave vectors. An important point to note is that cluster perturbation theory breaks the translational symmetry of the original lattice. However, at the super-lattice level, this symmetry is obviously preserved. Therefore, the Green function (2.3), must depend on two different wave vectors ($\mathbf{k}$ and $\mathbf{k}'$) of the Brillouin zone. The Fourier transform of the Green function is written as,

$$\mathbf{G}(\mathbf{k},\mathbf{k}',\omega) = \frac{L}{N_r} \sum_{\mathbf{R},\mathbf{R}'} \sum_{\tilde{\mathbf{r}},\tilde{\mathbf{r}}'} \mathbf{G}_{\mathbf{R},\mathbf{R}'}(\omega) e^{-i\mathbf{k}\cdot(\tilde{\mathbf{r}}+\mathbf{R})} e^{i\mathbf{k}'\cdot(\tilde{\mathbf{r}}'+\mathbf{R}')} \tag{2.7}$$

where $\mathbf{R}$ and $\mathbf{R}'$ are the positions of the sites in the cluster, L is the number of sites in the cluster (or super-unit-cell) and N_r is the number of sites in the super-lattice. Using equation (2.5), in (2.7) we have:

$$\mathbf{G}(\mathbf{k},\mathbf{k}',\omega) = \frac{L}{N_r^2}\sum_{\mathbf{R},\mathbf{R}'}\sum_{\tilde{\mathbf{r}},\tilde{\mathbf{r}}'}\sum_{\tilde{\mathbf{q}}}\mathbf{G}_{\mathbf{R},\mathbf{R}'}(\tilde{\mathbf{q}},\omega)e^{i\tilde{\mathbf{q}}\cdot(\tilde{\mathbf{r}}-\tilde{\mathbf{r}}')}e^{-i\mathbf{k}\cdot(\tilde{\mathbf{r}}+\mathbf{R})}e^{i\mathbf{k}'\cdot(\tilde{\mathbf{r}}'+\mathbf{R}')} \tag{2.8}$$

The summation over the cluster sites can be done using:

$$\frac{L^2}{N_r^2}\sum_{\tilde{\mathbf{r}},\tilde{\mathbf{r}}'}e^{i\tilde{\mathbf{r}}\cdot(\tilde{\mathbf{q}}-\mathbf{k})}e^{i\tilde{\mathbf{r}}'\cdot(\tilde{\mathbf{q}}-\mathbf{k}')} = \Delta_\Gamma(\mathbf{k}-\tilde{\mathbf{q}})\Delta_\Gamma(\mathbf{k}'-\tilde{\mathbf{q}}) \tag{2.9}$$

where $\Delta_\Gamma(\mathbf{k})$ is the Laue function:

$$\Delta_\Gamma(\mathbf{k}) = \sum_{\mathbf{K}\in\Gamma^*}\delta_{\mathbf{k}+\mathbf{K}} \tag{2.10}$$

Using this equation, we rewrite the equation (2.8) in the form:

$$\mathbf{G}(\mathbf{k},\mathbf{k}',\omega) = \frac{1}{L}\sum_{\mathbf{R},\mathbf{R}'}\sum_{\tilde{\mathbf{q}}}\mathbf{G}_{\mathbf{R},\mathbf{R}'}(\tilde{\mathbf{q}},\omega)e^{-i\mathbf{k}\cdot\mathbf{R}}e^{i\mathbf{k}'\cdot\mathbf{R}'}\Delta_\Gamma(\mathbf{k}-\tilde{\mathbf{q}})\Delta_\Gamma(\mathbf{k}'-\tilde{\mathbf{q}}) \tag{2.11}$$

We decompose the wave vectors $\mathbf{k}$ and $\mathbf{k}'$ in a unique way by writing (see Fig. 2.2):

$$\mathbf{k} = \mathbf{K}+\tilde{\mathbf{k}} \quad \text{and} \quad \mathbf{k}' = \mathbf{K}'+\tilde{\mathbf{k}}' \tag{2.12}$$

where $\mathbf{K}$, $\mathbf{K}'$ belong both to the reciprocal super-lattice and to BZ_γ, and $\tilde{\mathbf{k}}$, $\tilde{\mathbf{k}}'$ belong to BZ_Γ. Taking into account the translational invariance of the vector $\tilde{\mathbf{q}}$ by an element of the reciprocal superlattice, such as $\mathbf{k}-\tilde{\mathbf{k}}$, we have:

$$\mathbf{G}(\tilde{\mathbf{k}},\tilde{\mathbf{k}}',\omega) = \mathbf{G}(\mathbf{k},\mathbf{k}',\omega) \qquad \text{in the same way} \qquad \mathbf{V}(\mathbf{k}) = \mathbf{V}(\tilde{\mathbf{k}}) \tag{2.13}$$

From equations (2.11), (2.12) and (2.13), we have:

$$\mathbf{G}(\mathbf{k},\mathbf{k}',\omega) = \frac{1}{L}\sum_{\mathbf{R},\mathbf{R}'}\sum_{\tilde{\mathbf{k}}}\mathbf{G}_{\mathbf{R},\mathbf{R}'}(\tilde{\mathbf{k}},\omega)e^{-i\mathbf{k}\cdot\mathbf{R}}e^{i\mathbf{k}'\cdot\mathbf{R}'}\Delta_\Gamma(\tilde{\mathbf{k}}-\tilde{\mathbf{k}}') \tag{2.14}$$

The decomposition of the vectors of equation (2.12) results in equality:

$$\Delta_\Gamma(\tilde{\mathbf{k}}-\tilde{\mathbf{k}}') = \sum_{s=1}^{L}\delta_{\mathbf{k}-\mathbf{k}'+\mathbf{q}_s} \tag{2.15}$$

Thus the expression (2.14) becomes:

$$\mathbf{G}(\mathbf{k},\mathbf{k}',\omega) = \frac{1}{L}\sum_{\mathbf{R},\mathbf{R}'}\sum_{s=1}^{L}\delta(\mathbf{k}-\mathbf{k}'+\mathbf{q}_s)\mathbf{G}_{\mathbf{R},\mathbf{R}'}(\mathbf{k},\omega)e^{-i\mathbf{k}\cdot\mathbf{R}}e^{i\mathbf{k}'\cdot\mathbf{R}'} \tag{2.16}$$

38
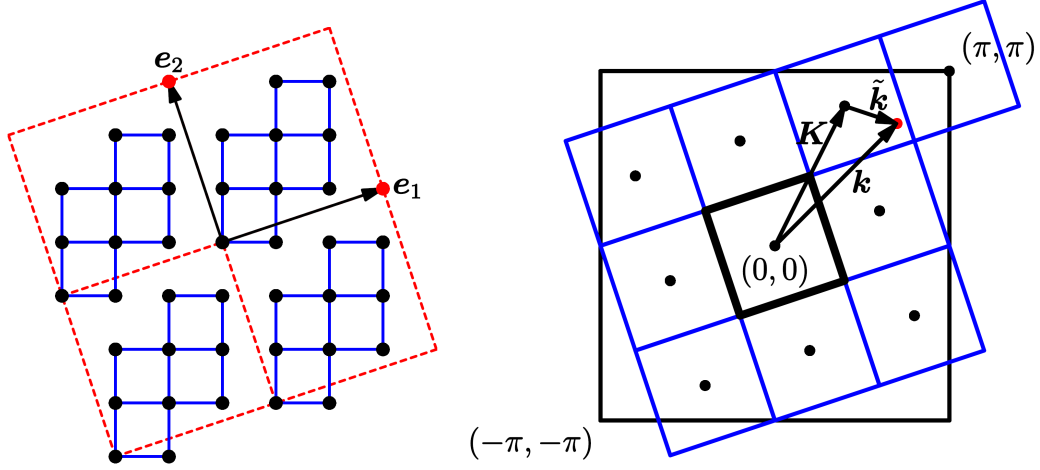
Figure 2.2
Left panel: Tiling of the square lattice with identical ten-site clusters ($L = 10$). The vectors $e_{1,2}$ define a super-lattice of clusters. Right panel: the corresponding Brillouin zones. The reduced Brillouin zone (tilted black square) is associated with the super-lattice and L copies of it can be fitted within the original Brillouin zone (large square).

The vector $\mathbf{q}_s$ belongs both to the reciprocal lattice Γ^* and to the Brillouin zone of the original lattice. In practice, we only retain the diagonal elements of Eq. (2.16). We can show that if $\mathbf{q}_s \neq 0$ the spectral weight includes both negative and positive values, however the sum of their contribution is zero. Using Eq. (2.13), we get the periodic Green function:

$$\mathbf{G}_{\text{per}}(\mathbf{k}, \omega) = \frac{1}{L} \sum_{\mathbf{R}, \mathbf{R}'} \mathbf{G}_{\mathbf{R}, \mathbf{R}'}(\mathbf{k}, \omega) e^{-i\mathbf{k} \cdot (\mathbf{R} - \mathbf{R}')} \tag{2.17}$$

In practice, we will be more interested in the spectral weight $A(\omega, \mathbf{k})$, deduced from Green's function of Eq. (2.17). It is expressed as follows:

$$\mathbf{A}(\omega, \mathbf{k}) = -2 \lim_{\eta \to 0} \text{Im} \left(\mathbf{G}_{\text{per}}(\mathbf{k}, \omega + i\eta) \right) \tag{2.18}$$

where η is a positive infinitesimal parameter.

One of the successes of the CPT is the agreement with the ARPES observations in the cuprates. Indeed, the spectral function obtained with CPT at the Fermi level describes in large parts the results obtained with ARPES.

Cluster perturbation theory is not applicable when we are interested in systems with spontaneous symmetry breaking. Dealing with these systems requires a variational principle which is absent from CPT. In the following subsections, we will focus on other numerical methods related to CPT that include this variational principle. However, before discussing these methods, we will show how $\mathbf{G}'(\omega)$ is obtained numerically by exact diagonalization.

2.2 Exact diagonalization

Although the quantum cluster methods are not dependent on a specic solver, in this section we will discuss the exact diagonalization solver we used. In this document, we are interested in superconductivity at zero temperature, which justifies our choice focused on exact diagonalization. It is a powerful tool for calculating the ground state $|\Omega\rangle$ and the Green function of the cluster. These quantities should be calculated iteratively using the Lanczos algorithm [4] or the band Lanczos algorithm [37]. The basic idea of exact diagonalization is to represent the Hubbard Hamiltonian in a small-dimensional subspace and solve it. This Hamiltonian in second quantization is:

$$H = -\sum_{ij,\sigma} t_{ij} c_{i\sigma}^{\dagger} c_{j\sigma} + U \sum_i n_{i\uparrow} n_{i\downarrow} \tag{2.19}$$

2.2.1 State coding

The first step in the exact diagonalization is to define a scheme that makes it possible to encode the quantum states. The occupancy number for an orbital μ is represented by $n_\mu = 0$ or $n_\mu = 1$. In terms of creation operators, any quantum state can be written in the form:

$$(c_{1\uparrow}^{\dagger})^{n_{1\uparrow}} (c_{2\uparrow}^{\dagger})^{n_{2\uparrow}} \cdots (c_{L\uparrow}^{\dagger})^{n_{L\uparrow}} (c_{1\downarrow}^{\dagger})^{n_{1\downarrow}} (c_{2\downarrow}^{\dagger})^{n_{2\downarrow}} \cdots (c_{L\downarrow}^{\dagger})^{n_{L\downarrow}} |0\rangle \tag{2.20}$$

where $|0\rangle$ is the vacuum state. The occupation numbers make a set of 0's and 1's that can be regarded as the binary representation of an integer. Thus the different integer numbers can be used to store the different quantum states of the system. A system with L orbital has 4^L states and we need 4^L integer numbers to store them. However, due to conservation laws, not all of these states are necessary. Commutation relations

$$[N_\uparrow, H] = [N_\downarrow, H] = 0 \tag{2.21}$$

indicate the conservation of the number of spin up ($N_\uparrow$) and spin down ($N_\downarrow$) electrons. Therefore, the exact diagonalization can be restricted to sectors of the Hilbert space of dimension d where $N_\uparrow$ and $N_\downarrow$ are xed. The dimension of the space in this case is given by:

$$d = d(N_\uparrow) d(N_\downarrow) \tag{2.22}$$

where the dimension $d(N_\sigma)$ is given by:

$$d(N_\sigma) = \frac{L!}{N_\sigma! \, (L - N_\sigma)!}. \tag{2.23}$$

For instance, in a system with L sites at half-filling, in a sector with zero total spin, the number of spin-up and spin-down electrons are equal:

$$N_\sigma = N_{-\sigma} = \frac{L}{2} \tag{2.24}$$

and equation 2.23 becomes:

$$d = \left(\frac{L!}{((L/2)!)^2} \right)^2.$$ (2.25)

By applying the Stirling approximation, we show that $d \approx 4^L$ and consequently, the Hilbert space of the system increases exponentially with the number of sites, this is the reason why this method is constrained to small clusters.

2.2.2 Construction and diagonalization of the Hamiltonian

The second step is the construction and diagonalization of the Hubbard Hamiltonian of equation (2.19). We write it as:

$$H = H_{0\uparrow} \otimes \mathbb{1} + \mathbb{1} \otimes H_{0\downarrow} + H_1$$ (2.26)

where $H_{0\uparrow}$ and $H_{0\downarrow}$ are respectively the operators of the kinetic energy of the up and down spin electrons, $\mathbb{1}$ the identity matrix and H_1 the Coulomb interaction. $H_{0\uparrow}$ and $H_{0\downarrow}$ represent the first term of the Hamiltonian (2.19). Likewise, H_1 represents the second term. To calculate the matrix elements of the Hamiltonian H, namely, $H_{0\sigma}$ and H_1, we proceed as follows: The H_1 matrix is diagonal in the basis of the occupancy number. There are also diagonal elements, coming from the chemical potential.
The $H_{0\sigma}$ matrix is a sparse matrix. The calculation of its matrix elements requires some attention because of the nature of the sign. After having established a coding scheme for the quantum basis states and having obtained the matrix elements of H, we must proceed to its diagonalization using the Lanczos algorithm which we will describe in what follows.

2.2.3 Lanczos algorithm: ground state

In general, the Lanczos method is used to determine the extreme (largest and smallest) eigenvalues of a matrix which is too large to be completely diagonalized. The basic idea of the method is to project the Hamiltonian (2.26) onto a Krylov space [49, 3]. The Krylov subspace $\mathscr{K}$ is generated by the action of $H, H^2, \cdots, H^q$ (for q iterations) on a vector $|\phi_0\rangle$:

$$\mathscr{K} = \text{span}\left(|\phi_0\rangle, H|\phi_0\rangle, H^2|\phi_0\rangle, \cdots, H^q|\phi_0\rangle\right)$$ (2.27)

The vectors generated in Eq. (2.27) are not mutually orthogonal. However, a sequence of orthogonal vectors can be obtained by the following recurrence relation:

$$|\phi_{n+1}\rangle = H|\phi_n\rangle - a_n|\phi_n\rangle - b_n^2|\phi_{n-1}\rangle$$ (2.28)

where the coefficients a_n and b_n are given by ($n \geq 0$):

$$a_n = \frac{\langle \phi_n|H|\phi_n \rangle}{\langle \phi_n|\phi_n \rangle} \quad \text{and} \quad b_n^2 = \frac{\langle \phi_n|\phi_n \rangle}{\langle \phi_{n-1}|\phi_{n-1} \rangle},$$ (2.29)

with the initial conditions $b_0 = 0$ and $|\phi_{-1}\rangle = 0$. In the base of normalized states:

$$|n\rangle = \frac{|\phi_n\rangle}{\sqrt{\langle\phi_n|\phi_n\rangle}},\tag{2.30}$$

the Hamiltonian H, obtained by projection, in matrix form, is [23]:

$$H = \begin{pmatrix} a_0 & b_1 & 0 & 0 & \cdots & 0 \\ b_1 & a_1 & b_2 & 0 & \cdots & 0 \\ 0 & b_2 & a_2 & b_3 & \cdots & 0 \\ \vdots & \vdots & \vdots & \vdots & \ddots & \vdots \\ 0 & 0 & 0 & 0 & \cdots & a_q \end{pmatrix}\tag{2.31}$$

The energy E_0 of the ground state $|\Omega\rangle$ of the Hamiltonian (2.31) is, to a precision determined by the number of iterations q, the lowest eigenvalue of H.

2.2.4 Lanczos algorithm for the cluster's Green function.

We saw previously how we get the ground state $|\Omega\rangle$ by the Lanczos method. However, we also need the Green function $G'_{\mu\nu}(\omega)$ at zero temperature, where we assume that ω is a complex frequency. It breaks down into a part $G'_{\mu\nu,e}(\omega)$ for the electrons and a component $G'_{\mu\nu,h}(\omega)$ for the holes:

$$G'_{\mu\nu}(\omega) = G'_{\mu\nu,e}(\omega) + G'_{\mu\nu,h}(\omega)\tag{2.32}$$

where, for electrons:

$$G'_{\mu\nu,e}(\omega) = \langle\Omega|c_\mu \frac{1}{\omega - H + E_0} c_\nu^\dagger|\Omega\rangle\tag{2.33}$$

and for the holes:

$$G'_{\mu\nu,h}(\omega) = \langle\Omega|c_\nu^\dagger \frac{1}{\omega + H - E_0} c_\mu|\Omega\rangle\tag{2.34}$$

The Lanczos algorithm allows to numerically evaluate the equation (2.32). To calculate the electron part of the Green function, $G'_{\mu\nu,e}(z)$ we do as follow. We try to estimate the action of $(z - H)^{-1}$ on a state $|\phi_\nu\rangle = c_\nu^\dagger|\Omega\rangle$ where $z = \omega + E_0$. Using the Taylor series:

$$(z - H)^{-1}|\phi_\nu\rangle = \left(\frac{1}{z} + \frac{1}{z^2}H + \frac{1}{z^3}H^2 + \cdots\right)|\phi_\nu\rangle\tag{2.35}$$

We see that the Krylov space constructed on $|\phi_\nu\rangle$ offers a good representation of:

$$\frac{1}{z - H}|\phi_\nu\rangle\tag{2.36}$$

42

From equations (2.27) and (2.31), and when $\mu = \nu$, the expression

$$G'_{\nu\nu}(z) = \langle \phi_\nu | \frac{1}{z-H} | \phi_\nu \rangle \tag{2.37}$$

leads to the representation in continuous fraction [23]:

$$G'_{\nu\nu}(z) = \cfrac{\langle \phi_\nu | \phi_\nu \rangle}{z - a_0 - \cfrac{b_1^2}{z - a_1 - \cfrac{b_2^2}{z - a_2 - \cfrac{b_3^2}{\cdots}}}} \tag{2.38}$$

The hole part of the Green function can be calculated in a similar method. In practice, we calculate the continued fraction (2.38) starting with the bottom floor. In the case where $\mu \neq \nu$ we proceed as follows. We dene

$$G'^{+}_{\mu\nu}(z) = \langle \Omega | (c_\mu + c_\nu) \frac{1}{z-H} (c_\mu + c_\nu)^\dagger | \Omega \rangle \tag{2.39}$$

which, using the symmetry $G'_{\mu\nu}(z) = G'_{\nu\mu}(z)$, leads to:

$$G'_{\mu\nu}(z) = \frac{1}{2} \left(G'^{+}_{\mu\nu}(z) - G'_{\nu\nu}(z) - G'_{\mu\mu}(z) \right) \tag{2.40}$$

where the $G'_{\mu\mu}(z)$ are calculated the same way as equation (2.38).

2.2.5   Band Lanczos algorithm for the cluster Green function.

An alternative method for calculating the cluster's Green function is the band Lanczos algorithm. It is a generalization of the Lanczos algorithm where the Krylov subspace is generated by more than one state. For a system of L states, this subspace, $\mathcal{K}'$, is written in the form:

$$\mathcal{K}' = \text{span}\{|\phi_1\rangle \cdots |\phi_L\rangle, H|\phi_1\rangle \cdots H|\phi_L\rangle, \cdots H^q|\phi_1\rangle \cdots H^q|\phi_L\rangle\} \tag{2.41}$$

Where the number of iterations q is controled by the convergence of the ground state of the Hamiltonian.

As in the previous Lanczos method, the structure of the matrix (2.31) remains valid, but with $2L$ diagonals around the first diagonal. Thus, the Krylov subspace, $\mathcal{K}'$, provides a Lehmann representation of the cluster's Green function as follows. By inserting the completeness relation in Krylov space:

$$\sum_m {}' |\phi_m\rangle \langle \phi_m| = \mathbb{1} \tag{2.42}$$

in expression (2.32), we get:

$$G'_{\nu\mu}(\omega) = \sum_m \langle \Omega | c_\mu | \phi_m \rangle \frac{1}{\omega - E_m + E_0} \langle \phi_m | c_\nu^\dagger | \Omega \rangle$$
$$+ \sum_n \langle \Omega | c_\nu^\dagger | \phi_n \rangle \frac{1}{\omega + E_n - E_0} \langle \phi_n | c_\mu | \Omega \rangle \tag{2.43}$$

where $|\phi_m\rangle$ and $|\phi_n\rangle$ are eigenstates of the Hamiltonian corresponding respectively to the eigenvalues E_m and E_n. The sum m and n relates respectively to a system of $N + 1$ and $N - 1$ electrons. In the following, we will adopt the following notation:

$$Q_{\mu m}^{(e)} = \langle \Omega | c_\mu | \phi_m \rangle \qquad Q_{\mu n}^{(h)} = \langle \Omega | c_\mu^\dagger | \phi_n \rangle \tag{2.44}$$

which are respectively matrices of $2LN^{(e)}$ and $2LN^{(h)}$ where $N^{(e)}$ is the number of states $|\phi_m\rangle$ and $N^{(h)}$ the number of states $|\phi_n\rangle$. In the same way, we dene:

$$\omega_m^{(e)} = E_m - E_0 \qquad \omega_n^{(h)} = -E_n + E_0 \tag{2.45}$$

Using these notations, the expression (2.43) becomes:

$$G'_{\nu\mu}(\omega) = \sum_m \frac{Q_{\mu m}^{(e)} Q_{\nu m}^{(e)*}}{\omega - \omega_m^{(e)}} + \sum_n \frac{Q_{\mu n}^{(h)} Q_{\nu n}^{(h)*}}{\omega - \omega_m^{(h)}} \tag{2.46}$$

We can vertically join the matrices $Q^{(e)}$ and $Q^{(h)}$ in a single matrix of dimension $2L \times N$ where $N = N^{(e)} + N^{(h)}$ and denote by ω_r the union of the sets $\{\omega_n^{(e)}\}$ and $\{\omega_n^{(h)}\}$. Thus, we can simplify the writing of Green function of equation (2.46):

$$G'_{\nu\mu}(\omega) = \sum_r \frac{Q_{\mu r} Q_{\nu r}^*}{\omega - \omega_r} \tag{2.47}$$

This last equation constitutes Lehmann's representation of the cluster's Green function. The band Lanczos method is more memory demanding, because $2L + 1$ vectors must be stored against three vectors, for the simple Lanczos method. In practice, the number of states in the Krylov subspace $\mathcal{K}'$, at convergence, is a few hundred, depending on the size of the system. Nevertheless, it remains the fastest, because all the pairs (μ, ν) are evaluated at the same time. In addition, as Expression (2.47) shows, the band Lanczos algorithm gives a Lehmann representation of the cluster's Green function. It is the algorithm that we have used in this document.

2.3 Potthoff's functional approach

In Section 2.1, we saw that cluster perturbation theory allows us to calculate the approximate Green function of the lattice using the exact Green function of the cluster and the

inter-cluster hopping matrix. Numerically, we evaluate the cluster's Green function by the exact diagonalization described in section 2.2. The spectral function $A(\mathbf{k}, \omega)$ of the lattice, that is an experimentally observable and corresponding to the imaginary part of the Green function of the lattice, is thus deduced. However, CPT alone is unable to describe systems where symmetry is broken, as it only deals with a finite subset of the original system. However, a spontaneous breaking of symmetry can only occur in an infinite system, that is to say in the thermodynamic limit.

In this section, we will summarize the self-energy functional approach (SFA) introduced in 2003 by Michael Potthoff [78, 84]. Essentially, we will see that, combined with other numerical methods, the functional self-energy approach makes it possible to deal very successfully with systems with broken symmetries.

More generally, numerical methods that deal with strongly correlated electron systems are generally based on Green functions via the formalism of Luttinger and Ward [60] and Baym and Kadanoff [5]. The grand potential Ω of the system is expressed as a functional of the Green function $G(\mathbf{k}, \omega)$. We have an exact variational approach in principle, but unfortunately, the functional $\Omega[G(\mathbf{k}, \omega)]$ is not explicitly known. It is given, by denition, by [81]:

$$\Omega[\mathbf{G}] = \Phi[\mathbf{G}] + \text{Tr}\ln(-\mathbf{G}) - \text{Tr}\{(\mathbf{G}_0^{-1} - \mathbf{G}^{-1})\mathbf{G}\} \tag{2.48}$$

where for an operator $\mathbf{A}$, $\text{Tr}\mathbf{A} = T\sum_{\omega,\alpha} A_{\alpha\alpha}(i\omega)$ and the $A_{\alpha\alpha}$ are the diagonal matrix elements. T is the temperature and the sum is over Matsubara frequencies $i\omega$ and degrees of freedom indices α. The Luttinger Ward functional $\Phi[\mathbf{G}]$ must be obtained from an infinite sum of irreducible two-particle diagrams, as shown in Figure 2.3. For this reason, we are always led to resort to approximations to numerically compute the functional $\Omega[\mathbf{G}(\mathbf{k}, \omega)]$. Potthoff distinguishes three types of approximation:

(i) the type I approximation: we have a variational principle, but we apply an approximation to the Euler equation, that is to say to:

$$\frac{\delta\Omega[\mathbf{G}(\mathbf{k}, \omega)]}{\delta\mathbf{G}} = 0 \tag{2.49}$$

(ii) the type II approximation: we apply an approximation to $\Omega[\mathbf{G}]$, for example by truncating the series of Figure 2.3, while keeping Euler's equation (2.49);

(iii) the type III approximation: here we truncate the space of Green functions, $\mathbf{G}$ (or self-energy functions Σ), i.e. the variational space is truncated. However, we compute the functional $\Omega[\mathbf{G}]$ exactly and we also apply Euler's equation, $\delta\Omega[\mathbf{G}]/\delta\mathbf{G}$, exactly. In this document, we will adopt the type III approximation, or the approach of the Potthoff functional. We will try to express the functional $\Omega[\mathbf{G}]$ as a function of the self-energy Σ, but restricted to the space of the physical self-energies of a cluster.

The functional $\Phi[\mathbf{G}]$ has several properties [81]. However, the most important property for us is the derivative of the Luttinger-Ward functional $\Phi[\mathbf{G}]$ with respect to $\mathbf{G}$ corresponds exactly to the self-energy $\Sigma[\mathbf{G}]$:

$$\Sigma = \Sigma[\mathbf{G}] = \frac{\delta\Phi[\mathbf{G}]}{\delta\mathbf{G}} \tag{2.50}$$

45
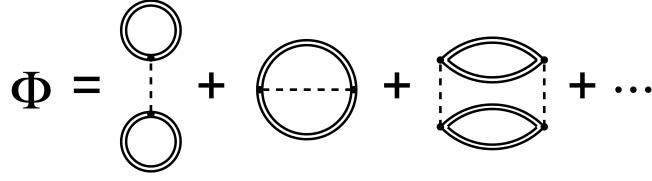
Figure 2.3
The classic denition of the Luttinger Ward functional. The lines represent the Green function and the dotted lines represent the Coulomb interaction (U) [82].

We can easily deduce this property from the irreducible diagrams of $\Phi[\mathbf{G}]$ where the derivative with respect to $\mathbf{G}$ gives us the self-energy. When $\mathbf{G}$ corresponds to the correct Green function of the system, the functional $\Omega[\mathbf{G}]$ becomes stationary at this point, that is to say:

$$\frac{\delta\Omega[\mathbf{G}]}{\delta\mathbf{G}} = 0 \tag{2.51}$$

which corresponds to the Dyson equation:

$$\mathbf{G}^{-1} = \mathbf{G}_0^{-1} - \mathbf{\Sigma} \tag{2.52}$$

We assume that the functional $\mathbf{\Sigma}[\mathbf{G}]$ of equation (2.50) is invertible, so we can write:

$$\mathbf{G} = \mathbf{G}[\mathbf{\Sigma}] \tag{2.53}$$

However, this assumption can be wrong during a phase transition. Thus we can build a new functional, $F[\mathbf{\Sigma}]$, dependent on self-energy, which is the Legendre transform of the Luttinger-Ward functional:

$$F[\mathbf{\Sigma}] = \Phi[\mathbf{G}[\mathbf{\Sigma}]] - \mathrm{Tr}(\mathbf{\Sigma}\mathbf{G}[\mathbf{\Sigma}]) \tag{2.54}$$

Like the functional $\Phi[\mathbf{G}]$, $F[\mathbf{\Sigma}]$ is not known explicitly. Using equation (2.50), we can show that:

$$\mathbf{G}[\mathbf{\Sigma}] = -\frac{\delta F[\mathbf{\Sigma}]}{\delta\mathbf{\Sigma}} \tag{2.55}$$

We now dene the Potthoff functional $\Omega_{\mathbf{t}}[\mathbf{\Sigma}]$ which is a functional of the self-energy:

$$\Omega_{\mathbf{t}}[\mathbf{\Sigma}] = F[\mathbf{\Sigma}] + \mathrm{Tr}\ln\left[-(\mathbf{G}_0^{-1} - \mathbf{\Sigma})^{-1}\right] \tag{2.56}$$

The index $\mathbf{t}$, indicates the dependence of Ω on $\mathbf{t}$, coming from the free Green function $\mathbf{G}_0$:

$$\mathbf{G}_0^{-1} = i\omega - \mathbf{t} \tag{2.57}$$

When the self-energy corresponds to the correct self-energy of the system, we obtain:

$$\frac{\delta\Omega_{\mathbf{t}}[\boldsymbol{\Sigma}]}{\delta\boldsymbol{\Sigma}} = \boldsymbol{\Sigma} - \mathbf{G}^{-1} - \mathbf{G}_{0\mathbf{t}}^{-1} = 0 \tag{2.58}$$

Consequently for this value of self-energy, $\Omega_{\mathbf{t}}[\boldsymbol{\Sigma}]$ is stationary. However, the stationary solution is not accessible for all self-energies, but in a restricted domain of $\boldsymbol{\Sigma}(\mathbf{t}', \mathbf{U})$, as shown in Figure 2.4 we can find it. The quantity $\mathbf{t}'$ is the hopping matrix of a reference system. The reference system has the same $\mathbf{U}$ interactions as the original system but, their hopping matrices are different, that is, $\mathbf{t} \neq \mathbf{t}'$. In this document, the reference system is a set of clusters. Similar to equation (2.56), we can write the Potthoff functional for the cluster as:

$$\Omega_{\mathbf{t}'}[\boldsymbol{\Sigma}] = F[\boldsymbol{\Sigma}] + \operatorname{Tr}\ln\left[-(\mathbf{G}_0'^{-1} - \boldsymbol{\Sigma})^{-1}\right] \tag{2.59}$$

with the Green function, $\mathbf{G}_0'^{-1}$, given by:

$$\mathbf{G}_0'^{-1} = i\omega - \mathbf{t}' \tag{2.60}$$

The Luttinger Ward functional, $\Phi[\mathbf{G}]$, is a universal quantity, that is to say that it does not change for two systems which differ only by their hopping matrix. As a consequence, its Legendre transform, $F[\boldsymbol{\Sigma}]$ is also universal. Thus, the two equations of the Potthoff functional $\Omega_{\mathbf{t}}[\boldsymbol{\Sigma}]$ and $\Omega_{\mathbf{t}'}[\boldsymbol{\Sigma}]$, respectively, for the original system and the cluster are identical in the expressions. By combining equations (2.56) and (2.59), we obtain the Potthoff functional used in numerical calculations [82]:

$$\Omega_{\mathbf{t}}[\boldsymbol{\Sigma}] = \Omega_{\mathbf{t}'}[\boldsymbol{\Sigma}] + \operatorname{Tr}\ln\{-[\mathbf{G}_0^{-1} - \boldsymbol{\Sigma}(\mathbf{t}')]^{-1}\} - \operatorname{Tr}\ln(-\mathbf{G}') \tag{2.61}$$

2.4 Variational cluster approximation

The variational cluster approximation (VCA) can be seen as an extension of cluster perturbation theory, where certain parameters of the Hamiltonian of the cluster are determined according to the variational principle of the self-energy functional, described previously. The purpose of VCA is to deal with systems susceptible to spontaneous symmetry breaking. Indeed, the cluster perturbation theory is not able to deal with these systems: CPT is not accompanied by a variational principle making it possible to fix the value of the Weiss field. In principle, we must adopt the VCA method to have a variational principle, to determine the values of the Weiss fields. In what follows, we look at the notion of Weiss field.
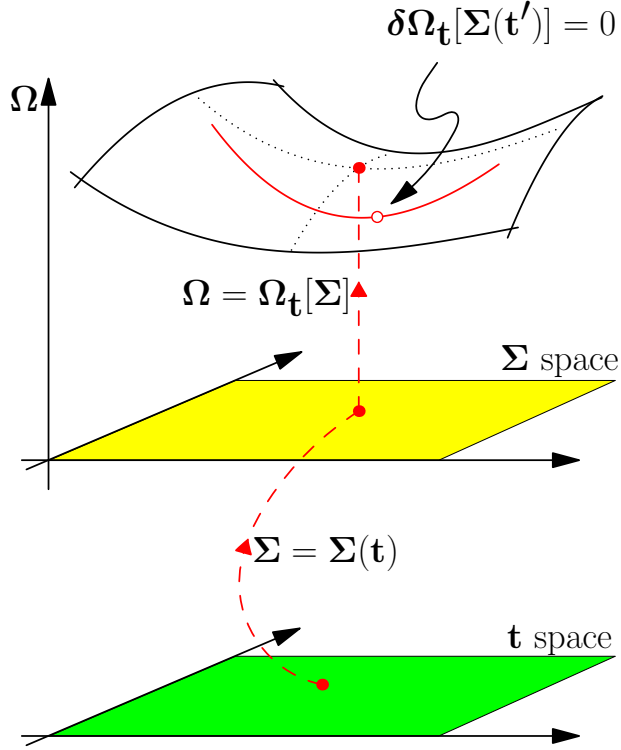
Figure 2.4

Schematic illustration of the self-energy functional approximation. Ω is a functional of $\Sigma(\mathbf{t})$ where $\mathbf{t}$ is the hopping term of the Hamiltonian and the Hubbard interaction (U) is fixed. When Σ corresponds to the correct self-energy of the system, Ω becomes stationary (red dots). However, it is not accessible in the overall Σ-space, but in a restricted domain where Σ depends on $\mathbf{t}$ of the reference system (cluster for example). The latter has the same U interaction as the original system. Ω can be evaluated exactly for the reference system and lead to an approximated self-energy and a large potential to the real system [81].

2.4.1 Weiss fields

To study the possibility of symmetry breaking of a system with quantum cluster methods, we add operators capable of breaking this symmetry to the cluster Hamiltonian. These operators are called Weiss fields (In practice, we often call "Weiss fields" the amplitude of these operators). For example, the antiferromagnetic Hamiltonian in the case of the honeycomb lattice is of the form:

$$H_{Af} = h_{AF}\left\{\sum_{i\in A}(n_{i\uparrow} - n_{i\downarrow}) - \sum_{i\in B}(n_{i\uparrow} - n_{i\downarrow})\right\}. \tag{2.62}$$

where h_{AF} is called the antiferromagnetic Weiss field. Figure 2.5 shows the Potthoff functional as a function of the Weiss field h_{AF}, for a six-site hexagonal cluster and a

ten-site cluster at $U = 6$ and half-filled. The black dots indicate the value of the optimal Weiss field where the Potthoff functional has a minimum. We see that as the cluster
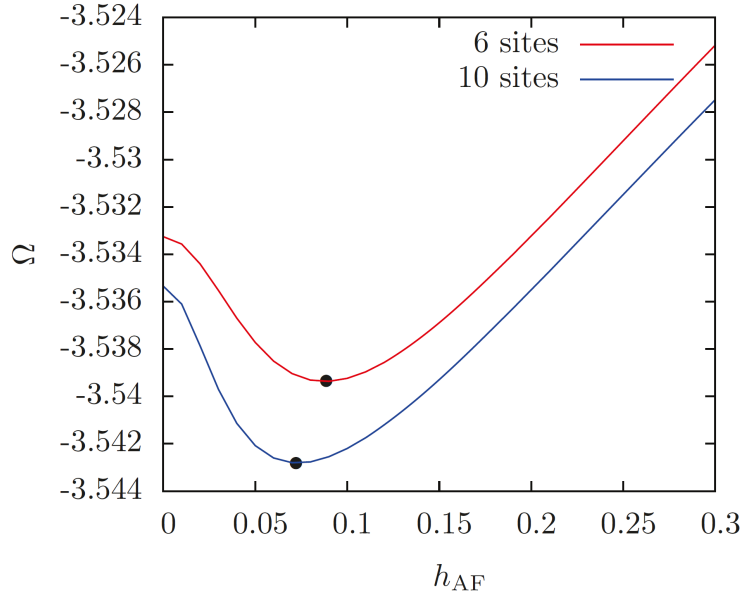
Figure 2.5
The Potthoff functional as a function of the h_{AF}, the antiferromagnetic Weiss field of the half-filled honeycomb lattice. In red, for a hexagonal cluster of six sites and in blue, a cluster of ten sites (two hexagons), $U/t = 6$. We can clearly see that the optimal Weiss field, indicated by the black point, decreases when the system size increases.

size increases, the optimal Weiss field decreases. Indeed, in quantum cluster methods, the Weiss field only makes it possible to break a spontaneous symmetry which can only appear in an infinite cluster. Therefore, the more the cluster size increases, the easier it becomes to break the symmetry, and the more the value of the optimal Weiss field decreases. In principle, one should expect a zero optimal Weiss field within the infinite size limit. It is important to note that the Weiss field of quantum cluster methods is different from the Weiss field of ordinary mean field theory. Indeed, in quantum cluster methods, the Weiss field and the order parameter are different, unlike ordinary mean field theory, where they are proportional.

The study of superconductivity, on the other hand, is done by adding, to the Hamiltonian of the cluster, anomalous Weiss fields that are likely to create or destroy Cooper pairs. In the case of the honeycomb lattice, the anomalous operators, of singlet or triplet
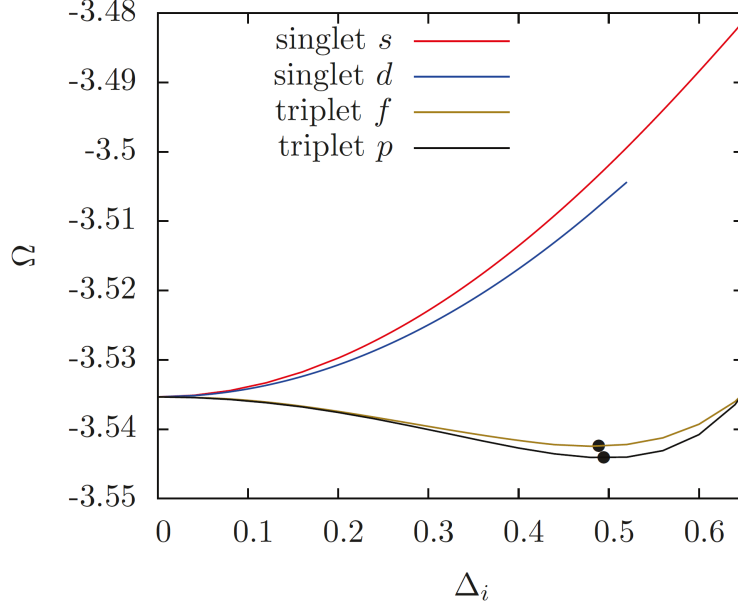
Figure 2.6
The Potthoff functional Ω as a function of the superconducting Weiss fields of the half-filled honeycomb lattice. The Weiss field Δ_i for $i = s, d, p$ or f and $U = 6t$. A six-site hexagonal cluster was used. Triplet-type superconductivity exists at half-filling, because Ω has a minimum, indicated by black dots, at a non-zero optimal Weiss field, unlike singlet types. Note: this neglects other orders (like AF), which would exist at this value of U.

type, are dened in the form:

$$\Delta_{singlet} = \sum_{\mathbf{r}} (\Delta_1 S_{1,\mathbf{r}} + \Delta_2 S_{2,\mathbf{r}} + \Delta_3 S_{3,\mathbf{r}})$$

$$\Delta_{triplet} = \sum_{\mathbf{r}} (\Delta_1 T_{1,\mathbf{r}} + \Delta_2 T_{2,\mathbf{r}} + \Delta_3 T_{3,\mathbf{r}}) \tag{2.63}$$

where $S_{i\mathbf{r}}$ and $T_{i\mathbf{r}}$ are the singlet and triplet pairing operators:

$$S_{i,\mathbf{r}} = c_{\mathbf{r},\uparrow} c_{\mathbf{r}+\mathbf{e}_i,\downarrow} - c_{\mathbf{r},\downarrow} c_{\mathbf{r}+\mathbf{e}_i,\uparrow},$$

$$T_{i,\mathbf{r}} = c_{\mathbf{r},\uparrow} c_{\mathbf{r}+\mathbf{e}_i,\downarrow} + c_{\mathbf{r},\downarrow} c_{\mathbf{r}+\mathbf{e}_i,\uparrow},$$

The superconducting Weiss fields are the coefficients Δ_i which, according to their denitions, can lead to a singlet symmetry like s, d and $d + id$ or a triplet like p, f and $p + ip$. Figure 2.6 describes the Potthoff functional Ω as a function of the Weiss field Δ_i (for example, $i = s$ corresponds to the s symmetry) of the half-filled honeycomb lattice. The solutions with singlet symmetries that were obtained using VCA, correspond to a zero Weiss field and thus identify with the normal solution.

Figure 2.7 shows the results of another calculation that has been done for the honeycomb lattice, out of half-filling, at $U = 4t$ and $\mu = 3.2t$. It shows Ω has a minimum
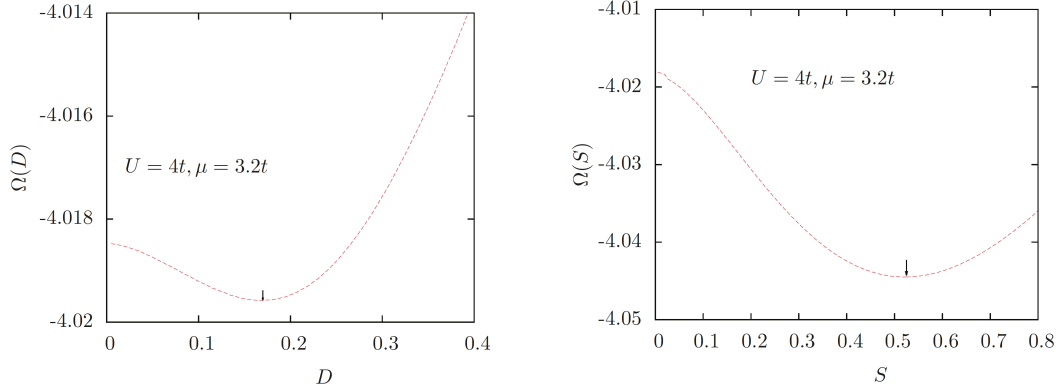
Figure 2.7
Potthoff functional as a function of the superconducting, singlet Weiss fields of the honeycomb lattice. A six-site hexagonal cluster was used with $U = 4t$ and the chemical potential, $\mu = 3.2t$. The functional Ω shows a minimum at half-filling, unlike in figure 2.6.

at a non-zero optimal Weiss field for two singlet-type superconductivity (d-wave and s-wave). Singlet superconductivity, in this system, can exist only when the system is doped, unlike triplet superconductivity [31]. Physically, the minimum of the Potthoff functional Ω is a signature of possibility of emergence of the order defined by the Weiss field. However, the different values of the Weiss field must be determined iteratively in the variational cluster approximation using the variational principle of self-energy functional. In what follows, we are interested in the variational cluster approximation.

2.4.2 The VCA procedure

Based on the self-energy functional, the reference system of the VCA, is a set of clusters repeated in an identical manner on the original network. In VCA, the self-energy of the system is approximated by the self-energy of the cluster. The value of the latter must be determined by adding Weiss fields to the Hamiltonian of the cluster. We x the parameters of these Weiss fields by calculating the Potthoff functional of equation (2.48). Unlike ordinary mean-field methods, VCA correctly accounts for the effects of short-range correlations. The advantage of VCA, compared to cluster perturbation theory, is its ability to describe long-range orders when a suitable Weiss field for symmetry breaking is added to the cluster Hamiltonian. From a microscopic point of view, the coexistence of several phases can be studied using one or more Weiss fields for each of the possible symmetries.

The procedure in the variational cluster approximation is as follows:
(i) we add to the Hamiltonian of the cluster, a Weiss field adapted to the symmetry we want to break. This choice must be guided by the possibilities of breaking symmetries of the system to be studied.

51

(ii) for each value of the Weiss field the exact Green function of the cluster must be computed using the Lanczos or band Lanczos algorithm. Then we optimize the Potthoff functional in the space of variational parameters.

(iii) In the last step of VCA we calculate the properties of the system such as the order parameters at this optimal point.

The variational cluster approximation is limited to a small number of variational parameters. In the next section, we will describe the cluster dynamical mean-field theory, which takes into account the effect of the lattice environment on the cluster using auxiliary bath orbitals.

2.5 Cluster dynamical mean field theory

Cluster dynamical mean field theory (CDMFT) [47] is an extension of dynamic mean field theory. The basic idea is to model the effects of the environment on the cluster by a set of coupled auxiliary degrees of freedom. These degrees of freedom form an effective environment in which the cluster is immersed, and are therefore called bath orbitals. Figure 2.8 shows the example of a four-site cluster with its six bath orbitals, within a honeycomb lattice. The black circles represent the sites and the small red squares the bath orbitals. The black lines represent the $t_{\mu\nu}$ hopping terms between the μ and ν sites of the cluster, and the dotted lines represent the $\theta_{\mu\alpha}$ hopping terms between the cluster sites and the bath orbitals. In CDMFT, the cluster plays the role of the impurity in Anderson's model [1]. Thus the Hamiltonian of the cluster-environment system is of the form:

$$H' = \sum_{\mu\nu} t_{\mu\nu} c_\mu^\dagger c_\nu + U \sum_{\mathbf{R}} n_{\mathbf{R}\uparrow} n_{\mathbf{R}\downarrow} + \sum_{\mu\alpha} \theta_{\mu\alpha}(c_\mu^\dagger a_\alpha + H.c) + \sum_\alpha \varepsilon_\alpha a_\alpha^\dagger a_\alpha \qquad (2.64)$$

In this expression, the operator $c_\mu^\dagger$ creates an electron in the $\mu = (\mathbf{R}, \sigma)$ orbital of the cluster while, c_μ destroys it. Likewise, $a_\alpha^\dagger$ creates and a_α destroys an electron in the α bath orbital. The ε_α are the energies of these bath orbitals. By tracing over these bath orbitals, the Green's function, $\mathbf{G}'$, of the Hamiltonian (2.64) takes the form:

$$\mathbf{G}'^{-1}(\omega) = \omega - \mathbf{t}' - \mathbf{\Gamma}(\omega) - \mathbf{\Sigma}(\omega) \qquad (2.65)$$

where the hybridization matrix $\mathbf{\Gamma}$ describes the effect of bath orbitals on the electron's Green function. Its matrix elements $\Gamma_{\mu\nu}$, are defined by the energies of the bath orbitals and the $\theta_{\mu\alpha}$ hybridization terms:

$$\Gamma_{\mu\nu}(\omega) = \sum_\alpha \frac{\theta_{\mu\alpha} \theta_{\nu\alpha}^*}{\omega - \varepsilon_\alpha} \qquad (2.66)$$

The energies of the bath orbitals, as well as the hybridization terms must be determined by the self-consistency condition:

$$\bar{\mathbf{G}}(\omega) = \mathbf{G}'(\omega) \qquad (2.67)$$
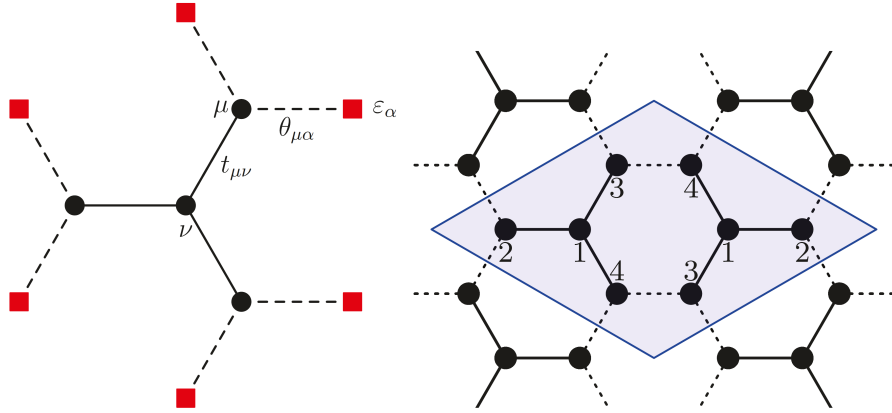
Figure 2.8
Left: Illustration of a honeycomb lattice cluster with its eight bath orbitals. The dark circles are the sites of the cluster, and the red squares are the bath orbitals. $t_{\mu\nu}$ is the hopping amplitude between the μ and ν sites of the cluster, and $\theta_{\mu\alpha}$ is the hopping amplitude between the μ site of the cluster and the α bath orbital. The energy of the α bath orbital is denoted by ε_{α}. This cluster must be accompanied by its inverted image to form a tessellation of the lattice as shown in the colored area of the figure on the right.

where $\bar{\mathbf{G}}$ is the average of the Green function over the superlattice i.e. the Fourier transform giving the local Green function:

$$\bar{\mathbf{G}}(\omega) = \sum_{\tilde{\mathbf{k}}} \mathbf{G}(\tilde{\mathbf{k}}, \omega) \tag{2.68}$$

and where $\mathbf{G}(\tilde{\mathbf{k}}, \omega)$ is dened by the Dyson equation:

$$\mathbf{G}^{-1}(\tilde{\mathbf{k}}, \omega) = \mathbf{G}_0^{-1}(\tilde{\mathbf{k}}, \omega) - \Sigma(\omega) \tag{2.69}$$

In this expression, the self-energy of the system Σ is replaced by the self-energy of the cluster. In principle, if Γ represents the cluster environment well, equation (2.68) satisfies the equality:

$$\bar{\mathbf{G}}(\omega) = \mathbf{G}'(\omega) \tag{2.70}$$

However, the self-consistency condition (2.67) cannot be satisfied with a finite number of bath parameters. Therefore, we apply the minimization condition by calculating the distance function:

$$d = \sum_{i\omega_n} W(i\omega_n) \left| \mathbf{G}'^{-1}(i\omega_n) - \bar{\mathbf{G}}^{-1}(i\omega_n) \right|^2 \tag{2.71}$$

where the sum is to be done over the Matsubara frequencies ω_n, and the weights $W(i\omega_n)$ are used to give importance to the low frequencies. At this point, changing the values of
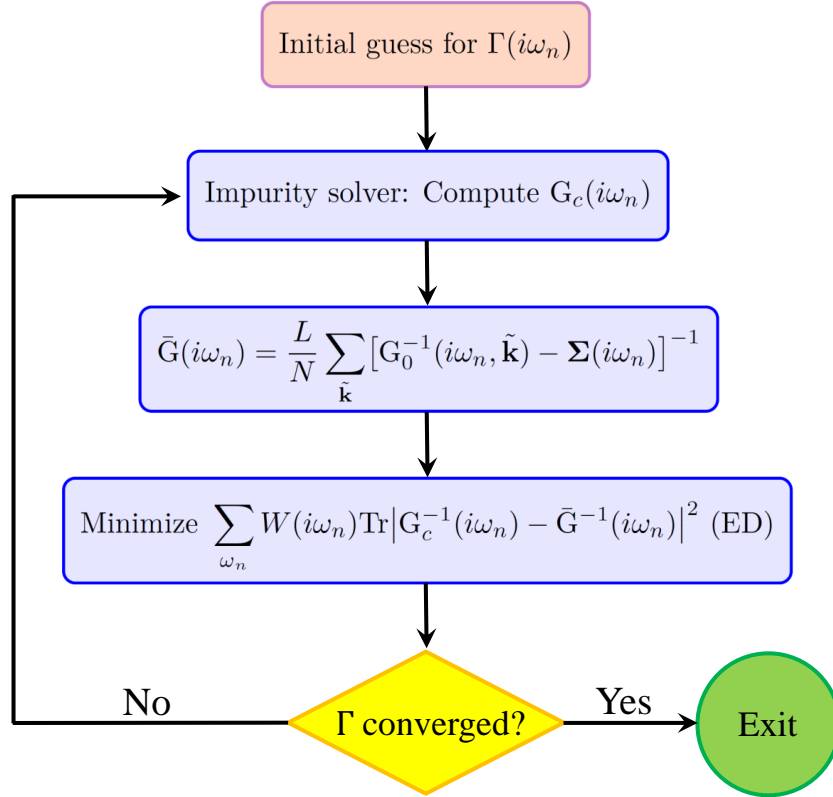
Figure 2.9
The CDMFT algorithm which describes the different steps of the method.

the bath parameters does not correspond to a new solution of the Hamiltonian (2.64). However, the hybridization function is often recalculated.

Figure 2.9 shows the CDMFT algorithm, which includes the following steps:
(i) We start with guess values of the bath parameters which define the hybridization function (2.66);
(ii) We calculate the Green function (2.65) of the cluster;
(iii) the projection $\bar{\mathbf{G}}$ is calculated;
(iv) We minimize the distance function of expression (2.71) and update the bath parameters
(v) Finally, if the bath parameters converge, we exit the loop otherwise we return to step (ii).

Cluster dynamical mean field theory is particularly useful in the study of phase transitions, for example the Mott transition. It can be used in the determination of the superconducting order parameter, if pairing terms are defined on the bath or between the cluster sites and those of the bath.

2.6 Limitations of quantum cluster methods.

The power of quantum cluster methods lies in their ability to include short-range spatial correlations, but also dynamic correlations. However, like most numeric methods, they have limitations:

(i) They do not take into account long-range correlations, which may be due to two-body uctuations. Consequently, they are not sensitive to the destabilization of orders due to collective stimulus. In particular they do not contain the physics of the Mermin-Wagner theorem.

(ii) The orders detectable by these methods are predicted a priori as in the case of mean field theory. Here the bath parameters and the Weiss fields must allow the breaking of the desired symmetries that can emerge in the system to be studied.

(iii) The orders studied with quantum cluster methods must have a short periodicity, that is, only commensurable orders are taken into account.

(iv) All excitations due to two bodies are confined to the cluster and therefore suffer from size effects.

Chapter 3

Superconductivity in twisted bilayer graphene

In this chapter, we will examine the superconducting phase in twisted bilayer graphene. To study this issue, we first use the symmetries in the honeycomb lattice to extract the available order parameters of this structure then using the CDMFT method, we will investigate the electron pairing in the superconducting phase corresponds to which one of the defined order parameters. The material of this chapter is published in SciPost Phys. 11, 017 (2021) [75]

3.1 Pairing symmetries in a hexagonal lattice

We are going to study the point group symmetry of the hexagonal lattice and use it to define appropriate superconducting (SC) order parameters. This study could be done in real or reciprocal space. In reference [10], all the pairing operators associated to the different irreducible representations of D_{6h} are classified in terms of low degree polynomials of momentum in reciprocal space. A different approach is adopted here, involving a real-space description of pairing operators defined on adjacent sites. Due to the on-site repulsion between electrons, U, on-site (singlet) pairing is almost impossible. The relevant pairing operators dened on the links between adjacent sites are

$$
\begin{aligned}
\text{singlet:} \quad & S_{i,\mathbf{r}} = c_{\mathbf{r},\uparrow} c_{\mathbf{r}+\mathbf{e}_i,\downarrow} - c_{\mathbf{r},\downarrow} c_{\mathbf{r}+\mathbf{e}_i,\uparrow}, \\
\text{triplet:} \quad & T_{i,\mathbf{r}} = c_{\mathbf{r},\uparrow} c_{\mathbf{r}+\mathbf{e}_i,\downarrow} + c_{\mathbf{r},\downarrow} c_{\mathbf{r}+\mathbf{e}_i,\uparrow}.
\end{aligned}
\tag{3.1}
$$

Where $\mathbf{e}_{1,2,3}$ are the 3 nearest neighbor vectors on the graphene lattice. These directions, give rise to a set of six pairing operators per site and we can combine them into operators

having a well-defined symmetry:

$$\hat{\Delta}_{\text{singlet}} = \sum_{\mathbf{r}} (\Delta_1 S_{1,\mathbf{r}} + \Delta_2 S_{2,\mathbf{r}} + \Delta_3 S_{3,\mathbf{r}}),$$

$$\hat{\Delta}_{\text{triplet}} = \sum_{\mathbf{r}} (\Delta_1 T_{1,\mathbf{r}} + \Delta_2 T_{2,\mathbf{r}} + \Delta_3 T_{3,\mathbf{r}}), \tag{3.2}$$

where the relative amplitudes $(\Delta_1, \Delta_2, \Delta_3)$ determine the symmetry of each operator. In this case the irreducible representations (irreps) of D_{6h}, which is equivalent to C_{6v} for a purely two-dimensional system, are used to classify the pairing operators. Here I am going to ilustrate how we can use the symmetries in such a system to define appropriate order parameters for it.

After realizing all the symmetris of a system, it is easy to find the relevant symmetry group and the associated character table. For a 2D hexagonal structure (graphene lattice), C_{6v} is the relevant symmetry group and its character table is shown in Table 3.1. The first row of this table lists the symmetry operations in the system (more precisely, the conjugacy classes): E is the identity operator, C_n is a $2\pi/n$ rotation operator around the vertical axis crossing from the hexagonal center and $\sigma_{d,v}$ are the reflection operators illustrated in the drawing next to Table 3.1.

$\mathbf{C}_{6v}$	E	C_2	$2C_3$	$2C_6$	$3\sigma_d$	$3\sigma_v$
A_1	1	1	1	1	1	1
A_2	1	1	1	1	-1	-1
B_1	1	-1	1	-1	-1	1
B_2	1	-1	1	-1	1	-1
E_1	2	-2	-1	1	0	0
E_2	2	2	-1	-1	0	0
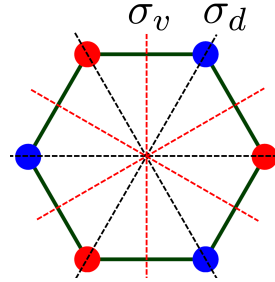
Table 3.1
Character Table for the C_{6v} Point Group. The first line of the table shows the symmetry operators of the hexagonal lattice. E is the identity element, C_n is an inplane rotation by $2\pi/n$ around the hexagonal center and $\sigma_{d,v}$ is the reflection operator. On the right: schematic view of the hexagonal cell of the graphene lattice. Black and red dashed lines show the reflection planes.

The first coulumn of the table shows the different irreducible representations of C_{6v}. This symmetry group has four 1D ($A_{1,2}$ and $B_{1,2}$) and two 2D ($E_{1,2}$) irreducible representations. The other columns show the character of each operator in different representations.

In a hexagonal lattice each site has 3 nearest neighbors and we want to define the pairing operators between two electrons located on nearest neighbor sites. According to Eq. 3.1 we can define six pairing operators for each site (three singlets and three
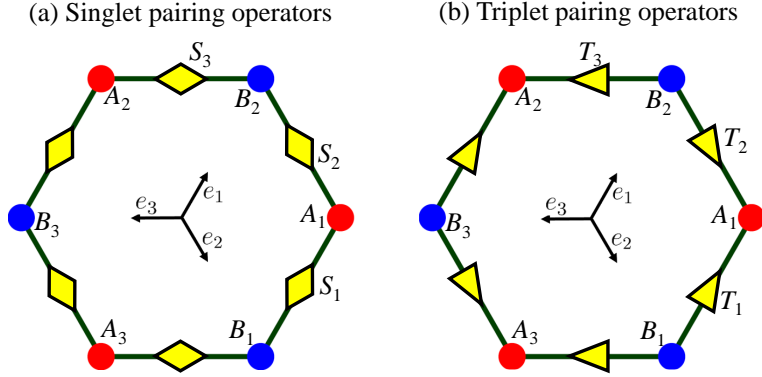
Figure 3.1
Shematic representation of pairing operators. Pairing operators along $\mathbf{e}_j$ are called S_j and T_j for singlet and triplet pairings.

triplets). A shematic representation of these operators is shown in Fig. 3.1. The second step is to know how these pairing operators change under the symmetry operations of Table 3.1. Let us illustrate this using a simple example. Consider the triplet pairing operator along the $\mathbf{e}_1$ direction that we call T_1 in Fig. 3.1.

$$T_1 = C_{B_1,\uparrow}C_{A_1,\downarrow} + C_{B_1,\downarrow}C_{A_1,\uparrow} \tag{3.3}$$

Let the system rotate by an angle $2\pi/6$ around the hexagonal center. This rotation maps B_1 and A_1 in Fig. 3.1 to A_1 and B_2, respectively, and therefore T_1 changes like

$$T_1 \xrightarrow{C_6} C_{A_1,\uparrow}C_{B_2,\downarrow} + C_{A_1,\downarrow}C_{B_2,\uparrow} = -\left(C_{B_2,\uparrow}C_{A_1,\downarrow} + C_{B_2,\downarrow}C_{A_1,\uparrow}\right) = -T_2, \tag{3.4}$$

where we used the anticommutation relations between anihilation operators. Thus T_1 goes to $-T_2$ after applying C_6. Table 3.2 shows how the symmetry operators of the system, listed in tabel 3.1, change the singlet and triplet pairing operators that we defined in Eq. 3.1 (E is the identity element of the symmetry group and does not change any pairing operator).

C_2	C_3	C_6	σ_d	σ_v
$S_1 \to S_1$	$S_1 \to S_3$	$S_1 \to S_2$	$S_1 \to S_1$	$S_1 \to S_2$
$S_2 \to S_2$	$S_2 \to S_1$	$S_2 \to S_3$	$S_2 \to S_3$	$S_2 \to S_1$
$S_3 \to S_3$	$S_3 \to S_2$	$S_3 \to S_1$	$S_3 \to S_2$	$S_3 \to S_3$

C_2	C_3	C_6	σ_d	σ_v
$T_1 \to -T_1$	$T_1 \to T_3$	$T_1 \to -T_2$	$T_1 \to T_1$	$T_1 \to -T_2$
$T_2 \to -T_2$	$T_2 \to T_1$	$T_2 \to -T_3$	$T_2 \to T_3$	$T_2 \to -T_1$
$T_3 \to -T_3$	$T_3 \to T_2$	$T_3 \to -T_1$	$T_3 \to T_2$	$T_3 \to -T_3$

Table 3.2
Left and right tabels show how the singlet and triplet pairing operators change under group elements of C_{6v} symmetry group in a hexagonal lattice. All the pairing operators are invariant under identity element (E).

Now we are going to define approprite order parameters for the superconducting phase on the hexagonal lattice. We have to find linear combinations (Eq. 3.1) of pairing operators (S_i and T_i) which satisfy the symmetry properties of the C_{6v} character table. We define the symmetric s-wave singlet order parameter as

$$\hat{\Delta}_s = \sum_{\mathbf{r}}(S_{1,r} + S_{2,r} + S_{3,r}).$$

Using Table 3.2 we see that $\hat{\Delta}_s$ is invariant under all symmetry operations. Thus $\hat{\Delta}_s$ is an acceptable order parameter associated to the A_1 representation (in this representation all charachters are equal to 1). The second example is about the two chiral combinations

Irrep	Symbol	Operators
A_1	s	$\hat{\Delta}_s = \sum_r (S_{1,r} + S_{2,r} + S_{3,r})$
B_2	f	$\hat{\Delta}_f = \sum_r (T_{1,r} + T_{2,r} + T_{3,r})$
E_2	d	$\hat{\Delta}_{d,1} = \sum_r (S_{1,r} - S_{2,r})$
		$\hat{\Delta}_{d,2} = \sum_r (S_{1,r} - S_{3,r})$
E_1	p	$\hat{\Delta}_{p,1} = \sum_r (T_{1,r} - T_{2,r})$
		$\hat{\Delta}_{p,2} = \sum_r (T_{1,r} - T_{3,r})$
Chiral representations		
E_2	$d+id$	$\hat{\Delta}_{d+id} = \sum_r (S_{1,r} + e^{2\pi i/3}S_{2,r} + e^{4\pi i/3}S_{3,r})$
	$d-id$	$\hat{\Delta}_{d-id} = \sum_r (S_{1,r} + e^{-2\pi i/3}S_{2,r} + e^{-4\pi i/3}S_{3,r})$
E_1	$p+ip$	$\hat{\Delta}_{p+ip} = \sum_r (T_{1,r} + e^{2\pi i/3}T_{2,r} + e^{4\pi i/3}T_{3,r})$
	$p-ip$	$\hat{\Delta}_{p-ip} = \sum_r (T_{1,r} + e^{-2\pi i/3}T_{2,r} + e^{-4\pi i/3}T_{3,r})$

Table 3.3
Symetricaly well-defined pairing operators associated with the irreducible representations (Irrep) of the C_{6v} symmetry group. S_j and T_j are singlet and triplet pairing along $\mathbf{e}_j$ (see Fig. 3.1). The last four lines are chiral representations, which are complex combinations of the real operators dened under E_1 and E_2.

of triplet pairing operators that we call $p + ip$ and $p - ip$, defined as

$$\hat{\Delta}_{p+ip} = \sum_{\mathbf{r}} (T_{1,\mathbf{r}} + \omega T_{2,\mathbf{r}} + \bar{\omega} T_{3,\mathbf{r}}),$$

$$\hat{\Delta}_{p-ip} = \sum_{\mathbf{r}} (T_{1,\mathbf{r}} + \bar{\omega} T_{2,\mathbf{r}} + \omega T_{3,\mathbf{r}}), \tag{3.5}$$

where $\omega = e^{2\pi i/3}$ and $\bar{\omega} = e^{-2\pi i/3}$. Using Table 3.2, it is easy to find how the C_{6v} symmetry group elements acts on these triplet chiral order parameters. One important point is that the two reflection operators (σ_v and σ_v) exchange $\hat{\Delta}_{p+ip}$ and $\hat{\Delta}_{p-ip}$ and therefore we have to use a 2D representation to express the transformation. In the fowlloing, I use the abbreviation $\hat{\Delta}_{p+ip} \equiv \hat{\Delta}_+$ and $\hat{\Delta}_{p-ip} \equiv \hat{\Delta}_-$ to simplify:

$$E \begin{pmatrix} \hat{\Delta}_+ \\ \hat{\Delta}_- \end{pmatrix} = \begin{pmatrix} 1 & 0 \\ 0 & 1 \end{pmatrix} \begin{pmatrix} \hat{\Delta}_+ \\ \hat{\Delta}_- \end{pmatrix}, \qquad C_2 \begin{pmatrix} \hat{\Delta}_+ \\ \hat{\Delta}_- \end{pmatrix} = \begin{pmatrix} -1 & 0 \\ 0 & -1 \end{pmatrix} \begin{pmatrix} \hat{\Delta}_+ \\ \hat{\Delta}_- \end{pmatrix},$$

$$C_3 \begin{pmatrix} \hat{\Delta}_+ \\ \hat{\Delta}_- \end{pmatrix} = \begin{pmatrix} \omega & 0 \\ 0 & \bar{\omega} \end{pmatrix} \begin{pmatrix} \hat{\Delta}_+ \\ \hat{\Delta}_- \end{pmatrix}, \qquad C_6 \begin{pmatrix} \hat{\Delta}_+ \\ \hat{\Delta}_- \end{pmatrix} = \begin{pmatrix} -\bar{\omega} & 0 \\ 0 & -\omega \end{pmatrix} \begin{pmatrix} \hat{\Delta}_+ \\ \hat{\Delta}_- \end{pmatrix},$$

$$\sigma_d \begin{pmatrix} \hat{\Delta}_+ \\ \hat{\Delta}_- \end{pmatrix} = \begin{pmatrix} 0 & 1 \\ 1 & 0 \end{pmatrix} \begin{pmatrix} \hat{\Delta}_+ \\ \hat{\Delta}_- \end{pmatrix}, \qquad \sigma_v \begin{pmatrix} \hat{\Delta}_+ \\ \hat{\Delta}_- \end{pmatrix} = \begin{pmatrix} 0 & -\omega \\ -\bar{\omega} & 0 \end{pmatrix} \begin{pmatrix} \hat{\Delta}_+ \\ \hat{\Delta}_- \end{pmatrix}. \tag{3.6}$$

The traces of the 2×2 matrices of Eq. 3.6 are equal to the characters of the E_1 representation of C_{6v} and this means $\hat{\Delta}_{p+ip}$ and $\hat{\Delta}_{p-ip}$ are two well-defined order parameters associated to E_1. All the order parameters that we can define for the hexagonal structure using the pairing operators, were defined in equation 3.2, are listed in Table 3.3 [31] and are shematicly shown in Fig. 3.2.

Note that the irreps A_2 and B_1 do not exist in this six-dimensional space of pairing operators. Representations E_1 and E_2 are two dimensional, and we illustrate only one of their components on Fig. 3.2. Two-dimensional irreducible representations make it posible to define complex combinations of pairing operators, $d \pm id$ and $p \pm ip$, expressed in the last four rows of Table 3.3 and are called chiral representations.

3.2 Superconductivity in twisted bilayer graphene

We studied the different kinds of bilayer graphene in chapter 1, where we used tight-binding and continuum models to describe the band structure of these systems. For TBG at some particular rotation angles (called "magic") we saw a remarkable property in
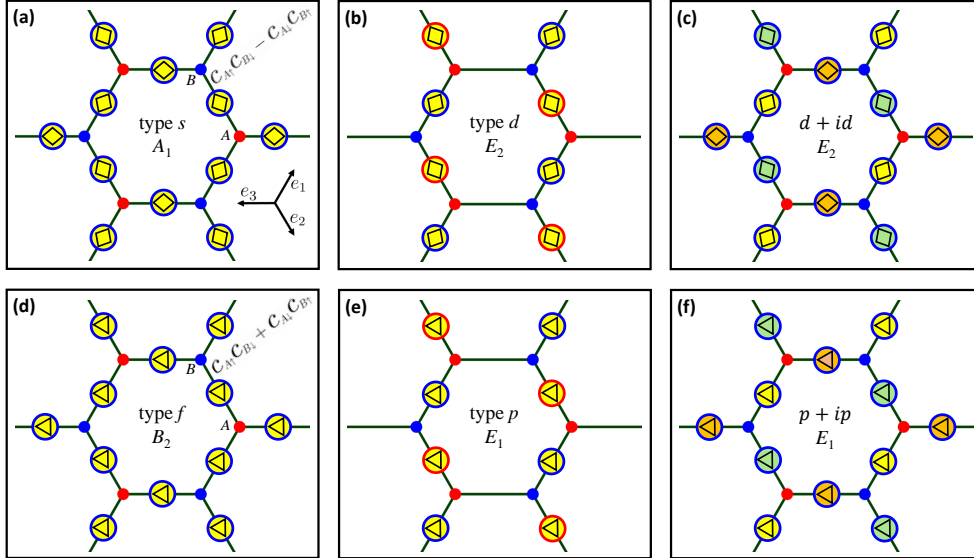
Figure 3.2
Real space representation of singlet and triplet pairing operators listed in Table 3.3. Blue and red circles indicate positive and negative sign of the pairing operators. The color is used for the phase factor, yellow, green and brown indicate the phase is equal to zero, $2\pi/3$ and $-2\pi/3$ respectively.

the band structure: the energy bands around the charge neutrality point become flat and are separated from other bands by an energy gap. The flat bands imply that the kinetic energy of electrons in these bands is small and therefore the system is a strongly correlated. Strong correlations between electrons lead to some amazing behaviours like superconductivity or Mott insulators. The correlated electrons are in the flat bands and since these flat bands are separeted from other energy bands, it is possible to define an effective model to describe the system around the charge neutrality point. In the following I will describe the effective model proposed by Kang and Vafek [40], itself based on the microscopic analysis of Moon and Koshino [67]. We then simply add a Hubbard U, local to each of the four Wannier states per unit cell, and apply cluster methods (CDMFT and VCA) to this interacting model in order to probe specic superconducting states and other correlated phases.

3.2.1 Effective model for magic angle TBG

The effective model introduced by Kang and Vafek is a low-energy, tight-binding model based on a few symmetry-adapted, maximally localized Wannier states to describe the four narrow bands of twisted bilayer graphene. This model is built for a TBG system when the twist angle is commensurate and close to one of the magic values.

For a commensurate twist angle the system has a periodic moiré pattern with a

62

triangular superlattice; see, e.g., Ref. [66]. For such a structure the size of a super unit cell relates to the twist angle. When the twist angle is small, the super unit cell is very big and contains a large number of carbon atoms. Consequently, the first Brillouin zone of the moiré structure (MBZ) is much smaller than the graphene Brillouin zone.

Due to the significant interlayer tunneling, the low-energy band structure of twisted bilayer graphene is remarkably different from that in two isolated monolayers. For a twist angle close to the magic values, the bandwidth becomes very narrow (but nonzero), the Fermi velocity vanishes at the Dirac points , and the quadratic band touching points can be seen at the corners of the MBZ [19]. To produce the above-mentioned four band effective model we have to find the spatial structure of the Wannier orbitals and also determine where is the best place to locate them in the moiré structure. The space group and time-reversal symmetries are used to answer these questions.

While the triangular moiré lattice sites have the highest local charge density at quarter filling [19], it is impossible to recover the fundamental features of the narrow-band structure unless the Wannier states (WSs) are located at the dual honeycomb lattice sites [110, 80]. We will prove this statement using symmetry considerations. Furthermore, we can compare the band structure obtained from the effective model with the result of a microscopic tight-binding model proposed by Moon and Koshino that contains a large number of atoms in the unit cell [67]. This comparison is a good criterion to confirm the validity of the effective model. The initial ansatz for localized WSs in Hilbert space is constructed based on the Bloch states at the MBZ center [63]. These initial ansatz is then used in the iterative procedure of Marzari and Vanderbilt [63] to construct maximally localized and symmetry adapted WSs [91]. Afterward the constructed WSs are used to develop and compare the low-energy tight-binding models.

Several theories have been proposed to study the insulating and superconducting phases [108, 89, 38, 79]. The closest to the four band model that we used in this work (I will call it the Vafek model) are defined in Refs. [110, 80]. However, there are important differences. In the model of Ref. [80], the valley symmetry and its spontaneous breaking play an important role. According to their assertion, the valley symmetry, together with the product of C_2 and time reversal, is an obstruction to building a four bands tight-binding model [80]. In the Vafek model, they use only the three-fold rotation around the axis across the AA stacked carbon atoms (C_3), the two-fold rotation which exchanges top and bottom layers (C_2'), and time-reversal symmetry [see Fig. 3.3(a)]. These considerations lead to the same group representations of the Bloch states at the high-symmetry MBZ points as assumed in Ref. [110]. This reference did not explicitly construct the WSs, but the WS symmetry was deduced in an insightful manner and is in agreement with the Vafek model. The three-peak structure of the WSs were found explicitly in Vafek model [see Fig. 3.4(c)] and was also recognized in Ref. [80] and dubbed the fidget spinner.

The point group symmetry operations (C_3 and C_2') form the D_3 group. This symmetry group results in nontrivial representations of Bloch states at high symmetry points of the MBZ, especially at $\mathbf{\Gamma}$ ($\mathbf{k} = 0$) and $\mathbf{K}$ ($\mathbf{k} = [(4\pi)/(3\mathbf{L}_1^2)]\mathbf{L}_1$).

Kang and Vafek calculated the band structure of the system based on the microscopic model of Ref. [67], which is a tight-binding model including both intralayer and interlayer carbon-carbon tunneling amplitudes. Their tight-binding Hamiltonian is written as

$$H = -\sum_{\mathbf{r}_i, \mathbf{r}_j} t(\mathbf{r}_i - \mathbf{r}_j) c_{\mathbf{r}_i}^\dagger c_{\mathbf{r}_j} \quad \text{with}$$

$$t(\mathbf{d}) = -V_{pp\pi}\left[1 - \left(\frac{\mathbf{d} \cdot \mathbf{e}_z}{d}\right)^2\right] - V_{pp\sigma}\left(\frac{\mathbf{d} \cdot \mathbf{e}_z}{d}\right)^2,$$

$$V_{pp\pi} = V_{pp\pi}^0 \exp\left(-\frac{d - a_0}{\delta}\right),$$

$$V_{pp\sigma} = V_{pp\sigma}^0 \exp\left(-\frac{d - d_0}{\delta}\right), \tag{3.7}$$

where $c_{\mathbf{r}_i}$ and $c_{\mathbf{r}_i}^\dagger$ are the annihilation and creation operators of the electron at the carbon site $\mathbf{r}_i$. Hopping amplitudes in π and σ bonds are set to $V_{pp\pi}^0 = -2.7$ eV, $V_{pp\sigma}^0 = 0.48$ eV. $a_0 = 0.142$ nm is the distance between two carbon atoms on a layer that are nearest to each other and $d_0 = 0.335$ nm is the interlayer distance. $\delta = 0.319\, a_0$ is the decay length for the hopping. hopping between orbitals that are apart by $d > 4a_0$ is exponentially small and neglected in the model. These detailed parameters are all taken from Ref.[67] and listed here for completeness. $\mathbf{\Gamma}$, $\mathbf{K}$, and $\mathbf{K}'$ are three high-symmetry points of the MBZ. Time-reversal transforms $\mathbf{K}$ and $\mathbf{K}'$ into each other but leaves $\mathbf{\Gamma}$ invariant.

Figure 3.3(c) illustrates that this model has four narrow bands with very small bandwidths around the charge neutrality point where the zero of energy is defined. The twist angle is important to determine whether there is an energy gap separating these narrow bands from the other bands of the spectrum. When $m - n = \pm 1$ mod 3 [66] at the $\mathbf{K}$ point, two bands make a Dirac cone, but a tiny gap ($< 0.01\ meV$) separates the two remaining bands. As a result these four Bloch states at the edge points of the MBZ form a two-dimensional representation (E) and two one-dimensional representations (A_1 and A_2) of the group D_3 [110].

The Bloch states are doubly degenerate at the center of the MBZ ($\mathbf{\Gamma}$) and the (narrow) bandwidth is defined as the energy difference between these two pairs. These doublets are the two-dimensional representations (E) of the group D_3 [110]. Two components of each doublet are chosen to be the eigenstates of C_3 with the eigenvalues equal to ϵ or ϵ^* (ϵ is a phase factor equal to $\epsilon = \exp(i2\pi/3)$). So the Bloch states at the $\mathbf{\Gamma}$ point are labeled $\Psi_{\mathbf{\Gamma}, E_\pm, \epsilon^{\pm 1}}$. Here, $E_\pm$ is used to specify the doublet with higher and lower energy, and $\epsilon^{\pm 1}$ refers to the components of each doublet which has different eigenvalues (ϵ and ϵ^*) under C_3. While the two components of each doublet are the eigenstates of C_3, they transform into each other under C_2' and the TRS. It is important to note that there is no simple transformation which relates the two doublets at different energy, i.e., $\Psi_{\mathbf{\Gamma}, E_\pm}$. This fact can be seen in Figs. 3.4(a) and 3.4(b) where $|\Psi_{\mathbf{\Gamma}, E_\pm}|^2$ is plotted.
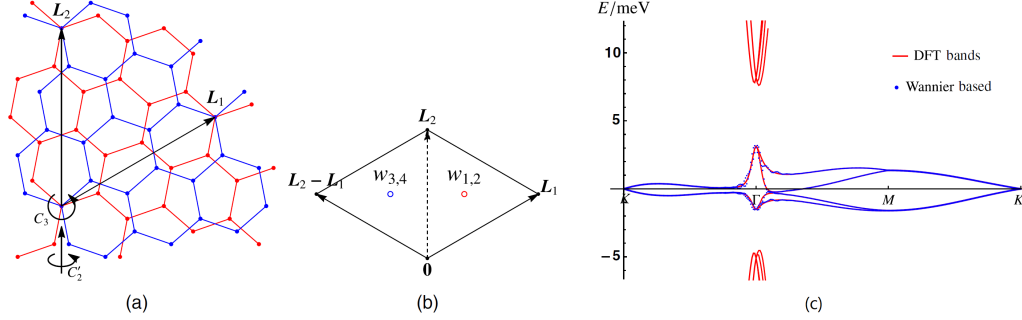
Figure 3.3

(a) The superlattice of twisted bilayer graphene. Blue and red colors refer to the bottom and top graphene layers. For the commensurate twisted angle we have a triangular super-lattice. The plot shows the super-lattice when $m = 2$ and $n = 1$. (b) Position of the local Wannier states. Black dots are the sites of the triangular super-lattice. Red and blue dots are two nonequivalent Wyckoff sites, where the local Wannier states are centered. In our effective model, w_1 and w_2 are placed at one Wyckoff position, and w_3 and w_4 are placed at the other position. Note that the Wyckoff sites form an emergent honeycomb lattice. (c) Red dots: Four narrow bands obtained from the microscopic tight-binding model given in Ref. [67] with a twist angle equal to 1.30°. Blue dots: The interpolated band structure by the effective model. This gure is taken from[40]

.

The next step is to apply the projection method to construct the localized WSs [63]. To do this, four narrow bands should be separated from all others by a gap. To satisfy this condition the twist angle is selected to be $\theta = 1.30°$ ($m = 25$ and $n = 26$ in moiré equation), which guarantees that the four narrow bands are separated by a gap on both sides. The twist angle, $\theta = 1.30°$, is a bit different from the magic angle but it is sensible to suppose the hopping parameters of the low-energy Hamiltonian to be almost the same for both of them. The confirmation of this assumption is the existence of the quadratic band touching at **K**, which can be taken as a definition of the magic angle.

Symmetry of the Wannier states

Both the shape and the position of the Wannier states are important in constructing the effective model. In a simple approach, it is possible to place the centers of all four states on the triangular moiré superlattice sites. So the WSs will be transformed as

$$g|w_{i,\mathbf{R}}\rangle = \sum_{j} |w_{j,g\mathbf{R}}\rangle U_{ji}(g) \tag{3.8}$$

where $i, j = 1, \cdots, 4$ are the indices of the WSs, $\mathbf{R}$ is the lattice vector associated to the triangular superlattice site, and g is the symmetry operation.

For the Bloch state $\Psi_{i,\mathbf{k}}$ which is a linear superposition of the WSs, the transformation
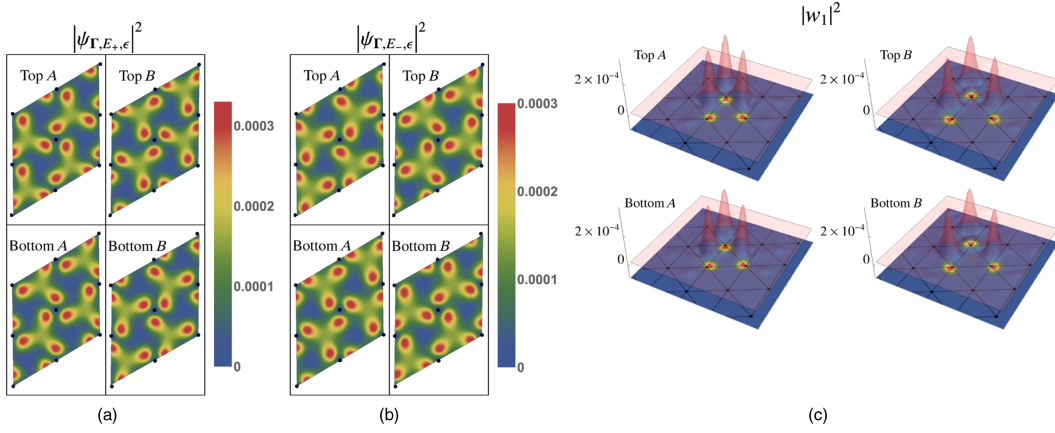
Figure 3.4

(a),(b) The square of the magnitude of the Bloch states $|\Psi_{\Gamma,E_+,\epsilon}|^2$ and $|\Psi_{\Gamma,E_-,\epsilon}|^2$ (c) The localization of the WSs based on the projection method. The four panels show $|w_1|^2$ at different layers and sublattices (layer and sublattice are labeled over the figure). This gure is taken from Ref. [40].

equation under the same symmetry operation is

$$g|\Psi_{i,\mathbf{k}}\rangle = g\sum_{\mathbf{R}} e^{i\mathbf{k}\cdot\mathbf{R}}|w_{i,\mathbf{R}}\rangle = \sum_{\mathbf{R}} e^{i\mathbf{k}\cdot\mathbf{R}}|w_{j,g\mathbf{R}}\rangle U_{ji}(g)$$
$$= \sum_{\mathbf{R}} e^{ig\mathbf{k}\cdot g\mathbf{R}}|w_{j,g\mathbf{R}}\rangle U_{ji}(g) = |\Psi_{j,g\mathbf{k}}\rangle U_{ji}(g). \tag{3.9}$$

It is interesting to discuss how the Bloch states transform at the high symmetry points of the MBZ, i.e., $\mathbf{\Gamma}$ and $\mathbf{K}$. Eq. (3.9) expresses that the Bloch states should transform as $U(g)$; this means the Bloch states at $\mathbf{\Gamma}$ and $\mathbf{K}$ should transform in the same way. But it is in conflict with the symmetry consideration of Bloch states.

As we pointed out previously, the four Bloch states transform as two doublets at $\mathbf{\Gamma}$ and one doublet and two singlets at $\mathbf{K}$. This contradiction confirms that the symmetry of the Bloch states can not be reproduced by putting all the WSs at triangular superlattice sites. A thoughtful suggestion to solve this conflict is to divide the four WSs into two groups and to place them at the centers of the equilateral triangle which make the superlattice unit cells (Wyckoff positions) [see Fig. 3.3(b)]. These centeral points of triangles form the dual honeycomb lattice [110, 80]. Thus, there should be two WSs at each site of this honeycomb lattice. Note that each super-unit-cell of the system contains two honeycomb lattice sites, and as a result w_1 and w_2 should be placed at one site and w_3 and w_4 at another site.

To demonstrate that this arrangement satisfies the symmetry consideration of the Wannier states, we start by modifying Eq. (3.8) for the dual honeycomb lattice [91],

$$g|w_{i,\mathbf{R}}\rangle = \sum_{j} |w_{j,g\mathbf{R}+\mathbf{R}'(g,i)}\rangle U_{ji}(g) \tag{3.10}$$

66

where $\mathbf{R}$ and $\mathbf{R}'$ are still the triangular super-lattice translation vectors, and the latter depends only on g and the WS index i. Equation (3.9) now takes the form [91]

$$g|\Psi_{i,\mathbf{k}}\rangle = |\Psi_{j,g\mathbf{k}}\rangle e^{-ig\mathbf{k}\cdot\mathbf{R}'}U_{ji}(g). \tag{3.11}$$

Note that the modified transformation creates an extra phase factor $e^{-ig\mathbf{k}\cdot\mathbf{R}'}$ and differentiates between $\boldsymbol{\Gamma}$ and $\mathbf{K}$. For $g = C_3$ and $\mathbf{k} = \boldsymbol{\Gamma}$, the transformation matrix U must be diagonal; in other words, all the WSs should be eigenstates of C_3 because of lattice symmetries. The Wannier orbitals $w_{1,4}$ and $w_{2,3}$ are choosen to have the eigenvalues ϵ and ϵ^*, respectively. About the second symmetry operation, since C_2' interchanges the two nonequivalent Wyckoff positions, we can set $C_2'w_1 = w_3$ and $C_2'w_2 = w_4$; see Fig. 3.3(b). Finally, time reversal does not change the position of the WSs, but it conjugates the eigenvalue of C_3. Therefore, $\mathcal{T}w_1 = w_2$ and $\mathcal{T}w_3 = w_4$. These transformation rules, together with translation symmetry, should be considered in making any low-energy model.

Symmetry considerations helped us to determine the location of the Wannier orbitals. The next step is to calculate these orbitals and also the hopping amplitudes between them. The projection method is used for this. In this method it is crucial to choose the appropriate initial trial states as input. Figs 3.4(a) and 3.4(b) show that the magnitudes of the Bloch states at the high symmetry Γ point have a smooth structure in real space when separated according to layers and sublattice. This observation is an important guide to find a good initial ansatz for w_1.

Figure 3.4(c) shows the result of the projection method for $|w_1|^2$ on different layers and sublattices. A precise look at w_1 reveals it to be closely localized and centered around the dual honeycomb lattice sites; it also displays three distinct peaks toward the triangular lattice sites. This shape of the Wannier orbitals is consistent with the results of Ref. [18], where the authors found the local density of states using density-functional theory (DFT) and proved it peaks around the triangular lattice sites. Note that all the WSs obtained in this way are related by the above-mentioned symmetry: $w_2 = w_1^*$, $w_3 = C_2'w_1$, and $w_4 = w_3^*$.

After determination of the WSs and hopping values between them in different neighbourhood, which is done in Ref. [40], it is easy to make a tight binding model and compute the band structure. The special structure of WSs demonstrated in Fig. 3.4(c) shows that the overlap between them are cosiderable in large neighbourhood, which leads to a sizable hopping amplitude between orbitals even for third neighbors and thus we cannot neglect them even in a minimal model.

The most general tight-binding Hamiltonian of the system is,

$$H = \sum_{\mathbf{R},\mathbf{r}} \sum_{i,j=1}^{4} t_{ij,\mathbf{r}} f_{i,\mathbf{R}}^{\dagger} f_{j,\mathbf{R}+\mathbf{r}}, \tag{3.12}$$

where both $\mathbf{R}$ and $\mathbf{r}$ are the triangular super-lattice vectors. The hopping amplitude t are indexed by two WS indices i and j, and the lattice vector $\mathbf{r}$.
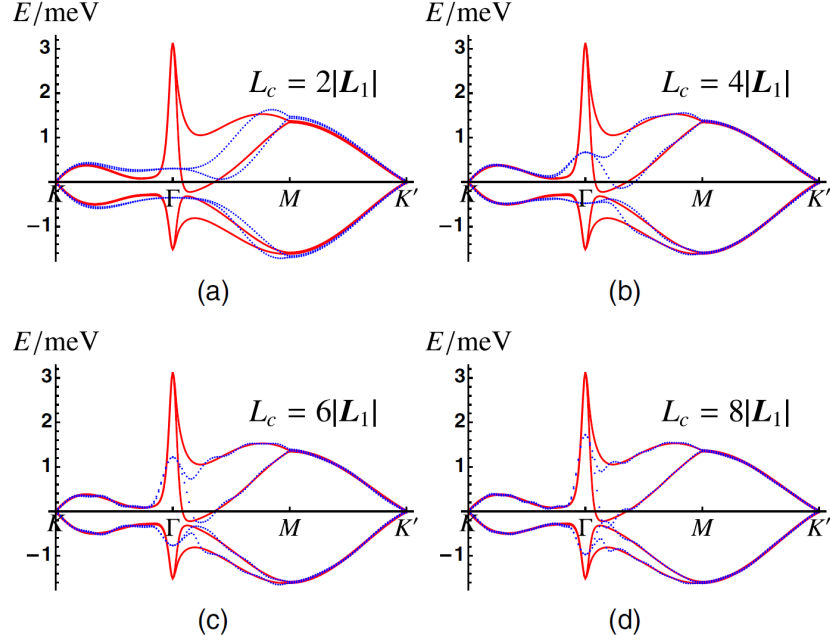
Figure 3.5
Comparison of the narrow-band structure constructed by the microscopic model expressed in Ref. [67] (red solid line) and the tight-binding model based on the Wannier orbitals (blue dots) with the range of hopping (a) $L_c = 2L$, (b) $L_c = 4L$, (c) $L_c = 6L$, and (d) $L_c = 8L$ (L is the moiré wavelengh). This gure is taken from Ref. [40].

Figure 3.5 illustrates the comparison of the narrow bands obtained using two different methods. The red solid curves are computed from the microscopic model of Ref. [67] and the blue dots show the result of the tight-binding model based on the localized WSs. The tight-binding computation is done at different hopping ranges L_c. For small L_c, most features of the band structure can be reproduced by the tight-binding model (it is in agrement with the microscopic model result), but the peaks and troughs are a bit different around Γ. By increasing the hopping range the two results become closer to each other.

3.2.2 Pairing symmetries in twisted bilayer graphene

The lattice structure proposed for the effective model for magic-angle TBG is a hexagonal lattice. Each site of this lattice, which in principle is a AB point of the moiré structure, contains two Wannier orbitals and therefore this model is based on four Wannier orbitals per unit cell, with maximal symmetry on an effective honeycomb lattice and is appropriate for a twist angle $\theta = 1.30°$.
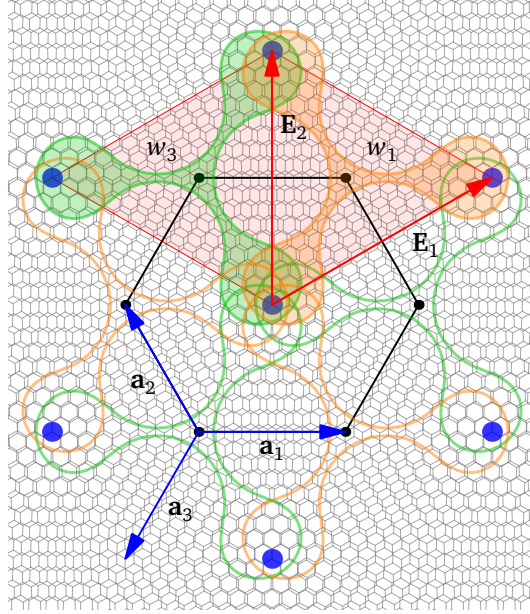
Figure 3.6
Schematic representation of the Wannier functions $w_1 = w_2^*$ (orange) and $w_3 = w_4^*$ (green) on which our model Hamiltonian is built. The charge is maximal at the AA superposition points (blue circles) forming a triangular lattice. The Wannier functions are centered on the triangular plaquettes that form a graphene-like lattice (black dots), whose unit cell is shaded in red. The underlying moiré pattern illustrated corresponds to $(m, n) = (9, 8)$, but the functions used in this work correspond to $(m, n) = (26, 25)$. The basis vectors $\mathbf{E}_{1,2}$ of the moiré lattice are shown (they are also basis vectors of the graphene-like lattice of Wannier functions), as well as the elementary nearest-neighbor vectors $\mathbf{a}_{1,2,3}$.

It is customary to derive effective models for TBG directly from continuum models. In that framework a valley symmetry emerges and the model is endowed with a fragile topology. It can be shown that in a model with nontrivial topology, time-reversal symmetry (TRS) cannot be represented simply by a set of localized Wannier states: its action is not strictly local [80]. However, as shown in [106], the error committed by using a localized Wannier basis is exponentially small. Since we are going to truncate the hopping matrix to a few terms and introduce strong interactions that would likely destroy any existing topology, this issue should not be of concern here.

Fig. 3.6 offers a schematic view of the orbitals w_1 and w_3. Orbitals $w_2 = w_1^*$ and $w_4 = w_3^*$ are not shown. Ref. [40] computes a large number of hopping integrals, of which we will only retain the largest, as listed in Table 3.4. The notation used is that of Ref. [40].

Remarkably, the most important hopping terms are between w_1 and w_4 (and between w_2 and w_3), i.e., between graphene sublattices. It therefore makes sense physically to picture the system as made of two *layers* and to assign w_1 and w_4 to the first layer, whereas w_2 and w_3 are assigned to the second layer. The rather small $t_{13}[0, 0]$

symbol	value (meV)
$t_{13}[0,0] = \omega t_{13}[1,-1] = \omega^* t_{13}[1,0]$	-0.011
• $t_{14}[0,0] = t_{14}[1,0] = t_{14}[1,-1]$	$0.0177 + 0.291i$
• $t_{14}[2,-1] = t_{14}[0,1] = t_{14}[0,-1]$	$-0.1141 - 0.3479i$
• $t_{14}[-1,0] = t_{14}[-1,1] = t_{14}[1,-2]$	
$= t_{14}[1,1] = t_{14}[2,-2] = t_{14}[2,0]$	$0.0464 - 0.0831i$

Table 3.4

Hopping amplitudes used in this work. They are the most important amplitudes computed in Ref. [40]. Here $\omega = e^{2\pi i/3}$ and the vector $[a,b]$ following the symbol represents the bond vectors in the $(\mathbf{E}_1, \mathbf{E}_2)$ basis shown on Fig.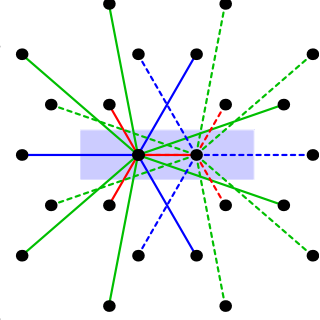 3.6. Note that $t_{23} = t_{14}^*$ and $t_{24} = t_{13}^*$. On the right: schematic view of the hopping terms t_{14} within a given layer (the unit cell is the blue shaded area). Lines 2, 3, and 4 of the table correspond to the red, blue and green links, respectively. Dashed and full lines are for t_{14} and t_{23}, respectively.

hopping (and its equivalents) is the only term that couples the two layers. The concept of layer is useful when visualizing the model in space and when arranging local clusters of sites in CDMFT, since it is preferable to have the more important hopping terms within a cluster; it is merely a book-keeping device. Fig. 3.7 illustrates a 3D representation of Wannier orbitals, where blue and red zigzag lines show the interlayer hopping terms and the yellow rhombuses are used to show the singlet pairing operators in two layers.

To this tight-binding model we will add a local interaction term U. This is a rather approximate description of the interactions in this system, but has the merit of simplicity and tractability in the context of dynamical mean field theory. A more refined description of the interactions would not only contain extended interactions (see, e.g., [26, 108]) but would include terms not of the density-density form [41]. The values of U in our calculations range from 0.5 meV to 5 meV. Fig. 3d of Ref. [18] leads us to expect a wide range of values of U depending on twist angle, and a rather large $U \sim 20$ meV at an angle of $1.30°$. However, Ref. [35] predicts a value $U \sim 5$ meV for this angle and the range of U values predicted in Fig. 9 of Ref. [103] is largely compatible with the range we have selected.

The model is invariant under a rotation C_3 by $2\pi/3$ about the AA site, and under a π-rotation C_2' about an axis in the plane of the bilayer (see Fig. 3.7). These transformations generate the point group D_3 and affect the Wannier orbitals as follows [40]:

$$
\begin{aligned}
C_3 &: w_1(\mathbf{r}) \to \omega w_1(C_3 \mathbf{r}) & C_3 &: w_4(\mathbf{r}) \to \omega w_4(C_3 \mathbf{r}) \\
C_3 &: w_2(\mathbf{r}) \to \bar{\omega} w_2(C_3 \mathbf{r}) & C_3 &: w_3(\mathbf{r}) \to \bar{\omega} w_3(C_3 \mathbf{r}) \\
C_2' &: w_1(\mathbf{r}) \to w_3(C_2' \mathbf{r}) & C_2' &: w_2(\mathbf{r}) \to w_4(C_2' \mathbf{r}) & (3.13)
\end{aligned}
$$

where $\omega = e^{2\pi i/3}$ and $\bar{\omega} = e^{-2\pi i/3}$. In other words, the orbitals w_1 and w_3 transform
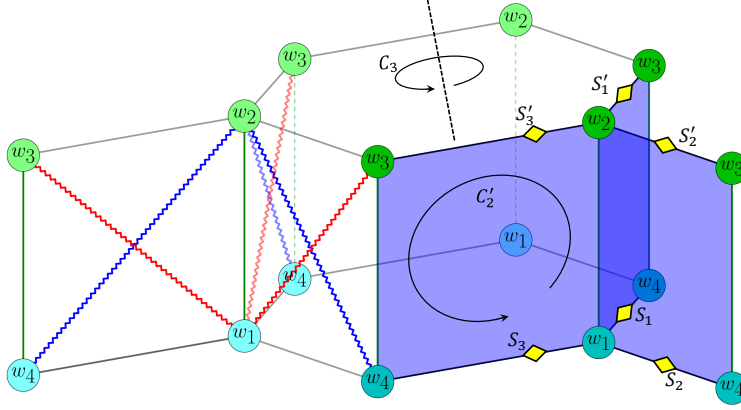
Figure 3.7
3D representation of Wannier orbitals. Blue and red zigzag lines show the interlayer hopping terms and the yellow rhombuses are used to show the singlet pairing operators in two layers. C_3 and C'_2 illustrate two rotational symmetry operators of the system.

between themselves, and so do w_2 and w_4. The model also has time-reversal symmetry (TRS), under which $w_1 \leftrightarrow w_2$ and $w_3 \leftrightarrow w_4$.

Possible superconducting pairings are either singlet or triplet (there is no spin orbit coupling). Let us therefore concentrate on pairing states involving nearest neighbors on a given layer, i.e., between orbitals w_1 and w_4 (or w_2 and w_3). Because of the strong local repulsion in our model, we ignore on-site pairing. Let us then recall the pairing operators that we can define in each layer (see Eq. 3.1)

$$S_{i,\mathbf{r}} = c_{\mathbf{r},\uparrow} c_{\mathbf{r}+\mathbf{a}_i,\downarrow} - c_{\mathbf{r},\downarrow} c_{\mathbf{r}+\mathbf{a}_i,\uparrow} \qquad \text{(singlet)}$$
$$T_{i,\mathbf{r}} = c_{\mathbf{r},\uparrow} c_{\mathbf{r}+\mathbf{a}_i,\downarrow} + c_{\mathbf{r},\downarrow} c_{\mathbf{r}+\mathbf{a}_i,\uparrow} \qquad \text{(triplet)} \qquad (3.14)$$

where $c_{\mathbf{r},\sigma}$ annihilates an electron at graphene site $\mathbf{r}$ of the first layer (in orbital w_1 or w_4 depending on the sublattice). The elementary vectors $\mathbf{a}_i$ are defined on Fig. 3.6, but apply to the layer in the current context. Likewise, we define operators $S'_{i,\mathbf{r}}$ and $T'_{i,\mathbf{r}}$ on the second layer, in terms of orbitals w_2 and w_3. Under the transformations C_3 and C'_2, the six singlet pairing operators transform amongst themselves,

$$C_3[S_1, S_2, S_3] = [S_3, S_1, S_2], \qquad C'_2[S_1, S_2, S_3] = [S'_2, S'_1, S'_3],$$
$$C_3[S'_1, S'_2, S'_3] = [S'_3, S'_1, S'_2], \qquad C'_2[S'_1, S'_2, S'_3] = [S_2, S_1, S_3], \qquad (3.15)$$

likewise for the triplet pairing operatores we have,

$$C_3[T_1, T_2, T_3] = [T_3, T_1, T_2], \qquad C'_2[T_1, T_2, T_3] = [-T'_2, -T'_1, -T'_3],$$
$$C_3[T'_1, T'_2, T'_3] = [T'_3, T'_1, T'_2], \qquad C'_2[T'_1, T'_2, T'_3] = [-T_2, -T_1, -T_3]. \qquad (3.16)$$

71

It customary to combine these pairing operatores to make symmetry adapted order parameters for the two layers. As we prove in section 3.1 these operators, for the first layer, could be written as

$$\text{Singlet operators} \qquad\qquad \text{Triplet operators}$$

$$s = \sum_{\mathbf{r}}\left(S_{1,\mathbf{r}} + S_{2,\mathbf{r}} + S_{3,\mathbf{r}}\right) \qquad\qquad f = \sum_{\mathbf{r}}\left(T_{1,\mathbf{r}} + T_{2,\mathbf{r}} + T_{3,\mathbf{r}}\right) \qquad (3.17a)$$

$$d_1 = \sum_{\mathbf{r}}\left(S_{1,\mathbf{r}} - S_{2,\mathbf{r}}\right) \qquad\qquad p_1 = \sum_{\mathbf{r}}\left(T_{1,\mathbf{r}} - T_{2,\mathbf{r}}\right) \qquad (3.17b)$$

$$d_2 = \sum_{\mathbf{r}}\left(S_{1,\mathbf{r}} - S_{3,\mathbf{r}}\right) \qquad\qquad p_2 = \sum_{\mathbf{r}}\left(T_{1,\mathbf{r}} - T_{3,\mathbf{r}}\right) \qquad (3.17c)$$

$$d + id = \sum_{\mathbf{r}}\left(S_{1,\mathbf{r}} + \omega S_{2,\mathbf{r}} + \bar{\omega} S_{3,\mathbf{r}}\right) \qquad p + ip = \sum_{\mathbf{r}}\left(T_{1,\mathbf{r}} + \omega T_{2,\mathbf{r}} + \bar{\omega} T_{3,\mathbf{r}}\right) \quad (3.17d)$$

$$d - id = \sum_{\mathbf{r}}\left(S_{1,\mathbf{r}} + \bar{\omega} S_{2,\mathbf{r}} + \omega S_{3,\mathbf{r}}\right) \qquad p - ip = \sum_{\mathbf{r}}\left(T_{1,\mathbf{r}} + \bar{\omega} T_{2,\mathbf{r}} + \omega T_{3,\mathbf{r}}\right) \quad (3.17e)$$

and similar combinations (specified with prime symbols) for the second layer. These operators may be organized into irreducible representations of D_3, as listed on Table 3.5.

$\mathbf{D_3}$	E	$2C_3(z)$	$3C_2'$	singlet pairing	triplet pairing
A_1	1	1	1	$s + s'$	$f + f'$
A_2	1	1	-1	$s - s'$	$f - f'$
E	2	-1	0	$[d - id , \ d' + id']$	$[p - ip , \ p' + ip']$
				$[d_1 + d_1' , \ d_2 + d_2']$	$[p_1 + p_1' , \ p_2 + p_2']$

Table 3.5
Irreducible representations (irreps) of D_3 associated with the six pairing operators defined on nearest-neighbor sites, as defined in Eqs (3.17). (Un)primed operators belong to the second (first) layer.

The following simple example can help us to understand how the pairing operators of Table 3.5 were defined. The operations C_3 and C_2' act as follows on the combinations $d - id$ and $d' + id'$:

$$C_3 \begin{pmatrix} d - id \\ d' + id' \end{pmatrix} \rightarrow \underbrace{\begin{pmatrix} \bar{\omega} & 0 \\ 0 & \omega \end{pmatrix}}_{trace=-1} \begin{pmatrix} d - id \\ d' + id' \end{pmatrix}, \quad \omega + \bar{\omega} = -1,$$

$$C_2' \begin{pmatrix} d - id \\ d' + id' \end{pmatrix} \rightarrow \underbrace{\begin{pmatrix} 0 & \bar{\omega} \\ \omega & 0 \end{pmatrix}}_{trace=0} \begin{pmatrix} d - id \\ d' + id' \end{pmatrix}, \qquad (3.18)$$

the traces of these transformation matrices are equal to the characters of C_3 and C'_2 of the E representation of the D_3 character table. This means $[d - id \ , \ d' + id']$ belongs to the E representation of the character table.

A similar analysis could be carried out with longer-range pairing, with the same classication: This would simply add harmonics to the basic pairing functions.

This organization into representations of D_3 is contingent on the importance of the inter-layer hopping t_{13}, which is an order of magnitude smaller than the intra-layer hopping. If t_{13} were zero, the two layers would be independent, the symmetry would be upgraded to C_{6v} and the classification of pairing states would be the same as in Ref. [31], with representations A_1 (s), A_2 (f), E_1 ($p \pm ip$) and E_2 ($d \pm id$).

3.2.3 CDMFT for twisted bilayer graphene

In order to probe the possible existence of superconductivity in this model, we use cluster dynamical mean-field theory (CDMFT) [47, 56, 93] with an exact diagonalization solver at zero temperature (or ED-CDMFT). We have described this method in section 2.5. The main idea is to divide the original lattice into small clusters and to add to each cluster an effective medium representing the remainder of the lattice. In other words the infinite lattice is tiled into identical, repeated units; this defines a superlattice, and an associated reduced Brillouin zone, smaller than the original Brillouin zone. In the present study the unit cell of the superlattice (or supercell) is made of four clusters of four sites each: Two clusters tile each of the two layers (Fig. 3.8c). The cluster-bath system for the current problem is illustrated on Fig. 3.8. The supercell contains four 4-site clusters; one layer is illustrated on Panel (c). Note that the only hopping term included in the impurity model is $t_{14}[0,0]$ and its equivalents, represented by red lines on Fig. 3.4. The other hopping terms have an effect through the self-consistent CDMFT procedure.

Each cluster contains four sites and six bath orbitals and the various bath parameters are illustrated on panels (a) and (b) of Fig. 3.8. The four black, numbered circles are the cluster sites per se. The six red squares are the bath orbitals. Even though their positions have no meaning, they are, on this diagram, assigned a virtual position that makes them look as if they were physical sites on neighboring clusters. They are then given nearest-neighbor hybridizations $\theta_{1,2}$ and second-neighbor hybridizations $\eta_{1,2}$. In order to probe superconductivity, we add pairing amplitudes within the bath itself, as shown on Fig. 3.8b: Two pairing amplitudes $d_{1,2}$ between consecutive bath orbitals, and two others $p_{1,2}$ between second neighbor bath orbitals. Each cluster is coupled to a bath of uncorrelated, auxiliary orbitals, and is governed by an Anderson impurity model (AIM):

$$H_{\text{imp}} = H_C + \sum_{i,r} \theta_{i,r}(c_i^\dagger a_r + H.c.) + \sum_r \epsilon_r(a_r^\dagger a_r) + H_{\text{pairing}}. \tag{3.19}$$

The pairing amplitudes must be understood in the restricted Nambu formalism, in which
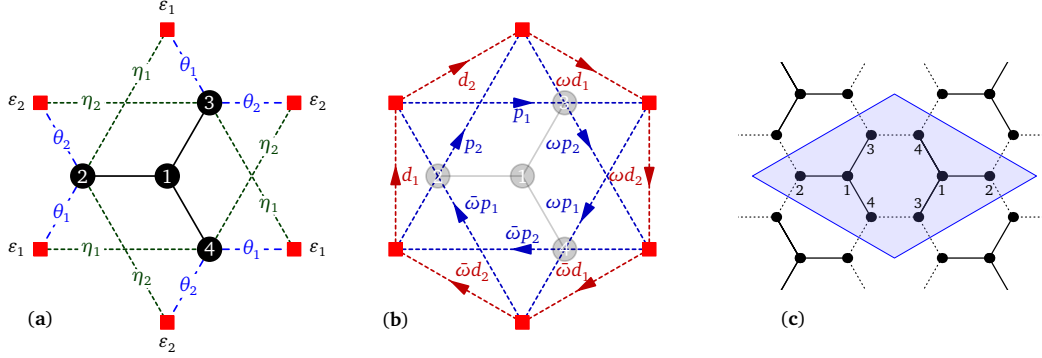
Figure 3.8
Schematic representation of the impurity model. Each cluster is made of four lattice sites (numbered black dots) and six bath orbitals (red squares). The normal-state bath parameters are shown on Panel (a): Two different bath energies $\varepsilon_{1,2}$, four different hybridizations $\theta_{1,2}$ and $\eta_{1,2}$. The anomalous bath parameters are shown on Panel (b). As shown, they are optimized for studying the $p + ip$ state: Two complex-valued triplet pairings $d_{1,2}$ between nearestneighbor bath orbitals, and two other complex-valued triplet pairings $p_{1,2}$ between second-neighbor bath orbitals, all modulated by powers of the complex amplitude $\omega = e^{2\pi i/3}$ as one goes around ($\bar{\omega} = \omega^2 = \omega^{-1}$). The unit cell of the impurity model contains four copies of this cluster: Two on the bottom level ($w_{1,3}$), two on the top level ($w_{2,4}$). On each level, they are arranged as shown on Panel (c) (the 4-site cluster on the right is the inversion of the one on the left, and the bath parameters are the same on the two clusters, except for the sign of the triplet pairings, which are inverted).

a particle-hole transformation is applied to the spin-down orbitals, giving the pairing operators the looks of hopping amplitudes. Specifically, in terms of the multiplet $(C_\uparrow, C_\downarrow^\dagger, A_\uparrow, A_\downarrow^\dagger)$, where $C_\sigma = (c_{1,\sigma}, c_{2,\sigma}, c_{3,\sigma}, c_{4,\sigma})$ and $A_\sigma = (a_{1,\sigma}, \cdots, a_{6,\sigma})(\sigma = \uparrow, \downarrow)$, the noninteracting part of the impurity Hamiltonian takes the form

$$H_{\text{imp}}^0 = \begin{pmatrix} C_\uparrow^\dagger & C_\downarrow & A_\uparrow^\dagger & A_\downarrow \end{pmatrix} \begin{pmatrix} \mathbf{T} & \boldsymbol{\Theta} \\ \boldsymbol{\Theta}^\dagger & \mathbf{E} \end{pmatrix} \begin{pmatrix} C_\uparrow \\ C_\downarrow^\dagger \\ A_\uparrow \\ A_\downarrow^\dagger \end{pmatrix} \tag{3.20}$$

where

$$\mathbf{T} = \begin{pmatrix} \mathbf{t}_c & 0 \\ 0 & -\mathbf{t}_c \end{pmatrix} \qquad \boldsymbol{\Theta} = \begin{pmatrix} \boldsymbol{\theta} & 0 \\ 0 & -\boldsymbol{\theta}^* \end{pmatrix} \qquad \mathbf{E} = \begin{pmatrix} \boldsymbol{\epsilon} & \boldsymbol{\Delta}^\dagger \\ \boldsymbol{\Delta} & -\boldsymbol{\epsilon} \end{pmatrix} \tag{3.21}$$

Here $\mathbf{t}_c$ is the hopping matrix restricted to the cluster, $\boldsymbol{\theta}$ is a 4×4 matrix containing the parameters $\theta_{1,2}$ and $\eta_{1,2}$, $\boldsymbol{\epsilon}$ is a diagonal matrix containing the bath energies $\varepsilon_{1,2}$ and $\boldsymbol{\Delta}$ is a 6×6 matrix containing the parameters $d_{1,2}$ and $p_{1,2}$.

74

In total, the AIM contains 10 bath parameters, some real, some complex. The impurity Hamiltonian does not contain pairing operators on the cluster sites themselves. However, the operators defined in Eqs (3.1) may develop a nonzero expectation value on the impurity through the self-consistent bath.

The hybridization pattern shown in the figure is appropriate for triplet pairing (it is directional, as indicated by the arrows) in a $p + ip$ state (because of the phases ω and $\omega^2 = \bar{\omega}$ appearing in the bath pairing amplitudes as one circles around). This may be readily adapted to probing a $p - ip$ state (by replacing $\omega \leftrightarrow \bar{\omega}$) or a f state (by replacing $\omega, \bar{\omega} \to 1$). Likewise, singlet states are probed by introducing singlet pairing between bath sites. In principle, we could leave all pairings free, at the price of tripling the number of bath parameters, but CDMFT convergence has proven problematic when this was tested. It is easier, and no less general, to separately probe the $p \pm ip$ and f states (and likewise for the singlet states).

One could also treat the bath parameters of all four clusters of the supercell as independent. In practice, this is not necessary as they are related. The two clusters belonging to the same layer have identical bath parameters by symmetry, except for the triplet pairings which must change sign between the two clusters because the second cluster is obtained from the first by a spatial inversion. According to Table 3.5, we expect the complex-valued bath parameters of the second layer to be the complex conjugates of those of the first layer. These constraints effectively reduce the total number of variational parameters to the equivalent of 13 real parameters.

Minimizing the distance function (2.71) is done by the Nelder-Mead or the conjugate-gradient method as implemented in SciPy. These methods do not guarantee a global minimum, but only a local one. Because of this, jumps in the bath parameters might occur as a function of an external (control) parameter like the chemical potential μ, and we would expect that this manifests itself as a hysteresis when cycling over μ. We have observed no such hysteresis in the present study. This being said, the CDMFT algorithm summarized above contains an iteration over impurity models that defines a very complex nonlinear system that rather complicates this simple expectation. Failure to converge often manifests itself by oscillations between two or more sets of bath parameters and experience shows that increasing the parameter set does not necessarily alleviate this problem.

3.3 Results and discussion

We have probed the different states listed in Table 3.5 using the above CDMFT setup. In order to reach a solution from scratch, we have used the following staged approach: (i) Owing to the small value of t_{13}, a one-layer model was first studied. (ii) An external field of each of types (3.17) was then applied to the cluster in order to induce a nonzero average pairing forcefully. This external field was then reduced to zero in a few steps, each time starting from the previous solution. (iii) Once a nontrivial solution was found in this way at zero external field, the second-layer was added (with a complex
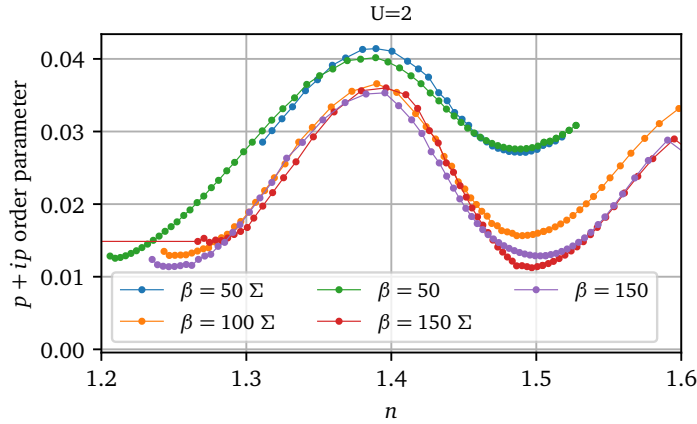
Figure 3.9
$p + ip$ order parameter found by CDMFT, as a function of electron density n, for $U = 2$ meV and several variants of the CDMFT procedure explained in the text. Only the electron-doped results ($n > 1$) are shown for clarity.

conjugated bath system, e.g., $p - ip$ instead of $p + ip$). (iv) the solution found was then scanned as a function of chemical potential within the two-layer model. The most delicate step is to find a first solution; scanning over parameters of the model (such as the chemical potential or the interaction) is easier since the solution at a given set of model parameters provides an initial trial solution for the next parameter set. Computing time varies depending on convergence rate, but is typically of the order of 10 minutes per parameter set once the scan is in motion, with code highly optimized for speed; memory needs are relatively modest at 3-4 gigabytes.[1]

We found a nonzero solution for $p \pm ip$ pairing extending over a wide range of doping. Fig. 3.9 shows the average $p + ip$ order parameter on a cluster of the first layer, as a function of electron density on the cluster, for a local repulsion $U = 2$ meV. The order parameter is the ground-state expectation value of operator (3.17d) restricted to the cluster within the impurity model. Several variants of the CDMFT procedure are illustrated, which we must now explain. The distance function (2.71) depend on a set of weights $W(i\omega_n)$ and a fictitious temperature β^{-1}. The values of β (in meV^{-1}) are indicated in the legend of Fig. 3.9. The grid of Matsubara frequencies then stops at some cutoff value taken to be $\omega_c = 2$ meV in this work. The curve labeled $\beta = 50$ (green dots) is obtained by setting all weights to the same value. The other curves (with a Σ label) are obtained by setting the weights proportional to the self-energy $|\Sigma(i\omega_n)|$ (the norm of the matrix). This is justified if one considers DMFT from the point of view

---

[1]Adding just a few orbitals to the impurity problem would dramatically increase the resources needed: Going from 6 to 9 bath orbitals, for a total of 13 orbitals in the impurity model, would increase the Hilbert space dimension 50-fold, with a corresponding increase in memory usage and an even sharper increase in computing time.
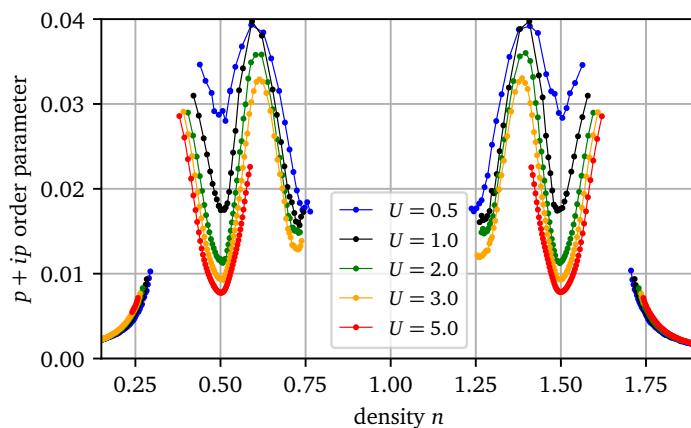
Figure 3.10
$p + ip$ order parameter found by CDMFT, as a function of electron density n, for several values of Hubbard U (in meV). The order parameter is the ground state average of the operator (3.17d), restricted to the cluster. The density n is the ground-state average occupation of the cluster. One of the clusters of the first layer was used for these averages. Clusters on the second layer would show the opposite chirality ($p - ip$).

of the Potthoff functional [84, 94]. In particular, it gives more importance to very low frequencies in an insulating state, as the self-energy then grows as $\omega \to 0$. We expect the superconducting order parameter to be minimum, if not zero, at quarter ($n = 0.5$) or three-quarter ($n = 1.5$) filling, as observed in experiments. Indeed, this commensurate filling leads to an insulating state at the magic angle $1.08°$[18] and superconductivity occurs on either side of this filling value. We see that this is not exactly the case in the data sets of Fig. 3.9, although using a higher β and, to a lesser extent, a self-energy modulated set of weights, greatly helps. We will stick to the value $\beta = 150$ and use a self-energy modulated set of weights in what follows.

Figure 3.10 shows the $p + ip$ order parameter as a function of electron density for the full range of solutions obtained, and five values of the one-site repulsion U (in meV). We note that the system is almost (but not exactly) particle-hole symmetric. Superconductivity is strongly suppressed near half-filling (CDMFT ceases to converge to a superconducting solution when $|n - 1| \lesssim 0.2$). Superconductivity is partially suppressed at quarter- and three-quarter filling ($n = 0.5, 1.5$) and this suppression increases with U. Despite a strong suppression of superconductivity at $n = 0.5$ and $n = 1.5$, a Mott state is not fully obtained there for the range of U studied. This is likely caused by our neglect of extended interactions. Note the gap in the solutions in the vicinity of $n = 0.3$ and $n = 1.7$; the solutions exist for all values of chemical potential μ around these values, but a discontinuity leads to the forbidden regions when plotted as a function of density.

We also found a weaker singlet solution with $d + id$ symmetry, as illustrated on Fig. 3.11a for $U = 2$ meV and $U = 5$ meV. The singlet solution has a smaller order
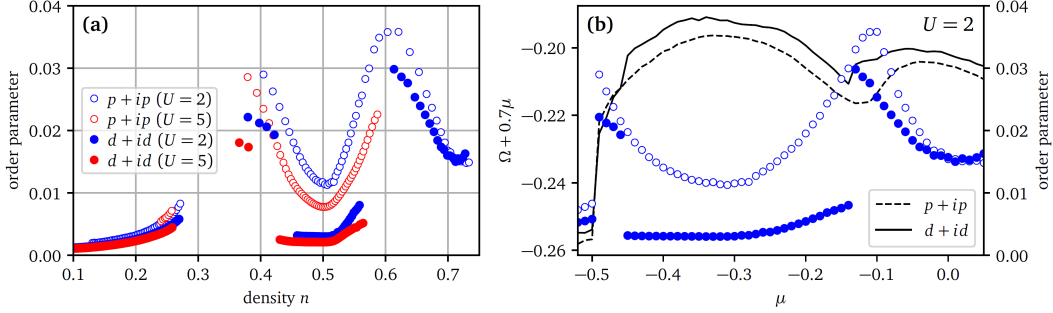
Figure 3.11
Left panel: $d+id$ order parameter found by CDMFT (filled circles), as a function of electron density n, compared with the $p+ip$ order parameter (open circles), for $U=2$ meV and $U=5$ meV. The $d+id$ order parameter is the ground state average of the operator (3.17b), restricted to the cluster. Again, clusters on the second layer would show the opposite chirality $(d-id)$. Right panel: For $U=2$ and as a function of chemical potential μ, the same chiral order parameters as in the left panel, as well as the value of the Potthoff functional Ω for each solution. The $p+ip$ solution (dashed curve) has a lower energy than the $d+id$ solution (full curve). A multiple of μ was added to Ω to rectify the curves and improve clarity.

parameter than the triplet solution, especially in the vicinity of $n=0.5$ and $n=1.5$, where it is strongly suppressed and suffers from a discontinuity (we only show the hole-doped case for clarity). A possible way to discriminate between the triplet and singlet solutions is to compare the energies of each. An optimal way to estimate the energy in CDMFT is to borrow the expression of the Potthoff self-energy functional from the variational cluster approximation [81, 84], as explained in Ref. [94]. The expression of the Potthoff functional is

$$\Omega = E_0 + \text{Tr}\ln[-(\mathbf{G}_0^{-1}-\mathbf{\Sigma})^{-1}] - \text{Tr}\ln(-\mathbf{G}_c) \qquad (3.22)$$

where E_0 is the ground state energy per site of the impurity model (including the chemical potential contribution), and the functional trace Tr represents an integral over frequencies and wave vector. It is an approximation to the grand potential $\Omega = E - \mu N$ of the system at zero temperature, given that the CDMFT is not far from the solution to Potthoff's variational principle [81]. Figure 3.11b shows the Potthoff functional of the two solutions ($p+ip$ and $d+id$) at the same time as the corresponding order parameters, as a function of chemical potential μ. The grand potential of the triplet is consistently lower than that of the singlet, except for an isolated point near a discontinuity. We have also compared directly the ground state energies E_0 of the corresponding two impurity models, and the same conclusion holds: the singlet $d+id$ solution has a higher energy, a smaller order parameter, and is thus subdominant.

We were not able to resolve the different representations of D_3, as listed on Table 3.5. In other words, the energy difference between the A_1, A_2 and E representations is likely too small to have an effect on the CDMFT convergence procedure. This is due to the

small value of the inter-layer hopping t_{13}. It is however important to assign opposite chiralities to the two layers.

The effective model used was based on the parameters of Ref. [40], appropriate for a twist angle $\theta = 1.30°$. Would our conclusions change for different, small twist angles, such as the ones found in Ref. [19] ($\theta = 1.05°$, $1.16°$)? Maybe. But a similar CDMFT of the nearest-neighbor Hubbard model on the graphene lattice has shown triplet pairing to be dominant [31]; so did a RPA study of bi-layer silicene [113], which is likewise based on the graphene lattice.

Let us compare our conclusions with some other works having found superconductivity in effective models for twisted bilyaer graphene. Ref. [34] finds triplet superconductivity as a Kohn-Luttinger instability, but is essentially a weak-coupling analysis, contrary to ours. Ref. [99] finds triplet superconductivity near $n = 0.5$, but with f symmetry, using a numerical renormalization group approach expected to be valid from weak to moderate coupling. Our strong-coupling calculations could not stabilize f-wave superconductivity. Kennes *et al.* [42] find $d + id$ superconductivity near $n = 1$ using a renormalization-group approach followed by an mean-field analysis. Zhang *et al.* [114] arrive at the same conclusion, using constrained path Monte Carlo, and so do Chen et al [21]. These three works do not contradict ours, since our prediction concerns mostly regions around $n = 0.5$ and $n = 1.5$, not $n = 1$.

A possible improvement to the present study would be to include extended interactions, for example derived from an on-site Coulomb interaction at the AA sites [26, 108]. We expect that including such interactions would hinder pairing at quarter filling. This would require adding inter-orbital interactions $U_{1,2}$ ($U_{3,4}$) between orbitals w_1 and w_2 (w_3 and w_4). Unfortunately, since orbitals w_1 and w_2 belong to different clusters in our CDMFT setup, this cannot be implemented as is. The effect could be studied within a different quantum cluster approach, such as the variational cluster approximation [84, 83, 31], which in practice allows larger clusters. Alternately, inter-cluster interaction terms could be treated at the mean field level, as done, for instance, in Refs. [98, 31]. Interactions that do not have a density-density form (and thus not diagonal in the Wannier basis) would, naturally, complicate matters.

A legitimate question is whether other broken symmetries could compete with superconductivity in the phase diagram. We expect charge order to be a serious contender at commensurate filling (in particular $n = 0.5$ and $n = 1.5$), provided extended interactions are taken into account. It is possible that the superconducting order that we found would disappear precisely at these fillings, either because of the extended interactions or out of competition with charge order. Likewise, antiferromagnetism is likely to appear at half-filling ($n = 1$), where superconductivity is suppressed, because of a suppression of the density of states related to Mott physics. We will discuss these subjects in the next chapter.

Chapter 4

Charge order and antiferromagnetism

4.1 Introduction

In this chapter, we use a modified version of the Vafek model that we introduced in the previous chapter. We will adopt this model and supplement it with local and extended interactions up to third neighbors. We will study the normal (i.e., non superconducting) states of this model at quarter- and half-lling. We use the variational cluster approximation (VCA) on a 12-site cluster, augmented by a mean-eld treatment of inter-cluster interactions. We will show that such interactions naturally lead to a pure Mott insulator at quarter-lling, without charge order, and to a pure Mott insulator at half-lling, without antiferromagnetism. This is the main conclusion of this chapter. Since the model studied is nearly particle-hole symmetric, the conclusions reached at quarter lling also apply at three-quarter lling. The material of this chapter is submitted for publication and appears on the arXiv:2112.00181v2 [74].

4.2 Low-energy model with extended interactions

A complete description of the low-energy model was given in section 3.2.1, where we discussed the symmetry of the four Wannier orbitals and also their position on the moiré lattice. Fig. 3.6 illustrates the shape and location of these orbitals. We retained the most important hopping terms between Wannier orbitals and assumed an onsite Hubbard interaction only in our effective model. We now proceed to describe a simple model for interactions, derived from a local Coulomb interaction [26, 108].

$$H_{\text{int}} = u \sum_{\mathbf{R} \in \text{AA}} n_{\mathbf{R}}^2 \qquad (4.1)$$

where the sum is carried over AA sites and $n_{\mathbf{R}}$ is the total charge located at that site, to which 12 Wannier orbitals (6 per layer) contribute. Specifically, we could write

$$n_{\mathbf{R}} = \frac{1}{3} \sum_{i=1}^{3} \left(n_{\mathbf{R}+\mathbf{a}_i}^{(1)} + n_{\mathbf{R}-\mathbf{a}_i}^{(1)} + n_{\mathbf{R}+\mathbf{a}_i}^{(2)} + n_{\mathbf{R}-\mathbf{a}_i}^{(2)} \right) \tag{4.2}$$

where $n_{\mathbf{r}}^{(\ell)}$ is the electron number associated with the Wannier orbital centered at the (honeycomb) lattice site $\mathbf{r}$ on layer ℓ. The vectors $\pm\mathbf{a}_i$, indicated on Fig. 3.6, go from each AA site to the six neighboring honeycomb lattice sites. The factor of $\frac{1}{3}$ above comes from the fact that each Wannier orbital has three lobes, i.e., is split across three AA sites.

Expressed in terms of the Wannier electron densities $n_{\mathbf{r}}^{\ell}$, the interaction takes the form

$$H_{\text{int}} = \frac{1}{2} \sum_{\mathbf{r},\mathbf{r}',\ell,\ell'} V_{\mathbf{r},\mathbf{r}'}^{\ell,\ell'} n_{\mathbf{r}}^{\ell} n_{\mathbf{r}'}^{\ell'} \tag{4.3}$$

where the factor of $\frac{1}{2}$ avoids double counting when performing independent sums over sites and orbitals. The Hubbard on-site, intra-orbital interaction U is equal to $V_{\mathbf{r},\mathbf{r}}^{\ell,\ell}$, since

$$V_{\mathbf{r},\mathbf{r}}^{\ell,\ell} n_{\mathbf{r}\uparrow}^{\ell} n_{\mathbf{r}\downarrow}^{\ell} = \frac{1}{2} V_{\mathbf{r},\mathbf{r}}^{\ell,\ell} (n_{\mathbf{r}\uparrow}^{\ell} + n_{\mathbf{r}\downarrow}^{\ell})(n_{\mathbf{r}\uparrow}^{\ell} + n_{\mathbf{r}\downarrow}^{\ell}) - \frac{1}{2} V_{\mathbf{r},\mathbf{r}}^{\ell,\ell} n_{\mathbf{r}}^{\ell} \qquad (n_{\mathbf{r}\sigma}^2 = n_{\mathbf{r}\sigma}) \tag{4.4}$$

Including on-site interactions in this form entails a compensation term $U/2$ to the chemical potential.

Careful counting from Eqs (4.1,4.2) shows that

$$
\begin{aligned}
U &= \frac{2}{3}u && \text{(on-site)} \\
V_{\mathbf{rr}}^{(1,2)} \equiv V_0 &= \frac{2}{3}u = U && \text{(same site, diff. layer)} \\
V_{\mathbf{rr}'}^{(\ell,\ell')} \equiv V_1 &= \frac{4}{9}u = \frac{2}{3}U && \text{(1st neighbors)} \\
V_{\mathbf{rr}'}^{(\ell,\ell')} \equiv V_2 &= \frac{2}{9}u = \frac{1}{3}U && \text{(2nd neighbors)} \\
V_{\mathbf{rr}'}^{(\ell,\ell')} \equiv V_3 &= \frac{2}{9}u = \frac{1}{3}U && \text{(3rd neighbors)}
\end{aligned}
\tag{4.5}
$$

There are no interactions beyond third neighbors coming from a single AA site. We will study this model by assuming the above relations between extended interactions $V_{0,1,2,3}$ and the on-site interaction U.

4.2.1 The strong-coupling limit

Given the large number of extended interactions in the model, it is instructive to look at the strong-coupling limit (neglecting all hopping terms) to detect possible charge order instabilities stemming solely from the interactions.

The reader will forgive us if we use a slightly different notation, writing the interaction Hamiltonian as

$$H_{\text{int}} = \frac{1}{2} \sum_{\mathbf{R},\mathbf{R}',a,b} V_{\mathbf{R},\mathbf{R}'}^{a,b} n_{\mathbf{R}}^a n_{\mathbf{R}'}^b \tag{4.6}$$

where now $\mathbf{R}$, $\mathbf{R}'$ denote Bravais lattice sites and a, b orbital indices from 1 to 4. In essence, for each $\mathbf{R}$, the site index $\mathbf{r}$ takes two values (the two sublattices A and B), as does the layer index ℓ, leading to four possible value of the orbital index a. This shift in notation allows us to express the interaction in Fourier space:

$$H_{\text{int}} = \frac{1}{2} \sum_{\mathbf{q}} \tilde{V}_{\mathbf{q}}^{ab} \tilde{n}_{\mathbf{q}}^{a\dagger} \tilde{n}_{\mathbf{q}}^b \tag{4.7}$$

where

$$V_{\mathbf{R}\mathbf{R}'}^{ab} = \frac{1}{L} \sum_{\mathbf{q}} \tilde{V}_{\mathbf{q}}^{ab} e^{i\mathbf{q}\cdot(\mathbf{R}-\mathbf{R}')} \qquad \tilde{n}_{\mathbf{q}}^a = \frac{1}{\sqrt{L}} \sum_{\mathbf{R}} e^{-i\mathbf{q}\cdot\mathbf{R}} n_{\mathbf{R}}^a \tag{4.8}$$

Interactions up to third neighbor are then encoded in the following $\mathbf{q}$-dependent matrix:

$$[\tilde{V}_{\mathbf{q}}^{ab}] = \begin{pmatrix} U + V_2\beta_{\mathbf{q}} & V_1\gamma_{\mathbf{q}} + V_3\gamma_{2\mathbf{q}}^* & V_0 + V_2\beta_{\mathbf{q}} & V_1\gamma_{\mathbf{q}} + V_3\gamma_{2\mathbf{q}}^* \\ V_1\gamma_{\mathbf{q}}^* + V_3\gamma_{2\mathbf{q}} & U + V_2\beta_{\mathbf{q}} & V_1\gamma_{\mathbf{q}} + V_3\gamma_{2\mathbf{q}}^* & V_0 + V_2\beta_{\mathbf{q}} \\ V_0 + V_2\beta_{\mathbf{q}} & V_1\gamma_{\mathbf{q}}^* + V_3\gamma_{2\mathbf{q}} & U + V_2\beta_{\mathbf{q}} & V_1\gamma_{\mathbf{q}} + V_3\gamma_{2\mathbf{q}}^* \\ V_1\gamma_{\mathbf{q}}^* + V_3\gamma_{2\mathbf{q}} & V_0 + V_2\beta_{\mathbf{q}} & V_1\gamma_{\mathbf{q}}^* + V_3\gamma_{2\mathbf{q}} & U + V_2\beta_{\mathbf{q}} \end{pmatrix} \tag{4.9}$$

with

$$\beta_{\mathbf{q}} = 2\left(\cos\mathbf{q}\cdot\mathbf{b}_1 + \cos\mathbf{q}\cdot\mathbf{b}_2 + \cos\mathbf{q}\cdot\mathbf{b}_3\right) \quad \text{and} \quad \gamma_{\mathbf{q}} = e^{i\mathbf{q}\cdot\mathbf{a}_1} + e^{i\mathbf{q}\cdot\mathbf{a}_2} + e^{i\mathbf{q}\cdot\mathbf{a}_3} \tag{4.10}$$

where the vectors $\mathbf{b}_i$ are the second-neighbor vectors on the honeycomb lattice (hence first neighbors on the Bravais lattice):

$$\mathbf{b}_1 = 2\mathbf{a}_1 + \mathbf{a}_2 \qquad \mathbf{b}_2 = \mathbf{a}_1 + 2\mathbf{a}_2 \qquad \mathbf{b}_3 = \mathbf{a}_2 - \mathbf{a}_1 \tag{4.11}$$

The order of orbitals adopted in this matrix notation is (w_1, w_4, w_2, w_3): the first two orbitals belong to the "first layer", the last two to the "second layer".

The local density $n_{\mathbf{R}\sigma}^a$ can only take the values 0 or 1, but the Fourier transforms $\tilde{n}_{\mathbf{q}}^a$ are potentially macroscopic variables. In particular, $\sum_a \tilde{n}_0^a$ is the total number of particles. If a charge density wave were in place at wave vector $\mathbf{q}$, a certain combination (over a) of $\tilde{n}_{\mathbf{q}}^a$ would also take a macroscopic, i.e., classical, value. Hence, for the sake of detecting charge order in the strong-coupling limit, we can treat the variables $\tilde{n}_{\mathbf{q}}^a$ as classical.

The matrix (4.9) can be diagonalized by a unitary matrix:

$$\tilde{V}_{\mathbf{q}}^{ab} = \sum_{r=1}^{4} U_{\mathbf{q}}^{ar} \lambda_{\mathbf{q}}^{(r)} U_{\mathbf{q}}^{br*} \tag{4.12}$$

and thus the interaction energy can take the form

$$H_{\text{int}} = \frac{1}{2} \sum_{\mathbf{q}} \sum_{r=1}^{4} \lambda_{\mathbf{q}}^{(r)} |m_{\mathbf{q}}^{(r)}|^2 \qquad \left(m_{\mathbf{q}}^{(r)} = U_{\mathbf{q}}^{ar*} \tilde{n}_{\mathbf{q}}^a \right) \qquad (4.13)$$

with the eigenvalues

$$\lambda_{\mathbf{q}}^{(1)} = U + V_0 + 2V_2\beta_{\mathbf{q}} + 2|V_1\gamma_{\mathbf{q}} + V_3\gamma_{2\mathbf{q}}^*| \qquad (4.14)$$

$$\lambda_{\mathbf{q}}^{(2)} = U + V_0 + 2V_2\beta_{\mathbf{q}} - 2|V_1\gamma_{\mathbf{q}} + V_3\gamma_{2\mathbf{q}}^*| \qquad (4.15)$$

$$\lambda_{\mathbf{q}}^{(3)} = \lambda_{\mathbf{q}}^{(4)} = U - V_0 \qquad (4.16)$$

The uniform solution $\tilde{n}_{\mathbf{0}}^a = (1,1,1,1)$ corresponds to $\lambda_{\mathbf{0}}^{(1)}$, which is the largest possible eigenvalue, and is favored by the (neglected) kinetic energy. Charge order instabilities in the strong-coupling limit occur for negative eigenvalues, since they can be lower the interaction energy. When substituting the values (4.5), one finds that the maximum eigenvalue is $\lambda_{\mathbf{0}}^{(1)} = 12U$ and the minimum eigenvalue is zero, the latter at the Dirac points $\mathbf{q} = \mathbf{K}$ and $\mathbf{q} = \mathbf{K}'$ for $\lambda_{\mathbf{q}}^{(1)}$, and at all wavevectors for $\lambda_{\mathbf{q}}^{(2,3,4)}$. This means that the system has no instabilities in the strong-coupling limit, only indifferent states (zero eigenvalue), especially at wavevectors $\mathbf{K}$ and $\mathbf{K}'$. When probing such instabilities with a cluster method, we should therefore make sure that these two wavevectors belong to the reciprocal cluster. The 12-site (hexagonal) cluster used in this work statisfies this requirement.

4.3 Computational procedure

The VCA approximation as summarized in section 2.4 only applies to systems with on-site interactions, since the Hamiltonians H and H' must differ by one-body terms only, i.e., they must have the same interaction part. This is not true if extended interactions are present, as they are partially truncated when the lattice is tiled into clusters. To treat the extended Hubbard model, one must apply further approximations. For instance, we can apply a Hartree (or mean-field) decomposition on the extended interactions that straddle different clusters, while interactions (local or extended) within each cluster are treated exactly. This is called the dynamical Hartree approximation (DHA) and has been used in Refs [98, 31] in order to assess the effect of extended interactions on strongly-correlated superconductivity. We will explain this approach in this section.

Let us consider a Hamiltonian of the form

$$H = H_0(\mathbf{t}) + \frac{1}{2} \sum_{i,j} V_{ij} n_i n_j \qquad (4.17)$$

where i, j are compound indices for lattice site and orbital, $n_{i\sigma}$ is the number of electrons of spin σ on site/orbital i, and $n_i = n_{i\uparrow} + n_{i\downarrow}$ (the index i is a composite of honeycomb

site **r** and layer ℓ indices as used in Sect. 4.2, or of Bravais lattice site **R** and orbital index a used in Sect. 4.2.1). The factor $\frac{1}{2}$ in the last term comes from the independent sums on i and j rather than a sum over pairs (i,j). In the dynamical Hartree approximation, the extended interactions in the model Hamiltonian (4.17) are replaced by

$$\frac{1}{2}\sum_{i,j}V_{ij}^{c}n_i n_j + \frac{1}{2}\sum_{i,j}V_{ij}^{ic}(\bar{n}_i n_j + n_i \bar{n}_j - \bar{n}_i \bar{n}_j) \tag{4.18}$$

where V_{ij}^{c} denotes the extended interaction between orbitals belonging to the same cluster, whereas V_{ij}^{ic} denotes those interactions between orbitals of different clusters. Here $\bar{n}_i$ is a mean-field, presumably the average of n_i, but not necessarily, as we will see below. Both the first term ($\hat{V}^{c}$) and the second term ($\hat{V}^{ic}$), which is a one-body operator, are part of the lattice Hamiltonian H and of the VCA reference Hamiltonian H'.

Let us express the index i as a cluster index c and a site-within-cluster index α. Then Eq. 4.19 can be expressed as

$$\frac{1}{2}\sum_{c}\sum_{\alpha,\beta}\tilde{V}_{\alpha\beta}^{c}n_{c,\alpha}n_{c,\beta} + \frac{1}{2}\sum_{c,c',\alpha,\beta}\tilde{V}_{\alpha\beta}^{ic}(\bar{n}_\alpha n_{c,\beta} + n_{c,\alpha}\bar{n}_\beta - \bar{n}_\alpha \bar{n}_\beta) \tag{4.19}$$

where we have assumed that the mean fields $\bar{n}_i$ are the same on all clusters, i.e., that they have minimally the periodicity of the superlattice, hence $\bar{n}_i = \bar{n}_\alpha$. We have consequently replaced the large, $N \times N$ and block diagonal matrix V_{ij}^{c} by a small, $N_c \times N_c$ matrix $\tilde{V}_{\alpha\beta}^{c}$, and we have likewise "folded" the large $N \times N$ matrix V_{ij}^{ic} into the $N_c \times N_c$ matrix $\tilde{V}_{\alpha\beta}^{ic}$.

In order to make this last point clearer, let us consider the simple example of a one-dimensional lattice with nearest-neighbor interaction v, tiled with 3-site clusters. The interaction Hamiltonian

$$H_{int} = v\sum_{i=0}^{N}n_i n_{i+1} \tag{4.20}$$

would lead to the following 3×3 interaction matrices:

$$\tilde{V}^{c} = v\begin{pmatrix} 0 & 1 & 0 \\ 1 & 0 & 1 \\ 0 & 1 & 0 \end{pmatrix} \qquad \tilde{V}^{ic} = v\begin{pmatrix} 0 & 0 & 1 \\ 0 & 0 & 0 \\ 1 & 0 & 0 \end{pmatrix} \tag{4.21}$$

In practice, the symmetric matrix $\tilde{V}_{\alpha\beta}^{ic}$ is diagonalized and the mean-field inter-cluster interaction is expressed in terms of eigenoperators m_μ:

$$\hat{V}^{ic} = \sum_{\mu}D_\mu\left[\bar{m}_\mu m_\mu - \frac{1}{2}\bar{m}_\mu^2\right] \tag{4.22}$$

85

For instance, in the above simple one-dimensional problem, these eigenoperators m_μ and their corresponding eigenvalues D_μ are

$$D_1 = -v \qquad\qquad m_1 = (n_1 - n_3)/\sqrt{2} \qquad\qquad (4.23)$$

$$D_2 = 0 \qquad\qquad m_2 = n_2 \qquad\qquad\qquad (4.24)$$

$$D_3 = v \qquad\qquad m_3 = (n_1 + n_3)/\sqrt{2} \qquad\qquad (4.25)$$

The mean fields $\bar{n}_i$ are determined either by applying (i) self-consistency or (ii) a variational method. In the case of ordinary mean-field theory, in which the mean-field Hamiltonian is entirely free of interactions, these two approaches are identical. In the present case, where the mean-field Hamiltonian also contains interactions treated exactly within a cluster, self-consistency does not necessarily yield the same solution as energy minimization. In the first case, the assignation $\bar{n}_i \leftarrow \langle n_i \rangle$ would be used to iteratively improve on the value of $\bar{n}_i$ until convergence. In the second case, one could treat $\bar{n}_i$ like any other Weiss field in the VCA approach, except that $\bar{n}_i$ is not defined only on the cluster, but on the whole lattice. We will follow the latter approach below.
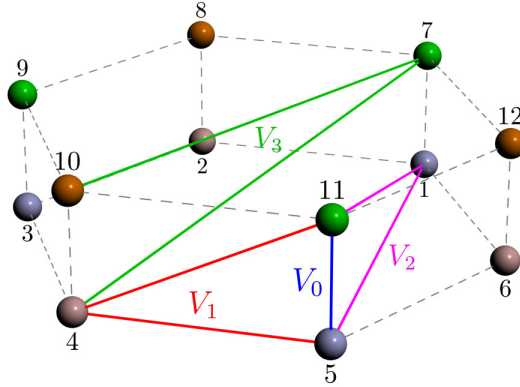
Figure 4.1
12-site cluster used in this work. The extended interactions V_0 to V_3 are shown. Different Wannier orbitals are shown as spheres of different colors. Orbitals w_1 and w_4 are located, say, on the bottom layer, whereas orbitals w_2 and w_3 are located on the top layer.

4.4 The normal state at quarter filling

In this work we use a 12-site cluster containing 3 unit cells of the low-energy model. It is made of two superimposed hexagonal clusters, as illustrated on Fig. 4.1. On that figure the various extended interactions V_0 to V_3 are indicated. The three wavevectors of the reciprocal cluster are $\mathbf{\Gamma} = \mathbf{0}$, $\mathbf{K}$ and $\mathbf{K}'$. The 12×12 matrix of inter-cluster interactions is given in Table 4.1 and the eigenoperators m_μ used in the dynamical Hartree approximation are illustrated in the lower part of the same table.

$$\tilde{V}^{\text{ic}} = \begin{pmatrix}
0 & V_3 & 2V_2 & V_1 & 2V_2 & V_3 & 0 & V_3 & 2V_2 & V_1 & 2V_2 & V_3 \\
V_3 & 0 & V_3 & 2V_2 & V_1 & 2V_2 & V_3 & 0 & V_3 & 2V_2 & V_1 & 2V_2 \\
2V_2 & V_3 & 0 & V_3 & 2V_2 & V_1 & 2V_2 & V_3 & 0 & V_3 & 2V_2 & V_1 \\
V_1 & 2V_2 & V_3 & 0 & V_3 & 2V_2 & V_1 & 2V_2 & V_3 & 0 & V_3 & 2V_2 \\
2V_2 & V_1 & 2V_2 & V_3 & 0 & V_3 & 2V_2 & V_1 & 2V_2 & V_3 & 0 & V_3 \\
V_3 & 2V_2 & V_1 & 2V_2 & V_3 & 0 & V_3 & 2V_2 & V_1 & 2V_2 & V_3 & 0 \\
0 & V_3 & 2V_2 & V_1 & 2V_2 & V_3 & 0 & V_3 & 2V_2 & V_1 & 2V_2 & V_3 \\
V_3 & 0 & V_3 & 2V_2 & V_1 & 2V_2 & V_3 & 0 & V_3 & 2V_2 & V_1 & 2V_2 \\
2V_2 & V_3 & 0 & V_3 & 2V_2 & V_1 & 2V_2 & V_3 & 0 & V_3 & 2V_2 & V_1 \\
V_1 & 2V_2 & V_3 & 0 & V_3 & 2V_2 & V_1 & 2V_2 & V_3 & 0 & V_3 & 2V_2 \\
2V_2 & V_1 & 2V_2 & V_3 & 0 & V_3 & 2V_2 & V_1 & 2V_2 & V_3 & 0 & V_3 \\
0 & 2V_2 & V_1 & 2V_2 & V_3 & 0 & V_3 & 2V_2 & V_1 & 2V_2 & V_3 & 0
\end{pmatrix}$$

$D_0 = 2(V_1 + 4V_2 + 2V_3) = \frac{16}{3}U$ $D_1 = 2(V_1 - 2V_2 - V_3) = -\frac{2}{3}U$ $D_2 = 2(V_1 - 2V_2 - V_3) = -\frac{2}{3}U$ $D_3 = -2(V_1 + 2V_2 - V_3) = -2U$

$D_4 = -2(V_1 + 2V_2 - V_3) = -2U$ $D_5 = -2(V_1 - 4V_2 + 2V_3) = 0$ $D_6 = 0$ $D_7 = 0$

$D_8 = 0$ $D_9 = 0$ $D_{10} = 0$ $D_{11} = 0$
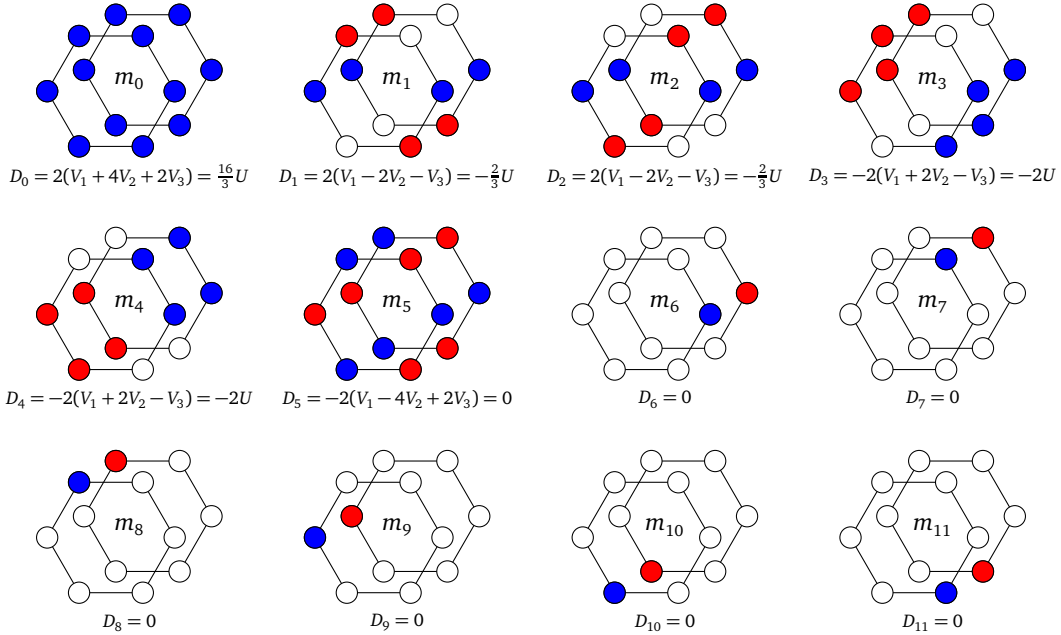
Table 4.1

Inter-cluster coupling matrix for the 12-site cluster used in this work. The numbering of sites is illustrated on Fig. 4.1. Bottom: eigenvalues D_μ and corresponding eigenvectors (or eigenoperators) m_μ of this matrix. The eigenoperators are shown graphically as a function of site on the 12-site cluster: blue means 1 and red -1. The eigenvalues are also shown as a function of the on-site repulsion U when the constraints (4.5) are applied.

87
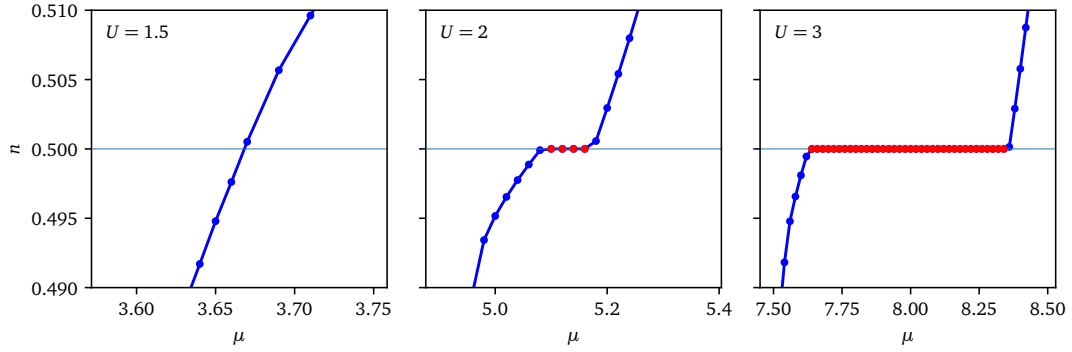
Figure 4.2
Electronic density vs chemical potential μ for different interaction strengths at quarter filling. The presence of a plateau (in red) is the signature of an insulating state, and the width of the plateau is the magnitude of the gap. The insulator-to-metal transition occurs between $U = 1.5$ and $U = 2$.
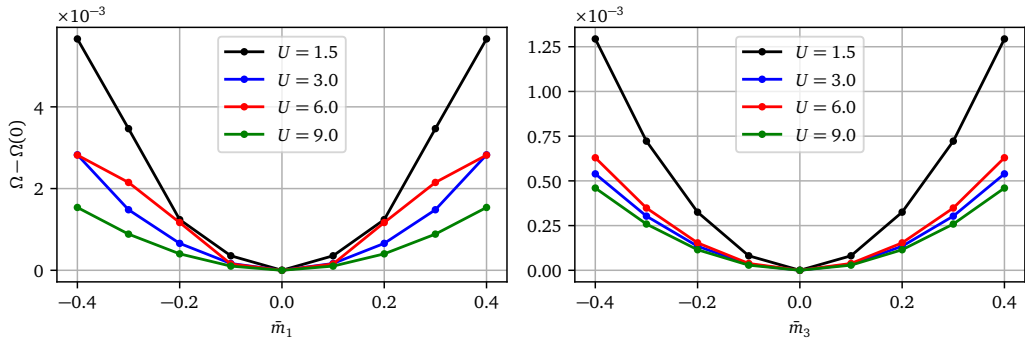
Figure 4.3
Left panel : The Potthoff functional Ω as a function of the charge-density-wave Weiss field $\bar{m}_1$ at quarter-filling. Right panel: the same, for the charge-density-wave Weiss field $\bar{m}_3$. See Table 4.1 for an illustration of the density-waves m_1 and m_3. The symmetric state (no charge density wave) $\bar{m}_{1,3} = 0$ is stable.

We begin by investigating the normal state at quarter filling, for several values of the interaction U, all the extended interactions following from U according to Eq. (4.5). We will start by applying VCA to detect the insulating state, assuming that no charge order is present. To do this, we treat the cluster chemical potential, μ_c, as the sole variational parameter in the VCA procedure. We do not take into account inter-cluster interactions, i.e., the Hartree approximation described in Sect. 4.3. Indeed, all the sites of the 12-site cluster are equivalent in the absence of charge order, meaning that the relevant (normalized) eigenvector of the inter-cluster interaction matrix V^{ic} is

$$m_0 = \frac{1}{2\sqrt{3}} \sum_{i=1}^{12} n_i \tag{4.26}$$

Therefore, adding the corresponding mean-field $\bar{m}_0 m_0$ to the lattice Hamiltonian would simply shift the chemical potential by $-\bar{m}_0$, and leave the variational space used in VCA unchanged. This would therefore not help us in determining whether there is a gap or not.

The signature of the Mott gap will be a plateau in the relation between μ and the density n. This is shown in Fig. 4.2 for a few values of the interaction U. Using the cluster chemical potential μ_c as a variational parameter makes the plateau very sharp, whereas not using VCA, i.e., simple cluster perturbation theory (CPT) would make the plateau softer, thereby making the transition to the metallic state more difficult to detect. In the case shown, the metal-insulator transition clear occurs between $U = 1.5$meV and $U = 2$meV. This Mott transition is essentially caused by extended interactions.

The question then arises as to the nature of the insulating state at quarter filling: is there a charge density wave or not? As shown in Sect. 4.2.1, the charge fluctuations are expected to be large, because a full array of charge configurations do not affect the energy in the strong-coupling limit when the extended interactions follow Eq. (4.5). We do expect, on intuitive grounds, that the kinetic energy terms would be unfavorable to charge order. Nevertheless, in order to probe the possible existence of charge order, we will apply Hartree inter-cluster mean-field theory, as described in Sect. 4.3. In order to put all the chances on our side, we will probe one of the eigenoperators with the lowest (negative) eigenvalues in Table 4.1, namely one of those with $D = -2U$:

$$m_3 = \frac{1}{2\sqrt{2}} \left(n_1 + n_2 - n_4 - n_5 + n_7 + n_8 - n_{10} - n_{11} \right) \tag{4.27}$$

We must then optimize the Potthoff functional as a function of the mean field $\bar{m}_3$, in addition to using μ_c as a variational parameter. On the right panel of Fig. 4.3 we show the Potthoff functional Ω as a function of $\bar{m}_3$ for a value μ_c that actually optimize Ω at a value of μ associated with quarter filling, for a few values of the interaction U. This is to illustrate the absence of nontrivial solution for $\bar{m}_3$, i.e., the value of the mean-field parameter $\bar{m}_3$ that minimizes the energy is indeed zero. This shows that, within this inter-cluster mean-field approximation and for these values of U, there is no charge order this type (m_3 or, equivalently, m_4) at quarter-filling.

We perform the same computation for the m_1 eigenoperator:

$$m_1 = \frac{1}{2\sqrt{2}}\left(n_1 - n_2 + n_4 - n_5 + n_7 - n_8 + n_{10} - n_{11}\right) \tag{4.28}$$

and find similar results, as shown on the left panel of Fig. 4.3. Therefore, for the values of U probed, the quarter-filled state appears to be a pure, uniform Mott insulator, driven by extended interactions.

4.5 The normal state at half filling and antiferromagnetism

The insulating state at half-filling is revealed the same way as at quarter-filling, by applying the VCA with μ_c as a variational parameter. The results are shown in Fig. 4.4, where it appears that the Mott transition occurs between $U = 0.1$meV and $U = 0.25$meV.

We will not probe charge order at half-filling, as an antiferromagnetic state is more likely to occur. The Weiss field used to probe antiferromagnetism is

$$\hat{M} = M \sum_{i=1}^{12} (-1)^i (n_{i\uparrow} - n_{i\downarrow}) \tag{4.29}$$

Fig. 4.5 shows the Potthoff functional as a function of M for different values of the extended interactions compared to the on-site repulsion $U = 3$meV. These different values are characterized by the ratio $a = 3V_1/2U$, which is unity when the extended interactions obey the constraints (4.5). Lower values of a correspond to weaker extended interactions (compared to U). From that figure we see that, even at a relatively strong U (the Mott transition occurs at a much lower value of U), antiferromagnetism is not present at half-filling for the nominal values of the extended interactions defined in (4.5). Upon lowering these interactions, antiferromagnetism appears. Hence the half-filled state should be a true Mott insulator, not an antiferromagnetic insulator.

This is relatively easy to understand in the strong-coupling limit, when (4.5) holds. The low-energy manifold at half-filling in the absence of hopping terms is degenerate non only because of spin, but also because of charge motion: if there is exactly one electron on each site, hopping an electron to the neighboring site does not change the interaction energy, and thus the usual strong-coupling perturbation theory argument leading to an effective Heisenberg model at half-filling and large U does not hold anymore.
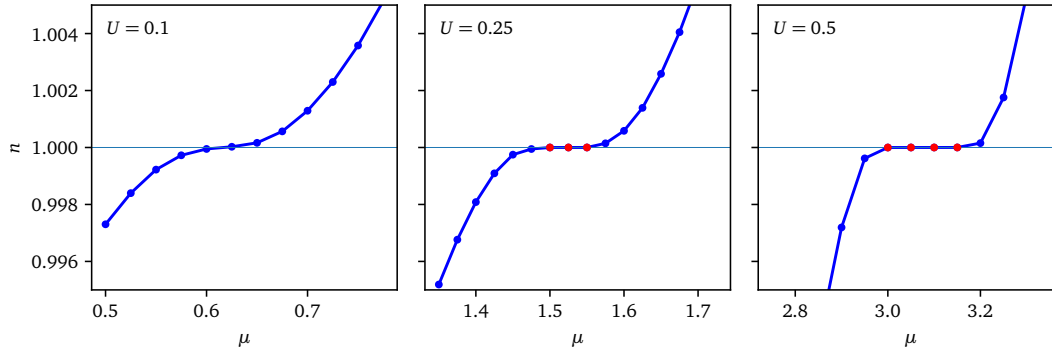
Figure 4.4
Electronic density vs chemical potential μ for different interaction strengths at half filling, similar to Fig. 4.2. The presence of a plateau (in red) is the signature of an insulating state, and the width of the plateau is the magnitude of the gap. The insulator-to-metal transition occurs between $U = 0.1$meV and $U = 0.25$meV.
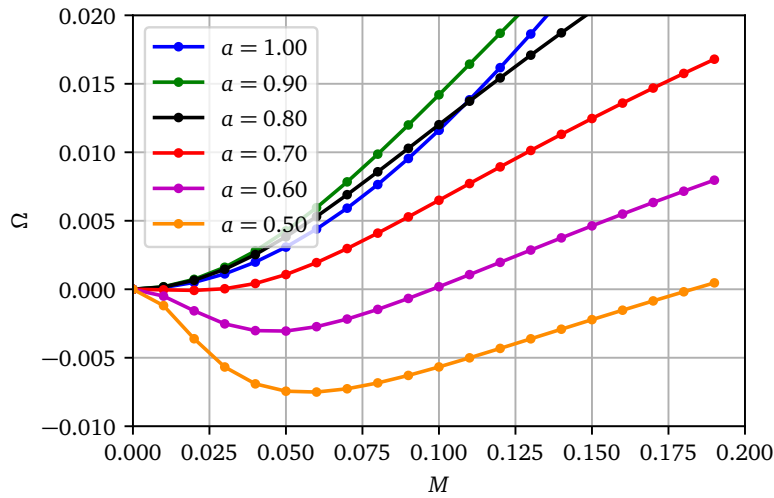
Figure 4.5
Potthoff functional vs the antiferromagnetic Weiss field M' for several values of $a = 3V_1/2U$ and $U = 3$, at half-filling. The case $a = 1$ corresponds to the contraints (4.5), and smaller values of a just weaken the extended interactions compared to the on-site interaction. The value of Ω at $M' = 0$ is subtracted for clarity. Antiferromagnetism appears only below $a = 0.7$, i.e., not for the extended interactions constrained by (4.5).

Conclusion

In this thesis, the superconducting phase, as well as the Mott insulating phase of a twisted bilayer graphene system are investigated. In examining the Mott insulating phase, we have also considered the possibility of the presence of broken symmetry phases such as charge density waves or antiferromagnetism. The computational methods we have used in these studies are known as quantum cluster methods. We described the basic concepts of these methods in Chapter 2.

The interaction between the layers of twisted bilayer graphene, at a special twist angle called the magic angle, causes the formation of four narrow bands, called the *flat bands*. The Fermi velocity of electrons in these bands is very low and therefore the electrons are highly correlated. When the Fermi energy is within the range of these bands, the system exhibits significant properties that originate from the strong correlation of electrons located in these flat bands.

At some certain twist angles, these flat bands are separated from the other bands by an energy gap, and we can obtain an effective model for describing the system. The effective model that we use in this thesis, which I have named the Vafek model, Has been introduced by Jian Kang and Oskar Vafek in Ref. [40]. We were able to add intra-orbital and inter-orbital interactions to this model and use it to describe the superconducting phase of the system as well as the insulating-metal phase transition, which is actually the result of these extended interactions.

By stacking the two layers of graphene on top of each other and rotating them by a magic angle, a periodic pattern is observed, called the moiré lattice. In the case of this system, the latter is a triangular lattice whose lattice parameter depends on the rotation angle. At small twist angle, it is much larger than the lattice parameter of the original graphene lattice. The Vafek model is based on four Wannier orbitals located at the center of the moiré lattice triangles (two orbitals in the center of each triangle). Thus these orbitals form a honeycomb lattice. Since there must be two Wannier orbitals at each site of this honeycomb lattice, we have considered it as a two-layer lattice so that the two orbitals that must be on the same site are in different layers. We define intra- and inter-orbital electron-electron interactions for the model. This effective model is appropriate for a twist angle $\theta = 1.30\circ$, but we expect that the shape of orbitals and the hopping amplitude between them does not change dramatically at $\theta = 1.08\circ$, where the system becomes a superconductor.

To study the superconducting phase, we divide this honeycomb lattice into smaller clusters and use cluster dynamical mean field theory (CDMFT). In this calculation, we have done the clustering so that each cluster consists of four lattice sites and is surrounded by six auxiliary orbitals, which we call bath orbitals.

Assuming that the electrons at neighboring sites can form Cooper pairs, we have defined the appropriate order parameters for the superconducting phase of the system, given the symmetries that exist in a honeycomb lattice. We used CDMFT calculations to obtain these order parameters. These calculations confirmed the occurence of superconductivity in this system and we were able to identify the symmetry of the order parameter: $p \pm ip$. If correct, this would be the first known system with such a symmetry.

The range of electron densities at which the system is in the superconducting phase is well consistent with experimental measurements. The effective model we have used to describe this system has approximate electron-hole symmetry, and therefore the superconducting phase is observed in both electron-doped and hole-doped densities. In experimental measurements, the superconducting phase is confirmed only for a range of hole-doped densities at $1.08°$. In addition to superconducting behavior, the system can exhibit insulating behavior in situations where the flat bands are quarter-filled or three-quarter-filled. There is no energy gap between the flat bands to justify the presence of these insulating phases. These insulating phases are therefore strongly correlated phases that occur due to interactions. In the last chapter of this thesis, we have studied these correlated insulator phases.

To investigate the insulating phases, in addition to intra-orbital interactions, we have included inter-orbital interactions. These are defined in two types, inter-layer and intra-layer so that each electron can interact with electrons in the opposite layer, on the same hexagonal site. Intralayer interactions are also defined in such a way that each electron in a particular site can interact with electrons in the first, second, and third-neighbor sites of the honeycomb lattice.

In order to be able to study the effect of these long-range interactions, the clustering should be done in a way that each cluster contains these extended interactions. We have also taken into account the inter-cluster terms using a mean field approximation. The smallest cluster that can be considered with these features is a hexagonal cluster with two Wannier orbitals at each site at the top and bottom layers. In other words, each cluster contains 12 Wannier orbitals. The relatively large size of the clusters in this clustering model prevents us from using the CDMFT method. Therefore, we have used the variational cluster approximation to solve this problem.

The results obtained by this approximation confirm the existence of the Mott insulating phase at certain values of the carrier density. More precisely, the system exhibits insulating behavior at half-filling, quarter-filling, and three-quarter-filling densities (due to electron-hole symmetry, we will see a similar behavior for electron- and hole-doped systems).

After proving the existence of these insulating phases, another issue that we have investigated is the presence or absence of charge density waves in this system. To answer

this question, we first examine the system analytically in the strong-coupling limit and obtain the possible instabilities of charge order. These instabilities are created solely by interactions and should be suppressed by the kinetic energy of the system. Using the VCA method, we compute and plot the Potthoff self-energy functional as a function of defined order parameters. The results of the calculations show the Potthoff functional has no non trivial minimum. This means that, there is no charge order phase for this model with the defined interactions.

These calculations were performed at quarter-filling. At half-filling, the antiferromagnetic phase is more likely to occur, so we define an order parameter corresponding to this phase for the system, and again, similar to the quarter-filling state, use the VCA method to check for the presence or absence of this phase. The results show that there is no antiferromagnetic order in the system for the values of the extended interactions. But by reducing the intensity of the extended interactions relative to the local interaction, an antiferromagnetic order is observed.

Bibliography

[1] Philip Warren Anderson. Localized magnetic states in metals. *Physical Review*, 124(1):41, 1961.

[2] Tsuneya Ando. Theory of electronic states and transport in carbon nanotubes. *Journal of the Physical Society of Japan*, 74(3):777–817, 2005.

[3] Zhaojun Bai. Krylov subspace techniques for reduced-order modeling of large-scale dynamical systems. *Applied numerical mathematics*, 43(1-2):9–44, 2002.

[4] Zhaojun Bai, James Demmel, Jack Dongarra, Axel Ruhe, and Henk van der Vorst. *Templates for the solution of algebraic eigenvalue problems: a practical guide*. SIAM, 2000.

[5] Gordon Baym and Leo P Kadanoff. Conservation laws and correlation functions. *Physical Review*, 124(2):287, 1961.

[6] J George Bednorz and K Alex Müller. Possible high t_c superconductivity in the Ba-La-Cu-O system. *Zeitschrift für Physik B Condensed Matter*, 64(2):189–193, 1986.

[7] Carl Bender, Fred Cooper, Richard Kenway, and LM Simmons Jr. Continuum regulation of the strong-coupling expansion for quantum field theory. *Physical Review D*, 24(10):2693, 1981.

[8] Carl M Bender, Fred Cooper, GS Guralnik, and David H Sharp. Strong-coupling expansion in quantum field theory. *Physical Review D*, 19(6):1865, 1979.

[9] Rafi Bistritzer and Allan H MacDonald. Moiré bands in twisted double-layer graphene. *Proceedings of the National Academy of Sciences*, 108(30):12233–12237, 2011.

[10] Annica M Black-Schaffer, Wei Wu, and Karyn Le Hur. Chiral d-wave superconductivity on the honeycomb lattice close to the Mott state. *Physical Review B*, 90(5):054521, 2014.

[11] CJ Bolech, SS Kancharla, and G Kotliar. Cellular dynamical mean-field theory for the one-dimensional extended Hubbard model. *Physical Review B*, 67(7):075110, 2003.

[12] Jolanta Borysiuk, Jakub Sołtys, and Jacek Piechota. Stacking sequence dependence of graphene layers on SiC (0001) – experimental and theoretical investigation. *Journal of Applied Physics*, 109(9):093523, 2011.

[13] NB Brandt, SM Chudinov, and Ya G Ponomarev. Modern problems in condensed matter sciences. *Agranovich and AA Maradudin: North-Holland, Am-sterdam*, 20, 1988.

[14] William F Brinkman and T Maurice Rice. Application of Gutzwiller's variational method to the metal-insulator transition. *Physical Review B*, 2(10):4302, 1970.

[15] N Bulut, DJ Scalapino, and SR White. One-electron spectral weight of the doped two-dimensional Hubbard model. *Physical review letters*, 72(5):705, 1994.

[16] N Bulut, DJ Scalapino, and SR White. Quasiparticle dispersion in the cuprate superconductors and the two-dimensional Hubbard model. *Physical Review B*, 50(10):7215, 1994.

[17] Michel Caffarel and Werner Krauth. Exact diagonalization approach to correlated fermions in infinite dimensions: Mott transition and superconductivity. *Physical review letters*, 72(10):1545, 1994.

[18] Yuan Cao, Valla Fatemi, Ahmet Demir, Shiang Fang, Spencer L Tomarken, Jason Y Luo, Javier D Sanchez-Yamagishi, Kenji Watanabe, Takashi Taniguchi, Efthimios Kaxiras, et al. Correlated insulator behaviour at half-filling in magic-angle graphene superlattices. *Nature*, 556(7699):80, 2018.

[19] Yuan Cao, Valla Fatemi, Shiang Fang, Kenji Watanabe, Takashi Taniguchi, Efthimios Kaxiras, and Pablo Jarillo-Herrero. Unconventional superconductivity in magic-angle graphene superlattices. *Nature*, 556(7699):43, 2018.

[20] J-C Charlier, J-P Michenaud, and Xavier Gonze. First-principles study of the electronic properties of simple hexagonal graphite. *Physical Review B*, 46(8):4531, 1992.

[21] Wanying Chen, Yonghuan Chu, Tongyun Huang, and Tianxing Ma. Metal-insulator transition and dominant $d + id$ pairing symmetry in twisted bilayer graphene. *Phys. Rev. B*, 101(15):155413, April 2020.

[22] Charles E Creffield, EG Klepfish, Edward Roy Pike, and Sarben Sarkar. Spectral weight function for the half-filled Hubbard model: a singular value decomposition approach. *Physical review letters*, 75(3):517, 1995.

[23] Elbio Dagotto. Correlated electrons in high-temperature superconductors. *Reviews of Modern Physics*, 66(3):763, 1994.

[24] RS Deacon, K-C Chuang, RJ Nicholas, KS Novoselov, and AK Geim. Cyclotron resonance study of the electron and hole velocity in graphene monolayers. *Physical Review B*, 76(8):081406, 2007.

[25] Cory R Dean, L Wang, P Maher, C Forsythe, Fereshte Ghahari, Y Gao, Jyoti Katoch, M Ishigami, P Moon, M Koshino, et al. Hofstadters butterfly and the fractal quantum Hall effect in moiré superlattices. *Nature*, 497(7451):598–602, 2013.

[26] John F Dodaro, Steven A Kivelson, Yoni Schattner, Xiao-Qi Sun, and Chao Wang. Phases of a phenomenological model of twisted bilayer graphene. *Physical Review B*, 98(7):075154, 2018.

[27] JMB Lopes Dos Santos, NMR Peres, and AH Castro Neto. Graphene bilayer with a twist: Electronic structure. *Physical review letters*, 99(25):256802, 2007.

[28] JMB Lopes Dos Santos, NMR Peres, and AH Castro Neto. Graphene bilayer with a twist: Electronic structure. *Physical review letters*, 99(25):256802, 2007.

[29] JMB Lopes dos Santos, NMR Peres, and AH Castro Neto. Continuum model of the twisted graphene bilayer. *Physical Review B*, 86(15):155449, 2012.

[30] Mildred S Dresselhaus and Gene Dresselhaus. Intercalation compounds of graphite. *Advances in physics*, 51(1):1–186, 2002.

[31] JPL Faye, P Sahebsara, and David Sénéchal. Chiral triplet superconductivity on the graphene lattice. *Physical Review B*, 92(8):085121, 2015.

[32] Antoine Georges. Strongly correlated electron materials: Dynamical mean-field theory and electronic structure. In *AIP Conference Proceedings*, volume 715, pages 3–74. American Institute of Physics, 2004.

[33] Antoine Georges, Gabriel Kotliar, Werner Krauth, and Marcelo J Rozenberg. Dynamical mean-field theory of strongly correlated fermion systems and the limit of infinite dimensions. *Reviews of Modern Physics*, 68(1):13, 1996.

[34] José González Carmona and Tobias Stauber. Kohn-Luttinger superconductivity in twisted bilayer graphene. 2019.

[35] Zachary AH Goodwin, Fabiano Corsetti, Arash A Mostofi, and Johannes Lischner. Attractive electron-electron interactions from internal screening in magic-angle twisted bilayer graphene. *Physical Review B*, 100(23):235424, 2019.

[36] Claudius Gros and Roser Valenti. Cluster expansion for the self-energy: A simple many-body method for interpreting the photoemission spectra of correlated Fermi systems. *Physical Review B*, 48(1):418, 1993.

[37] M Gu, Axel Ruhe, R Lehoucq, D Sorensen, R Freund, G Sleijpen, H van der Vorst, Zhaojun Bai, and R Li. Hermitian eigenvalue problems. In *Templates for the Solution of Algebraic Eigenvalue Problems: A Practical Guide*, pages 45–107. SIAM, 2000.

[38] Huaiming Guo, Xingchuan Zhu, Shiping Feng, and Richard T Scalettar. Pairing symmetry of interacting fermions on a twisted bilayer graphene superlattice. *Physical Review B*, 97(23):235453, 2018.

[39] Benjamin Hunt, Javier D Sanchez-Yamagishi, Andrea F Young, Matthew Yankowitz, Brian J LeRoy, Kenji Watanabe, Takashi Taniguchi, Pilkyung Moon, Mikito Koshino, Pablo Jarillo-Herrero, et al. Massive Dirac fermions and Hofstadter butterfly in a van der Waals heterostructure. *Science*, 340(6139):1427–1430, 2013.

[40] Jian Kang and Oskar Vafek. Symmetry, maximally localized Wannier states, and a low-energy model for twisted bilayer graphene narrow bands. *Physical Review X*, 8(3):031088, 2018.

[41] Jian Kang and Oskar Vafek. Strong coupling phases of partially filled twisted bilayer graphene narrow bands. *Physical review letters*, 122(24):246401, 2019.

[42] Dante M. Kennes, Johannes Lischner, and Christoph Karrasch. Strong correlations and $d + id$ superconductivity in twisted bilayer graphene. *Phys. Rev. B*, 98(24):241407, December 2018.

[43] M Kindermann and PN First. Local sublattice-symmetry breaking in rotationally faulted multilayer graphene. *Physical Review B*, 83(4):045425, 2011.

[44] K Kobayashi, T Mizokawa, A Fujimori, M Isobe, Y Ueda, T Tohyama, and S Maekawa. Finite temperature effects in a one-dimensional Mott-Hubbard insulator: Angle-resolved photoemission study of na 0.96 v 2 o 5. *Physical review letters*, 82(4):803, 1999.

[45] Mikito Koshino. Interlayer interaction in general incommensurate atomic layers. *New Journal of Physics*, 17(1):015014, 2015.

[46] Mikito Koshino and Pilkyung Moon. Electronic properties of incommensurate atomic layers. *Journal of the Physical Society of Japan*, 84(12):121001, 2015.

[47] Gabriel Kotliar, Sergej Y Savrasov, Gunnar Pálsson, and Giulio Biroli. Cellular dynamical mean field approach to strongly correlated systems. *Physical review letters*, 87(18):186401, 2001.

[48] Gabriel Kotliar and Dieter Vollhardt. Strongly correlated materials: Insights from dynamical mean-field theory. *Physics today*, 57(3):53–60, 2004.

[49] AN Krylov. On the numerical solution of equations whose solution determine the frequency of small vibrations of material systems. *Izv. Akad. Nauk. SSSR Otd Mat. Estest*, 1:491–539, 1931.

[50] AB Kuzmenko, Iris Crassee, Dirk Van Der Marel, P Blake, and KS Novoselov. Determination of the gate-tunable band gap and tight-binding parameters in bilayer graphene using infrared spectroscopy. *Physical Review B*, 80(16):165406, 2009.

[51] P Lauffer, KV Emtsev, R Graupner, Th Seyller, L Ley, SA Reshanov, and HB Weber. Atomic and electronic structure of few-layer graphene on SiC (0001) studied with scanning tunneling microscopy and spectroscopy. *Physical Review B*, 77(15):155426, 2008.

[52] Jae-Kap Lee, Seung-Cheol Lee, Jae-Pyoung Ahn, Soo-Chul Kim, John IB Wilson, and Phillip John. The growth of aa graphite on (111) diamond. *The Journal of chemical physics*, 129(23):234709, 2008.

[53] Pak Wo Leung, Zhiping Liu, Efstratios Manousakis, MA Novotny, and Paul E Oppenheimer. Density of states of the two-dimensional Hubbard model on a 4× 4 lattice. *Physical Review B*, 46(18):11779, 1992.

[54] Pak Wo Leung, Barrett O Wells, and Robert J Gooding. Comparison of 32-site exact-diagonalization results and ARPES spectral functions for the antiferromagnetic insulator $sr_2cuo_2cl_2$. *Physical Review B*, 56(10):6320, 1997.

[55] ZQ Li, EA Henriksen, Zhigang Jiang, Zhao Hao, Michael C Martin, P Kim, HL Stormer, and Dimitri N Basov. Band structure asymmetry of bilayer graphene revealed by infrared spectroscopy. *Physical Review Letters*, 102(3):037403, 2009.

[56] AI Lichtenstein and MI Katsnelson. Antiferromagnetism and d-wave superconductivity in cuprates: A cluster dynamical mean-field theory. *Physical Review B*, 62(14):R9283, 2000.

[57] Wei Liu, Stephan Kraemer, Deblina Sarkar, Hong Li, Pulickel M Ajayan, and Kaustav Banerjee. Controllable and rapid synthesis of high-quality and large-area Bernal stacked bilayer graphene using chemical vapor deposition. *Chemistry of materials*, 26(2):907–915, 2014.

[58] Zheng Liu, Kazu Suenaga, Peter JF Harris, and Sumio Iijima. Open and closed edges of graphene layers. *Physical review letters*, 102(1):015501, 2009.

[59] A Luican, Guohong Li, A Reina, J Kong, RR Nair, Konstantin S Novoselov, Andre K Geim, and EY Andrei. Single-layer behavior and its breakdown in twisted graphene layers. *Physical review letters*, 106(12):126802, 2011.

[60] Joaquin Mazdak Luttinger and John Clive Ward. Ground-state energy of a many-fermion system. ii. *Physical Review*, 118(5):1417, 1960.

[61] DL Mafra, LM Malard, SK Doorn, Han Htoon, Johan Nilsson, AH Castro Neto, and MA Pimenta. Observation of the Kohn anomaly near the k-point of bilayer graphene. *Physical Review B*, 80(24):241414, 2009.

[62] LM Malard, J Nilsson, DC Elias, JC Brant, F Plentz, ES Alves, AH Castro Neto, and MA Pimenta. Probing the electronic structure of bilayer graphene by Raman scattering. *Physical Review B*, 76(20):201401, 2007.

[63] Nicola Marzari and David Vanderbilt. Maximally localized generalized Wannier functions for composite energy bands. *Physical review B*, 56(20):12847, 1997.

[64] Edward McCann and Vladimir I Falko. Landau-level degeneracy and quantum Hall effect in a graphite bilayer. *Physical review letters*, 96(8):086805, 2006.

[65] Edward McCann and Mikito Koshino. The electronic properties of bilayer graphene. *Reports on Progress in physics*, 76(5):056503, 2013.

[66] EJ Mele. Commensuration and interlayer coherence in twisted bilayer graphene. *Phys. Rev. B*, 81:161405, 2010.

[67] Pilkyung Moon and Mikito Koshino. Energy spectrum and quantum Hall effect in twisted bilayer graphene. *Physical Review B*, 85(19):195458, 2012.

[68] Pilkyung Moon and Mikito Koshino. Optical absorption in twisted bilayer graphene. *Physical Review B*, 87(20):205404, 2013.

[69] A Moreo, DJ Scalapino, RL Sugar, SR White, and NE Bickers. Numerical study of the two-dimensional Hubbard model for various band fillings. *Physical Review B*, 41(4):2313, 1990.

[70] NF Mott. On the transition to metallic conduction in semiconductors. *Canadian journal of physics*, 34(12A):1356–1368, 1956.

[71] M Mucha-Kruczyński, JR Wallbank, and VI Fal'Ko. Heterostructures of bilayer graphene and h-BN: Interplay between misalignment, interlayer asymmetry, and trigonal warping. *Physical Review B*, 88(20):205418, 2013.

[72] AH Castro Neto, Francisco Guinea, Nuno MR Peres, Kostya S Novoselov, and Andre K Geim. The electronic properties of graphene. *Reviews of modern physics*, 81(1):109, 2009.

[73] Martin Nuss, Enrico Arrigoni, Markus Aichhorn, and Wolfgang von der Linden. Variational cluster approach to the single-impurity Anderson model. *Physical Review B*, 85(23):235107, 2012.

[74] B Pahlevanzadeh, P Sahebsara, and D Sénéchal. Charge order and antiferromagnetism in twisted bilayer graphene from the variational cluster approximation. *arXiv preprint arXiv:2112.00181*, 2021.

[75] B Pahlevanzadeh, P Sahebsara, and David Sénéchal. Chiral p-wave superconductivity in twisted bilayer graphene from dynamical mean field theory. *SciPost Physics*, 11(1):017, 2021.

[76] Stéphane Pairault, David Sénéchal, and A-MS Tremblay. Strong-coupling expansion for the Hubbard model. *Physical review letters*, 80(24):5389, 1998.

[77] Stéphane Pairault, David Sénéchal, and A-MS Tremblay. Strong-coupling perturbation theory of the Hubbard model. *The European Physical Journal B-Condensed Matter and Complex Systems*, 16(1):85–105, 2000.

[78] A Paoletti and P Rudolf. Fluctuation-induced magnetotransport of superconductors in the quasiballistic regime p. 415. *The European Physical Journal B*, 32(4), 2003.

[79] Teemu J Peltonen, Risto Ojajärvi, and Tero T Heikkilä. Mean-field theory for superconductivity in twisted bilayer graphene. *Physical Review B*, 98(22):220504, 2018.

[80] Hoi Chun Po, Liujun Zou, Ashvin Vishwanath, and T Senthil. Origin of Mott insulating behavior and superconductivity in twisted bilayer graphene. *arXiv preprint arXiv:1803.09742*, 2018.

[81] Michael Potthoff. Self-energy-functional approach to systems of correlated electrons. *The European Physical Journal B-Condensed Matter and Complex Systems*, 32(4):429–436, 2003.

[82] Michael Potthoff. Non-perturbative construction of the Luttinger-Ward functional. *arXiv preprint cond-mat/0406671*, 2004.

[83] Michael Potthoff. Variational cluster approximation. In Eva Pavarini, Erik Koch, Dieter Vollhardt, and Alexander Lichtenstein, editors, *DMFT at 25: Infinite Dimensions, Lecture Notes of the Autumn School on Correlated Electrons 2014*. Forschungszentrum Jülich, 2014.

[84] Michael Potthoff, Markus Aichhorn, and Cristopher Dahnken. Variational cluster approach to correlated electron systems in low dimensions. *Physical review letters*, 91(20):206402, 2003.

[85] R Preuss, W Hanke, C Gröber, and HG Evertz. Pseudogaps and their interplay with magnetic excitations in the doped 2d Hubbard model. *Physical review letters*, 79(6):1122, 1997.

[86] R Preuss, A Muramatsu, W Von der Linden, P Dieterich, FF Assaad, and W Hanke. Spectral properties of the one-dimensional Hubbard model. *Physical review letters*, 73(5):732, 1994.

[87] AL Rakhmanov, AV Rozhkov, AO Sboychakov, and Franco Nori. Instabilities of the a a-stacked graphene bilayer. *Physical Review Letters*, 109(20):206801, 2012.

[88] Stephanie Reich, Janina Maultzsch, Christian Thomsen, and Pablo Ordejon. Tight-binding description of graphene. *Physical Review B*, 66(3):035412, 2002.

[89] Bitan Roy and Vladimir Juričić. Unconventional superconductivity in nearly flat bands in twisted bilayer graphene. *Physical Review B*, 99(12):121407, 2019.

[90] AV Rozhkov, AO Sboychakov, AL Rakhmanov, and Franco Nori. Electronic properties of graphene-based bilayer systems. *Physics Reports*, 648:1–104, 2016.

[91] Rei Sakuma. Symmetry-adapted Wannier functions in the maximal localization procedure. *Physical Review B*, 87(23):235109, 2013.

[92] D Sénéchal, D Perez, and M Pioro-Ladriere. Spectral weight of the Hubbard model through cluster perturbation theory. *Physical review letters*, 84(3):522, 2000.

[93] David Sénéchal. Quantum cluster methods: CPT and CDMFT. *Many-Body Physics: From Kondo to Hubbard, Lecture Notes of the Autumn School on Correlated Electrons 2015*, 5:13–1.

[94] David Sénéchal. Bath optimization in the cellular dynamical mean-field theory. *Physical Review B*, 81(23):235125, 2010.

[95] David Sénéchal, Danny Perez, and Dany Plouffe. Cluster perturbation theory for Hubbard models. *Physical Review B*, 66(7):075129, 2002.

[96] Richard N Silver, Devinderjit S Sivia, and James E Gubernatis. Maximum-entropy method for analytic continuation of quantum monte carlo data. *Physical Review B*, 41(4):2380, 1990.

[97] John C Slater and George F Koster. Simplified lcao method for the periodic potential problem. *Physical Review*, 94(6):1498, 1954.

[98] D. Sénéchal, A. G. R. Day, V. Bouliane, and A.-M. S. Tremblay. Resilience of d-wave superconductivity to nearest-neighbor repulsion. *Phys. Rev. B*, 87(7):075123, February 2013.

[99] Qing-Kun Tang, Lin Yang, Da Wang, Fu-Chun Zhang, and Qiang-Hua Wang. Spin-triplet f-wave pairing in twisted bilayer graphene near quarter filling. *Physical Review B*, 99(9):094521, 2019.

[100] Luis EF Foa Torres, Jean-Christophe Charlier, and Stephan Roche. *Introduction to graphene-based nanomaterials: from electronic structure to quantum transport*, volume 1. Springer, 2013.

[101] G Trambly de Laissardiere, Didier Mayou, and Laurence Magaud. Localization of Dirac electrons in rotated graphene bilayers. *Nano letters*, 10(3):804–808, 2010.

[102] Seiji Uryu. Electronic states and quantum transport in double-wall carbon nanotubes. *Physical Review B*, 69(7):075402, 2004.

[103] Tuomas I Vanhala and Lode Pollet. Constrained random phase approximation of the effective Coulomb interaction in lattice models of twisted bilayer graphene. *Physical Review B*, 102(3):035154, 2020.

[104] M Vekić and SR White. Pseudogap formation in the half-filled Hubbard model. *Physical Review B*, 47(2):1160, 1993.

[105] JR Wallbank, AA Patel, M Mucha-Kruczyński, AK Geim, and VI Fal'Ko. Generic miniband structure of graphene on a hexagonal substrate. *Physical Review B*, 87(24):245408, 2013.

[106] Xiaoyu Wang and Oskar Vafek. Diagnosis of explicit symmetry breaking in the tight-binding constructions for symmetry-protected topological systems. *Physical Review B*, 102(7):075142, 2020.

[107] Yaping Wu, Harry Chou, Hengxing Ji, Qingzhi Wu, Shanshan Chen, Wei Jiang, Yufeng Hao, Junyong Kang, Yujie Ren, Richard D Piner, et al. Growth mechanism and controlled synthesis of ab-stacked bilayer graphene on Cu-Ni alloy foils. *Acs Nano*, 6(9):7731–7738, 2012.

[108] Cenke Xu and Leon Balents. Topological superconductivity in twisted multilayer graphene. *Physical review letters*, 121(8):087001, 2018.

[109] Matthew Yankowitz, Jiamin Xue, and Brian J LeRoy. Graphene on hexagonal boron nitride. *Journal of Physics: Condensed Matter*, 26(30):303201, 2014.

[110] Noah FQ Yuan and Liang Fu. A model for metal-insulator transition in graphene superlattices and beyond. *arXiv preprint arXiv:1803.09699*, 2018.

[111] Marc G Zacher, Robert Eder, Enrico Arrigoni, and Werner Hanke. Stripes in doped antiferromagnets: single-particle spectral weight. *Physical review letters*, 85(12):2585, 2000.

[112] Marc G Zacher, Robert Eder, Enrico Arrigoni, and Werner Hanke. Evolution of the stripe phase as a function of doping from a theoretical analysis of angle-resolved photoemission data. *Physical Review B*, 65(4):045109, 2002.

[113] Li-Da Zhang, Fan Yang, and Yugui Yao. Itinerant ferromagnetism and $p + ip'$ superconductivity in doped bilayer silicene. *Physical Review B*, 92(10):104504, 2015.

[114] Lufeng Zhang, Tongyun Huang, Ying Liang, and Tianxing Ma. Ground state superconducting pair correlations in twisted bilayer graphene. *Mod. Phys. Lett. B*, 34(01):2050016, December 2019.